2008

# Flow structure on a 1303 UCAV subjected to small amplitude perturbations

Turgut Oruc Yilmaz
*Lehigh University*

Yilmaz, Turgut Oruc

# Flow Structure on a 1303 UCAV Subjected to Small Amplitude Perturbations

January 2009

# FLOW STRUCTURE ON A 1303 UCAV SUBJECTED TO SMALL AMPLITUDE PERTURBATIONS

by

Turgut Oruc Yilmaz

A Thesis

Presented to the Graduate and Research Committee

of Lehigh University

in Candidacy for the Degree of

Master of Science

in

The Department of Mechanical Engineering and Mechanics

Lehigh University

December, 2008

This thesis is accepted and approved in partial fulfillment of the requirements for the Master of Science.

12/02/08

Date

Thesis Advisor

Chairperson of Department

**ACKNOWLEDGMENTS**

I would like to express my deep gratitude and grateful thanks to my research advisor, Prof. Donald Rockwell, for his extensive wisdom, great guidance and encouragement, close support, efforts and distinguished supervision throughout this study.

I would like to mention my thanks to the Air Force Office of Scientific Research for its financial support.

I would like to express my gratitude to my professors from my undergraduate school, Prof. Metin Muradoglu and Prof. Ozgur Mustecaplioglu, for their supervision and invaluable contribution to my background and education.

I appreciate the assistance of the machine shop, particularly Mr. Richard Towne, Mr. Robert Minnich and Mr. James Bunderla for their craftsmanship. I am also very thankful to Mrs. JoAnn Casciano, Mrs. Geri Kneller, and Mrs. Carol Paul and for their kindness and administrative assistance. Many thanks to my colleagues, Dr. Alis Ekmekci, Dr. Tunc Goruney, Mr. Can Koroglu, Mr. Cem Alper Ozen, Mr. Egemen Tinar, Mr. Philip Breneman, and Mr. Mehmet Alpaslan Koseoglu for their valuable contributions, moral support and friendship.

I owe my heartfelt gratitude and thanks to my parents for their moral support and motivation; my best friend Okan, who was behind me in every step I took.

Last but the most I am grateful to my beautiful wife Esra for her encouragement, support, patience, love and everything, who deserves all the best.

And finally, to my baby boy Omer, thanks for your coming to my life.

TABLE OF CONTENTS

## LIST OF FIGURES:

**Figure A.18:** Comparison of dye visualization versus computational results of vortical structure at angle-of-attack $\alpha = 12^{o}$. Reynolds number based on mean aerodynamic chord is $Re_c = 32{,}000$.

**Figure A.19:** Comparison of dye visualization versus computational results of vortical structure at angle-of-attack $\alpha = 15^{o}$. Reynolds number based on mean aerodynamic chord is $Re_c = 32{,}000$.

**Figure A.20:** Comparison of experimental and computational results of time-averaged patterns of vorticity and Reynolds stress at $\alpha = 6^{o}$. Reynolds number based on mean aerodynamic chord is $Re_c = 32{,}000$.

**Figure A.21:** Comparison of experimental and computational results of time-averaged patterns of vorticity and Reynolds stress at $\alpha = 12^{o}$. Reynolds number based on mean aerodynamic chord is $Re_c = 32{,}000$.

**Figure AA.1:** Time-averaged vorticity and Reynolds stress contours for case of wing subjected to perturbations of angle-of-attack according to $\alpha = \overline{\alpha} + \alpha_e \sin 2\pi f_e t$ ; $\overline{\alpha} = 12^{o}$, $\alpha_e = 0.45^{o}$ and $f_e = f_o/8, f_o/4, f_o/2$ and $f_o$ where $f_o$ is the inherit instability frequency of separating shear layer. Reynolds number based on mean aerodynamic chord is $Re_c = 17{,}927$.

**Figure AA.2:** Time-averaged streamwise velocity contours and streamlines for case of wing subjected to perturbations of angle-of-attack according to $\alpha = \overline{\alpha} + \alpha_e \sin 2\pi f_e t$ ; $\overline{\alpha} = 12^{o}$, $\alpha_e = 0.45^{o}$ and $f_e = f_o/8, f_o/4, f_o/2$ and $f_o$ where $f_o$ is the inherit instability frequency of separating shear layer. Reynolds number based on mean aerodynamic chord is $Re_c = 17{,}927$.

**Figure AA.3:** Time-averaged vorticity and Reynolds stress contours for case of wing subjected to perturbations of angle-of-attack according to $\alpha = \overline{\alpha} + \alpha_e \sin 2\pi f_e t$ ; $\overline{\alpha} = 12^{o}$, $\alpha_e = 0.45^{o}$ and $f_e = f_o/8, f_o/4, f_o/2$ and $f_o$ where $f_o$ is the inherit instability frequency of separating shear layer. Reynolds number based on mean aerodynamic chord is $Re_c = 17{,}927$.

**Figure AA.4:** Time-averaged streamwise velocity contours and streamlines for case of wing subjected to perturbations of angle-of-attack according to $\alpha = \overline{\alpha} + \alpha_e \sin 2\pi f_e t$ ; $\overline{\alpha} = 12^{o}$, $\alpha_e = 0.45^{o}$ and $f_e = f_o/8, f_o/4, f_o/2$ and $f_o$ where $f_o$ is the inherit instability frequency of separating shear layer. Reynolds number based on mean aerodynamic chord is $Re_c = 17{,}927$.

**Figure AA.5:** Time-averaged vorticity and Reynolds stress contours for case of wing subjected to perturbations of angle-of-attack according to $\alpha = \overline{\alpha} + \alpha_e \sin 2\pi f_e t$ ; $\overline{\alpha} = 12^{o}$,

$\alpha_e = 0.45^\circ$ and $f_e = f_o/8, f_o/4, f_o/2$ and $f_o$ where $f_o$ is the inherit instability frequency of separating shear layer. Reynolds number based on mean aerodynamic chord is $Re_c$ = 17,927.

**Figure AA.6:** Time-averaged streamwise velocity contours and streamlines for case of wing subjected to perturbations of angle-of-attack according to $\alpha = \bar{\alpha} + \alpha_e \sin 2\pi f_e t$ ; $\bar{\alpha}$ = $12^\circ$, $\alpha_e = 0.45^\circ$ and $f_e = f_o/8, f_o/4, f_o/2$ and $f_o$ where $f_o$ is the inherit instability frequency of separating shear layer. Reynolds number based on mean aerodynamic chord is $Re_c$ = 17,927.

**Figure AA.7:** Time-averaged vorticity and Reynolds stress contours for case of wing subjected to perturbations of angle-of-attack according to $\alpha = \bar{\alpha} + \alpha_e \sin 2\pi f_e t$ ; $\bar{\alpha} = 12^\circ$, $\alpha_e = 0.45^\circ$ and $f_e = f_o/8, f_o/4, f_o/2$ and $f_o$ where $f_o$ is the inherit instability frequency of separating shear layer. Reynolds number based on mean aerodynamic chord is $Re_c$ = 17,927.

**Figure AA.8:** Time-averaged streamwise velocity contours and streamlines for case of wing subjected to perturbations of angle-of-attack according to $\alpha = \bar{\alpha} + \alpha_e \sin 2\pi f_e t$ ; $\bar{\alpha}$ = $12^\circ$, $\alpha_e = 0.45^\circ$ and $f_e = f_o/8, f_o/4, f_o/2$ and $f_o$ where $f_o$ is the inherit instability frequency of separating shear layer. Reynolds number based on mean aerodynamic chord is $Re_c$ = 17,927.

**Figure AA.9:** Time-averaged vorticity and streamwise velocity contours for case of wing subjected to perturbations of angle-of-attack according to $\alpha = \bar{\alpha} + \alpha_e \sin 2\pi f_e t$ ; $\bar{\alpha}$ = $12^\circ$, $\alpha_e = 0.45^\circ$ and $f_e = f_o/2$ where $f_o$ is the inherit instability frequency of separating shear layer. Reynolds number based on mean aerodynamic chord is $Re_c$ = 17,927.

**Figure AA.10:** Time-averaged streamlines and Reynolds stress contours for case of wing subjected to perturbations of angle-of-attack according to $\alpha = \bar{\alpha} + \alpha_e \sin 2\pi f_e t$ ; $\bar{\alpha}$ = $12^\circ$, $\alpha_e = 0.45^\circ$ and $f_e = f_o/2$ where $f_o$ is the inherit instability frequency of separating shear layer. Reynolds number based on mean aerodynamic chord is $Re_c$ = 17,927.

**Figure AA.11:** Time-averaged vorticity contours for case of wing subjected to perturbations of angle-of-attack according to $\alpha = \bar{\alpha} + \alpha_e \sin 2\pi f_e t$ ; $\bar{\alpha} = 12^\circ$, $\alpha_e = 0.45^\circ$ and $f_e = f_o/2$ where $f_o$ is the inherit instability frequency of separating shear layer. Reynolds number based on mean aerodynamic chord is $Re_c$ = 17,927.

**Figure AA.12:** Time-averaged Reynolds stress contours for case of wing subjected to perturbations of angle-of-attack according to $\alpha = \bar{\alpha} + \alpha_e \sin 2\pi f_e t$ ; $\bar{\alpha} = 12^\circ$, $\alpha_e = 0.45^\circ$ and $f_e = f_o/2$ where $f_o$ is the inherit instability frequency of separating shear layer. Reynolds number based on mean aerodynamic chord is $Re_c$ = 17,927.

**Figure AA.13:** Time-averaged streamwise velocity contours for case of wing subjected to perturbations of angle-of-attack according to $\alpha = \bar{\alpha} + \alpha_e \sin 2\pi f_e t$ ; $\bar{\alpha} = 12^o$, $\alpha_e = 0.45^o$ and $f_e = f_o/2$ where $f_o$ is the inherit instability frequency of separating shear layer. Reynolds number based on mean aerodynamic chord is $Re_c = 17{,}927$.

**Figure AA.14:** Time-averaged streamlines for case of wing subjected to perturbations of angle-of-attack according to $\alpha = \bar{\alpha} + \alpha_e \sin 2\pi f_e t$ ; $\bar{\alpha} = 12^o$, $\alpha_e = 0.45^o$ and $f_e = f_o/2$ where $f_o$ is the inherit instability frequency of separating shear layer. Reynolds number based on mean aerodynamic chord is $Re_c = 17{,}927$.

**Figure AA.15:** Phase-averaged vorticity contours for case of wing subjected to perturbations of angle-of-attack according to $\alpha = \bar{\alpha} + \alpha_e \sin 2\pi f_e t$ ; $\bar{\alpha} = 12^o$, $\alpha_e = 0.45^o$ and $f_e = f_o/4$ where $f_o$ is the inherit instability frequency of separating shear layer. Reynolds number based on mean aerodynamic chord is $Re_c = 17{,}927$.

**Figure AA.16:** Phase-averaged vorticity contours for case of wing subjected to perturbations of angle-of-attack according to $\alpha = \bar{\alpha} + \alpha_e \sin 2\pi f_e t$ ; $\bar{\alpha} = 12^o$, $\alpha_e = 0.45^o$ and $f_e = f_o/2$ where $f_o$ is the inherit instability frequency of separating shear layer. Reynolds number based on mean aerodynamic chord is $Re_c = 17{,}927$.

**Figure AA.17:** Phase-averaged vorticity contours for case of wing subjected to perturbations of angle-of-attack according to $\alpha = \bar{\alpha} + \alpha_e \sin 2\pi f_e t$ ; $\bar{\alpha} = 12^o$, $\alpha_e = 0.45^o$ and $f_e = f_o$ where $f_o$ is the inherit instability frequency of separating shear layer. Reynolds number based on mean aerodynamic chord is $Re_c = 17{,}927$.

**Figure AA.18:** Phase-averaged vorticity contours for case of wing subjected to perturbations of angle-of-attack according to $\alpha = \bar{\alpha} + \alpha_e \sin 2\pi f_e t$ ; $\bar{\alpha} = 12^o$, $\alpha_e = 0.45^o$ and $f_e = f_o/4$ where $f_o$ is the inherit instability frequency of separating shear layer. Reynolds number based on mean aerodynamic chord is $Re_c = 17{,}927$.

**Figure AA.19:** Phase-averaged vorticity contours for case of wing subjected to perturbations of angle-of-attack according to $\alpha = \bar{\alpha} + \alpha_e \sin 2\pi f_e t$ ; $\bar{\alpha} = 12^o$, $\alpha_e = 0.45^o$ and $f_e = f_o/2$ where $f_o$ is the inherit instability frequency of separating shear layer. Reynolds number based on mean aerodynamic chord is $Re_c = 17{,}927$.

**Figure AA.20:** Phase-averaged vorticity contours for case of wing subjected to perturbations of angle-of-attack according to $\alpha = \bar{\alpha} + \alpha_e \sin 2\pi f_e t$ ; $\bar{\alpha} = 12^o$, $\alpha_e = 0.45^o$ and $f_e = f_o$ where $f_o$ is the inherit instability frequency of separating shear layer. Reynolds number based on mean aerodynamic chord is $Re_c = 17{,}927$.

**Figure AA.21:** Phase-averaged vorticity contours for case of wing subjected to perturbations of angle-of-attack according to $\alpha = \bar{\alpha} + \alpha_e \sin 2\pi f_e t$ ; $\bar{\alpha} = 12^o$, $\alpha_e = 0.45^o$

and $f_e = f_o/4$ where $f_o$ is the inherit instability frequency of separating shear layer. Reynolds number based on mean aerodynamic chord is $Re_c = 17{,}927$.

**Figure AA.22:** Phase-averaged vorticity contours for case of wing subjected to perturbations of angle-of-attack according to $\alpha = \bar{\alpha} + \alpha_e \sin 2\pi f_e t$ ; $\bar{\alpha} = 12^o$, $\alpha_e = 0.45^o$ and $f_e = f_o/2$ where $f_o$ is the inherit instability frequency of separating shear layer. Reynolds number based on mean aerodynamic chord is $Re_c = 17{,}927$.

**Figure AA.23:** Phase-averaged vorticity contours for case of wing subjected to perturbations of angle-of-attack according to $\alpha = \bar{\alpha} + \alpha_e \sin 2\pi f_e t$ ; $\bar{\alpha} = 12^o$, $\alpha_e = 0.45^o$ and $f_e = f_o$ where $f_o$ is the inherit instability frequency of separating shear layer. Reynolds number based on mean aerodynamic chord is $Re_c = 17{,}927$.

**Figure AA.24:** Phase-averaged vorticity contours for case of wing subjected to perturbations of angle-of-attack according to $\alpha = \bar{\alpha} + \alpha_e \sin 2\pi f_e t$ ; $\bar{\alpha} = 12^o$, $\alpha_e = 0.45^o$ and $f_e = f_o/4, f_o/2$ and $f_o$ where $f_o$ is the inherit instability frequency of separating shear layer. Case of stationary wing shown for comparison. Reynolds number based on mean aerodynamic chord is $Re_c = 17{,}927$.

**Figure AA.25:** Phase-averaged vorticity contours for case of wing subjected to perturbations of angle-of-attack according to $\alpha = \bar{\alpha} + \alpha_e \sin 2\pi f_e t$ ; $\bar{\alpha} = 12^o$, $\alpha_e = 0.45^o$ and $f_e = f_o/4, f_o/2$ and $f_o$ where $f_o$ is the inherit instability frequency of separating shear layer. Case of stationary wing shown for comparison. Reynolds number based on mean aerodynamic chord is $Re_c = 17{,}927$.

**Figure AA.26:** Phase-averaged vorticity contours for case of wing subjected to perturbations of angle-of-attack according to $\alpha = \bar{\alpha} + \alpha_e \sin 2\pi f_e t$ ; $\bar{\alpha} = 12^o$, $\alpha_e = 0.45^o$ and $f_e = f_o/4, f_o/2$ and $f_o$ where $f_o$ is the inherit instability frequency of separating shear layer. Case of stationary wing shown for comparison. Reynolds number based on mean aerodynamic chord is $Re_c = 17{,}927$.

**Figure AA.27:** Phase-averaged and instantaneous vorticity contours for case of wing subjected to perturbations of angle-of-attack according to $\alpha = \bar{\alpha} + \alpha_e \sin 2\pi f_e t$ ; $\bar{\alpha} = 12^o$, $\alpha_e = 0.45^o$ and $f_e = f_o/4$, $f_o/2$ and $f_o$ where $f_o$ is the inherit instability frequency of separating shear layer. Reynolds number based on mean aerodynamic chord is $Re_c = 17{,}927$.

**Figure AA.28:** Phase-averaged and instantaneous vorticity contours for case of wing subjected to perturbations of angle-of-attack according to $\alpha = \bar{\alpha} + \alpha_e \sin 2\pi f_e t$ ; $\bar{\alpha} = 12^o$, $\alpha_e = 0.45^o$ and $f_e = f_o/4$, $f_o/2$ and $f_o$ where $f_o$ is the inherit instability frequency of separating shear layer. Reynolds number based on mean aerodynamic chord is $Re_c = 17{,}927$.

**Figure AA.29:** Patterns of phase-averaged and instantaneous vorticity on stationary wing. Reynolds number based on mean aerodynamic chord is $Re_c = 17{,}927$.

**Figure AA.30:** Comparison of time-averaged patterns of vorticity at two values of Reynolds number based on mean aerodynamic chord, $Re_c = 17927$ (left column) and $Re_c = 32{,}000$ (right column). Wing is subjected to perturbations of angle-of-attack according to $\alpha = \bar{\alpha} + \alpha_e \sin 2\pi f_e t$ ; $\bar{\alpha} = 12^o$, $\alpha_e = 0.45^o$ and $f_e = f_o/4$ and $f_o/2$ where $f_o$ is the inherit instability frequency of separating shear layer.

**Figure AA.31:** Comparison of time-averaged patterns of Reynolds stress at two values of Reynolds number based on mean aerodynamic chord, $Re_c = 17{,}927$ (left column) and $Re_c = 32{,}000$ (right column). Wing is subjected to perturbations of angle-of-attack according to $\alpha = \bar{\alpha} + \alpha_e \sin 2\pi f_e t$ ; $\bar{\alpha} = 12^o$, $\alpha_e = 0.45^o$ and $f_e = f_o/4$ and $f_o/2$ where $f_o$ is the inherit instability frequency of separating shear layer.

**Figure AA.32:** Comparison of time-averaged patterns of streamwise velocity at two values of Reynolds number based on mean aerodynamic chord, $Re_c = 17{,}927$ (left column) and $Re_c = 32{,}000$ (right column). Wing is subjected to perturbations of angle-of-attack according to $\alpha = \bar{\alpha} + \alpha_e \sin 2\pi f_e t$ ; $\bar{\alpha} = 12^o$, $\alpha_e = 0.45^o$ and $f_e = f_o/4$ and $f_o/2$ where $f_o$ is the inherit instability frequency of separating shear layer.

**NOMENCLATURE:**

| | |
|---|---|
| $\alpha$ | Angle-of-attack |
| $\alpha_e$ | Angular displacement amplitude |
| $f_o$ | Inherit instability frequency of separating shear layer |
| $Re_C$ | Reynolds number based on mean aerodynamic chord |
| $Re_{Croot}$ | Reynolds number based on root chord |
| $\Delta$ | Displacement of the plane of symmetry of the wing |
| $\varepsilon$ | Spanwise location |
| $C^*$ | Sectional chord length |
| $S$ | Semi-span length |
| $x$ | Coordinate in streamwise direction |
| $y$ | Coordinate in surface normal/crossflow direction |
| $z$ | Coordinate in transverse direction |
| $\langle \underline{V} \rangle$ | Time-averaged velocity vectors |
| $\langle \omega \rangle$ | Time-averaged surface normal vorticity |
| $\langle \Psi \rangle$ | Time-averaged streamlines |
| $\langle u \rangle$ | Time-averaged streamwise velocity |
| U | Freestream velocity |
| $C_{ROOT}$ | Length of root chord |
| $f_e$ | Excitation frequency |
| $f_o^*$ | Inherit instability frequency at specific spanwise location |
| $C$ | Mean aerodynamic chord length |
| $\Delta y_{LE}$ | Displacement of the leading-edge |
| $\lambda$ | Wavelength between vortices |
| $h(t)$ | Instantaneous vertical displacement of the leading-edge |
| $t$ | Time |
| $T$ | Period |
| $a$ | Appearance of vorticity cluster |

| | |
|---|---|
| $BL^+$ | Positive bifurcation line |
| $F^-$ | Focus of separation |
| $F^+$ | Focus of attachment |
| S | Saddle point |

**ABSTRACT**

The performance of Unmanned Combat Air Vehicles (UCAVs) is of increasing interest, and in order to optimize flight performance, it is necessary to understand the detailed flow structure. Moreover, it is often desirable to employ flow control techniques. In the present study, the complex flow physics is investigated along a half- model of the 1303 UCAV which is representative of a variety of UCAVs with blended wing-body configurations. Using techniques of dye visualization and particle image velocimetry, the complex flow structure is defined on streamwise-oriented planes at a number of locations along the span of the wing. These quantitative flow patterns provide an understanding of the effects of variations of angle-of-attack and Reynolds number.

Open-loop active control is employed, in order to eliminate large-scale stall regions through reattachment of the flow. This control is in the form of small amplitude angular perturbations of the wing, of the order of one-half degree. Excitation at either the fundamental or the first subharmonic of the inherent instability frequency of the separating shear layer nearly eliminates the large-scale separation (stall) zone along the wing at high angle of attack. The physics of the flow is interpreted in terms of time-mean streamlines, vorticity, and Reynolds stress, in conjunction with phase-averaged patterns of instantaneous vorticity.

# 1. INTRODUCTION

Unmanned combat air vehicles (UCAV) are of increasing interest, due to their potential for maneuverability, endurance for surveillance, and quick penetration (Zhang et al, 2005). Wing configurations of the UCAV type are inherently three-dimensional with spanwise variations in local chord length and thickness. As a result, the corresponding flow structure can be very complex, involving spanwise variations of separation, stall, and associated unsteadiness, as reviewed, for example, by Gursul (2004b).

## *1.1 Previous Experimental and Computational Investigations of 1303 UCAV*

The 1303 UCAV of interest herein is a generic configuration, which was developed by AFRL, in cooperation with Boeing (Sherer et al, 2008). The 1303 configuration, with leading edge sweep of $47^{o}$ and cranked trailing edge, is representative of a variety of UCAVs with blended wing-body configurations (Ol, 2006). It has served as the basis for international investigations involving wind tunnel studies by Bruce (2003) and McParlin et al. (2003). A 1303 UCAV model was tested in the QinetiQ low-speed wind tunnel in order to investigate the onset and development of the flow separation near the wing leading edge and its sensitivity to leading edge radius and Reynolds number (McParlin et al, 2003). This test provided detailed information on the force and moment coefficients, surface pressure distribution, and a pitch break phenomenon, which is a result of the onset and development of flow separation over the outer portion of the wing. Ol (2006) recently determined the flow structure, and investigated flow separation in terms of patterns of

mean velocity and Reynolds stress, in conjunction with dye visualization, in a water facility. Using quantitative images obtained from PIV experiments, Ol (2006) compared patterns of velocity and Reynolds stress in the tip region with patterns at locations further inboard. He indicated that flow in the vicinity of the tip at $\alpha = 6^{o}$ is noticeably separated, while the flow inboard of the tip is attached, with a small laminar separation bubble. Ol (2006) also observed that, at $\alpha = 12^{o}$, formation of a leading-edge vortex (LEV) can occur, in accord with outboard branching of the dye visualization pattern at a location immediately downstream of the apex. Nelson et al. (2007) undertook dye injection in a water facility to characterize the onset of vortex formation and separated flow. The dye patterns showed that, at low angles of attack, $\alpha \leq 7^{o}$, the flow over most of the upper surface was dominated by a mean cross-flow from the wing root towards the tip. The formation of a leading edge vortex was evident at larger angles of attack, $\alpha > 8^{o}$ (Nelson et al, 2007).

Kosoglu (2007) employed dye visualization and particle image velocimetry to address the unsteady features of the flow structure in planes approximately parallel to the wing surface. Dye visualization results showed that tip stall is present at all angles-of-attack and it moves in the upstream direction and inboard with increasing angle-of-attack. Results obtained from near-surface PIV provided detailed characterization of the physics of tip stall. The scale of the stall region is highly dependent on the value of angle-of-attack and the distance from the surface of the wing. Furthermore, the results showed that the center of the stall region moves upstream with increasing angle-of-attack, and is located further downstream with the increasing distance from the surface

of wing. Moreover, the scale of the stall region, indicated by the pattern in a plane parallel to the surface of the wing, increases with increasing angle of attack. Also, it was shown that the extent of the stall region in the surface normal direction increased with angle-of-attack (Kosoglu, 2007).

Numerical investigations of the 1303 UCAV configuration include Zhang et al. (2005), Petterson (2006), Wong and Flores (2006), Atkinson and Ferguson (2006), and Wong et al. (2006). Most recently, Scherer et al. (2008) employed a high-order overset-grid algorithm to provide insight into the flow structure as a function of angle-of-attack, and directly compared their results with the experimental images of Ol (2006).

Insight into the flow structure on a three-dimensional UCAV configuration, such as the 1303 UCAV, builds upon extensive, recent studies of the flow structure on planar delta wings of low to moderate sweep angle. The high-order, structured-grid, finite-difference algorithm of Gordnier and Visbal (1998) has served as a basis for numerical computations on delta wings of low sweep angle at low Reynolds numbers by Gordnier and Visbal (2005) and moderate Reynolds numbers by Gordnier and Visbal (2006) and Gordnier et al. (2007). In these computations, an implicit, large-eddy simulation ILES method is employed, and at moderate Reynolds numbers, a hybrid RANS-ILES approach is employed.

Experimental investigations on planar delta wings and UCAV planforms are reviewed by Gursul (2004a, 2004b) and Gursul et al. (2005). Experiments on wings of low to moderate sweep angle, as well as on planar versions of UCAV planforms, are

addressed by Ol and Gharib (2003), Yaniktepe and Rockwell (2004, 2005) and Yavuz et al. (2004). Yaniktepe and Rockwell (2004, 2005) and Yavuz et al. (2004) investigated the flow structure on crossflow and near-surface planes for delta wings having relatively low values of sweep angle. Elkhoury and Rockwell (2004) investigated the effects of Reynolds number on the formation of vortices on a UCAV planform using dye visualization.

### *1.2 Control of the Flow Structure*

Various active and passive flow control techniques have been employed to control flows over delta wings, and attain enhancement of lift, optimization of forces and moments for flight control and maneuverability, attenuation of buffeting, reduction of drag, and attenuation of noise due to vortex/blade interaction. Gursul et al. (2007) review vortex control methods for slender, nonslender and high aspect ratio wings, which include manipulation of one or more of the following phenomena: flow separation from the leading-edge and surface of the wing, vortex formation, vortex breakdown, and flow reattachment to the wing surface.

Control of the flow structure on a flat delta wing of low sweep angle at high angle-of-attack was pursued by Yaniktepe and Rockwell (2004). The wing was perturbed at small angular displacement amplitude (one degree), and at a frequency corresponding to the first subharmonic of the separating shear layer from the leading-edge. It was possible to recover the leading-edge vortex, involving a well-defined focus of the cross-flow topology, as well as ordered and concentrated streamwise vorticity in the cross-flow plane. These changes were accompanied by early onset of

Reynolds stresses in the separating shear layer. Gursul et al. (2006) and Vardaki et al. (2008) investigated perturbation of wings of various sweep angle and determined that the optimum frequency for attainment of vortex reformation and/or flow reattachment was in the range $fC/U = 1$ to 2. They also addressed the consequence of both the symmetric and anti-symmetric excitation. Taylor et al. (2007) addressed the effect of wing flexibility at a dominant frequency $fC/U \sim 1$; such flexibility enhanced reattachment of the shear layer, which was associated with enhancement of lift. Self-excited limit cycle oscillations of wings are of basic importance, and a representative study is provided by Attar et al. (2008).

The goal of the present investigation is to characterize of the flow structure at various angles-of-attack and Reynolds numbers, and to determine the effect of very small angular displacement amplitudes, of the order of 0.5°, on the flow structure along a UCAV configuration at high angle-of-attack. The range of excitation frequency encompasses the fundamental and subharmonics of the frequency of naturally-occurring, small-scale vortex formation from the leading-edge of the wing. Moreover, the consequence of this excitation on the flow structure at different spanwise locations is addressed. A technique of high-image-density particle image velocimetry is employed to determine the time-averaged patterns of the mean and turbulent flow structure. In addition, phase-averaged images allow definition of the time variation of the flow structure that yields large modifications of the time-averaged patterns.

## 2. EXPERIMENTAL SYSTEM AND TECHNIQUES

Experiments were performed in a large scale, low-turbulence water channel in the form of a free surface, located in the Fluid Mechanics Laboratory at Lehigh University. Experiments involved investigation and quantitatively characterization of the flow structure, and determination of the effect of very small angular displacement amplitudes along 1303 UCAV using techniques of dye visualization and high-image-density particle image velocimetry.

A schematic of the water channel is shown in Figure 1a. It had a main test section of 613 mm width, 594 mm depth and 5435 mm length. An arrangement of honeycomb and a sequence of five screens were located at the entrance to attain low turbulence intensities of approximately 0.3% over the test section. The experiments were performed at a free-stream velocity varied over the range $23.6 \leq U_\infty \leq 251$ mm/sec.

A simplified schematic of the 1303 UCAV model is shown in Figure 1b. A half-wing arrangement of the model was used in the experiments and mounted on a vertical plate as illustrated in Figure 1a. In order to eliminate the effects of the approach boundary layer, it was maintained very thin by locating the apex of the wing immediately downstream of the leading-edge of the vertical mounting plate. Moreover, the wing model was manufactured in such a way that the plane of symmetry of the wing was far enough from the vertical plate to prevent effects of boundary layer. The displacement of the plane of symmetry of the wing from the vertical mounting plate was $\Delta = 38.1$ mm. This displacement, $\Delta$, was larger than the

displacement thickness of the approach boundary layer along the vertical plate. The root chord of the wing was $C_{ROOT}$ = 355.6 mm and the mean aerodynamic chord length was C = 212.5 mm. The blockage ratio of the wing was calculated and found between 0.0261 and 0.0655 as shown in Figure 2. In order to ensure the validity of the experimental system of the half-model and vertical mounting plate, extensive dye visualization experiments and PIV measurements were performed and the results for both the full model and the half model of the 1303 UCAV were compared. The results and comparison showed that the type of half-wing model of Figure 1c replicates, with indistinguishable deviation, the flow pattern on the full wing. Dye was injected in the apex region, and for the Reynolds number $Re_c$ = 17,927 and angle of attack $\alpha$ = 12° of interest herein, the pattern remained symmetrical along the center body, as shown in Figure 1c. Also shown is dye visualization in the critical apex region at two higher values of Reynolds number, $Re_c$ = 29,878, and 59,757. In addition, dye visualization over the entire semi-span of interest (not shown herein) was compared for the present configuration and the full wing of Kosoglu (2007). The location of onset of abrupt expansion of the leading-edge vortex, as well as the location and shape of the interface between the stalled and unstalled regions along the wing were essentially the same. Finally, PIV images of contours of constant vorticity and streamlines were nearly indistinguishable for the present configuration and the full wing of Kosoglu (2007), at a spanwise location $\eta$ = 0.1, i.e., a distance of 10% of the span of the half wing, measured from the center body.

Experiments include two cases: first is the stationary (unperturbed) case, which means that the wing was mounted to the vertical plate and kept stationary; the second was the excited (perturbed) case, which means that the wing was subjected to angular perturbations of small displacement amplitude at specific frequencies. Preliminary experiments on the stationary wing were performed at four values of angle-of-attack $\alpha$ = 6°, 9°, 12° and 15°. At each angle-of-attack, four values of Reynolds number based on the root chord $Re_{Croot}$ = 10,000, 30,000, 50,000 and 100,000, corresponding to Reynolds number based on the mean aerodynamic chord $Re_C$ = 5,976, 17,927, 29,879 and 59,758, were considered to determine effects of Reynolds number on the flow patterns.

By examining the results of PIV and dye visualization for the stationary case, it was found that an angle-of-attack $\alpha$ = 12° provided a fully-stalled condition, which provided a basis for investigation of the effectiveness of perturbations on altering the stalled flow patterns; this value of $\alpha$ is employed herein. A computer-controlled motor system mounted above the water channel was used to control and provide perturbations of angle-of-attack as shown in Figure 1a. An adjustable jack provided variations in tension of the belt from the motor system to the axis of rotation of the wing, which was at the mid-chord of the 1303 UCAV model. This system provided perturbation frequencies up to 5 Hz for an amplitude of the pitching motion corresponding to 0.45°. The wing was perturbed at the fundamental $f_o$ and subharmonics $f_o/2$, $f_o/4$, and $f_o/8$ of the spanwise-averaged frequency $f_o$ of small-scale vortex formation from the leading-edge of the stationary wing. This vortex formation

was clearly prevalent at the spanwise locations $\eta$ = 0.5 to 0.9. The frequency $f_o$ = 2.5 Hz corresponds to a dimensionless frequency $f_oC/U$ = 6.64 based on mean aerodynamic chord, and dimensionless frequencies $f_oC^*/U$ = 4.86, 2.56 and 1.44 based on values of sectional chord $C^*$ at spanwise locations $\eta$ = 0.5, 0.7 and 0.9, in which $\eta$ = $z/S$, where $S$ is the semi-span of the wing. Ho and Huerre (1984) assess a wide variety of works involving perturbation of a shear layer separating from an edge. Excitation of the inherent, convective instability at the fundamental (most unstable) frequency $f_o$, or one of its subharmonics $f_o/n$, is particularly effective. This guidance provided the basis for selection of the excitation frequencies employed in this investigation, $f_o$ to $f_o/8$. For the present configuration, the most unstable frequency varies along the span of the stationary leading-edge, and the spanwise-averaged value of $f_o$ is considered. When the wing is perturbed, the frequency of the initial region of development of the instability is constant along the span, as verified with dye visualization. Furthermore, in the limiting case of a linearly evolving disturbance from the leading-edge of the wing, it is known from the inviscid stability calculations of Michalke (1984) that the separating shear layer can effectively amplify disturbances, that is, the magnitude of the amplification factor is large, over a relatively wide band of frequencies.

A technique of high-image-density particle image velocimetry was employed to characterize the quantitative flow patterns. The orientation of the laser sheet is shown in Figure 1a. The laser was mounted on a traverse system, allowing images to be acquired at various spanwise locations $\eta$.

The water was filtered with a one micron filter system and subsequently seeded with 12 micron diameter metallic coated neutrally buoyant plastic spheres. The seeding density was sufficiently high that 14 particle images were typically attained within the interrogation window of 32 pixels × 32 pixels employed for PIV. The seeding density of these particles was sufficiently large, such that the high image density criterion was satisfied. The laser sheet was generated by a dual pulsed Yag laser system having a maximum output of 90 mJ; approximately one-half of this output was employed during the current experiments. The pulse rate of the lasers was 29 Hz, which corresponds to the acquisition of 14.5 image pairs per second.

Processing of the patterns of particle images involved a frame-to-frame cross-correlation technique. A 32 × 32 pixel interrogation window was employed, with a 50% overlap. During the course of the experiments, acquisition of images at various spanwise locations $\eta$ along the span of the wing required readjustment of the distance from the sensor array of the camera to the physical plane of the laser sheet. This distance ranged from 456 mm to 1052 mm. In turn, this range corresponds to effective values of magnification extending from 19.7 to 4.55, and values of grid size (distance between locations of velocity vectors) in the physical plane of the laser sheet from 1.624 to 7.033 mm. More specifically, at values of $\eta$ = 0.1, 0.3, 0.5, 0.7 and 0.9, the values of magnification were 4.55, 7.07, 9.77, 13.414 and 19.77 pixel/mm,, and the effective grid sizes were 7.033, 4.557, 3.275, 2.385 and 1.624 mm. Values of magnification and grid size correspond to a field of view at values of $\eta$ = 0.3, 0.5, 0.7 and 0.9 in the physical plane of the laser sheet of 212 mm × 98 mm, 152 mm × 88

mm, 108 mm × 67 mm, 75 mm × 43 mm,. Furthermore, the number of pixels of the imaging camera was 1600 pixels × 1200 pixels. The overall uncertainty of the velocity measurements is estimated to 1.5%. In excitation (perturbed) case, images were not considered at $\eta = 0.1$.

In order to determine the time-averaged patterns of velocity vectors, $<\underline{V}>$, a total of 200 instantaneous images were averaged. Furthermore, time-averaged representations of the flow structure, involving surface normal vorticity $<\omega>$, streamlines $<\Psi>$, and contours of constant streamwise velocity $<u>$ were calculated from the time-averaged patterns of velocity vectors.

A TSI particle image velocimetry system was used for acquiring images. Insight 3G software of TSI was used in pre-processing, processing and post-processing of images. Background subtraction with minimum intensity was employed in the pre-processing section to remove the unexpected laser reflections from the boundary of the wing. During the interrogation process, the Nyquist criterion was satisfied, and the Hart Correlation Algorithm was used, which is a direct correlation method that processes only the most significant pixels to improve processing speed. A bilinear peak method was employed as a peak engine; it is the recommended peak engine for the Hart correlation. It works by locating the correlation peak with sub-pixel accuracy by fitting a set of linear functions to the highest pixel and its four nearest neighbors. In the post-processing section, the Median test method was applied for vector validation and elimination of bad vectors in the image of the flow field. Median test eliminates invalid vectors by comparing the difference between each

velocity vector and its local median velocity with the given tolerance. In order to fill the removed data, a recursive filling method was employed. Finally, by using Gaussian low-pass filtering, smoothing was performed after filling the holes. The Gaussian low-pass filter uses a rotationally symmetric kernel of size n (filter size), which was 5x5, and standard deviation $\sigma$, which was taken as 0.8 in present experiments. The results obtained from those parameters were compared with the results obtained from another program, NFILVB, which was previously used in the processing of previous experiments performed in the Fluid Mechanics Laboratories at Lehigh University. It was found that both results yielded the almost same velocity and vorticity contours of the flow field. The Tecplot 360 program was used to prepare the final forms of data which included patterns of velocity, vorticity, streamlines and Reynolds stress in time-averaged, phased-averaged and instantaneous form. The images presented in this thesis were prepared by utilizing CorelDraw program.

## 3. FLOW STRUCTURE ON STATIONARY WING

The goal of the stationary wing experiments is investigation and quantitative characterization of the flow structure along the 1303 UCAV configuration at four values of angle-of-attack $\alpha = 6°, 9°, 12°$ and 15°. For all cases, Reynolds number based on the root chord was $Re_{Croot} = 50{,}000$, corresponding to a value based on the mean aerodynamic chord of $Re_C = 29{,}879$. Moreover, the effects of Reynolds number on the flow structure were examined at angle-of-attack $\alpha = 12°$ for four values of Reynolds number based on the mean aerodynamic chord $Re_C$ = 5,976, 17,927, 29,879 and 59,758. All experiments were performed at five values of spanwise locations $\eta = 0.3$, 0.5, 0.7, 0.8 and 0.9, in which $\eta = z/S$, where $S$ is the semi-span of the wing. The results of the side-view PIV and the dye visualization measurements of the stationary wing are given in Figures A.1 trough A.21.

### *3.1 Effect of Angle-of-attack on Flow Structure*

Contours of time of time-averaged dimensionless vorticity $\langle\omega\rangle C_{ROOT}/U$ and the streamwise component of velocity $\langle u\rangle/U$ for angles-of-attack $\alpha = 6°, 9°, 12°$ and 15° are presented in Figures A.1, A.3, A.5 and A.7 at five values of spanwise location $\eta$ = 0.3, 0.5, 0.7, 0.8 and 0.9. For each angle-of-attack, time-averaged streamlines $\langle\Psi\rangle$ and Reynolds stress correlation $\langle u'v'\rangle/U^2$ are shown in Figures A.2, A.4, A.6, and A.8.

At the lowest angle-of-attack, $\alpha = 6°$, the vorticity $\langle\omega\rangle C_{ROOT}/U$ indicate that at the tip of the wing corresponding to $\eta$ = 0.9, the region of high level vorticity,

indicated by the red color, extends to nearly the trailing-edge of the wing section; this extent of the high level region corresponds to the dimensionless streamwise distance $x/C = 0.28$. Further inboard from the tip of the wing, at values of $\eta = 0.8$ successively, this streamwise extent of $x/C = 0.28$ is approximately preserved. At locations still further inboard of the wing tip, $\eta = 0.5$ and 0.3, the layer of vorticity remains attached to the wing along its entire streamwise extent. These patterns of vorticity $<\omega>C_{ROOT}/U$ are associated with the contours of constant streamwise velocity $<u>/U$ shown in the right column of Figure 8.1. Most significant is the occurrence of a region of nearly zero or even negative velocity $<u>/U$ in the region adjacent to the wing surface, for values of $\eta = 0.7$ through 0.9. This observation suggests that the flow pattern on the outboard region of the wing is, essentially, stalled at $\eta = 0.9$ and exhibits bubbles of decreasing size at $\eta = 0.8$ and 0.7. The patterns of streamlines shown in Figure A.2 show these regions of separated flow. The contours of constant Reynolds stress $<u'v'>/U^2$ shown in the right column of Figure A.2 indicate that the onset of significant turbulence occurs as the separated shear layer approaches the region of the trailing-edge of the wing at values of $\eta = 0.7$ through 0.9. At a higher value of angle-of-attack, $\alpha = 9°$, shown in Figure A.3, illustrated in the left column, which shows patterns of vorticity $<\omega>C_{ROOT}/U$, the streamwise extent of the region of highest level (red) vorticity extends only to $x/C$ of approximately 0.18 to 0.2 at spanwise sections $\eta = 0.7$ to 0.9. This streamwise extent of the high vorticity region is significantly smaller, and at the lower angle-of-attack $\alpha = 6°$ illustrated in the left column of Figure

A.1. $\langle\omega\rangle C_{ROOT}/U$ fully attached vorticity layer is evident only at $\eta = 0.3$. Substantially large regions of zero or negative streamwise velocity $\langle u\rangle/U$ are shown in Figure A.3 at values of $\eta$ = 0.7 through 0.9, and a detectable region of velocity immediately adjacent to the surface of the wing, representative of a separation bubble, is evident at $\eta = 0.5$.

The corresponding patterns of streamlines in Figure A.4 are in accord with the representations of the contours of constant streamwise velocity component shown in Figure A.3. That is, regions of large-scale flow separation occur at $\eta = 0.7$ through 0.9 and a separation bubble exists at $\eta$ = 0.5. Patterns of Reynolds stress correlation $\langle u'v'\rangle/U^2$ given in the right column of Figure A.4 indicate that the onset of substantial fluctuations has progressed well upstream of the location indicated for $\alpha = 6°$ in the right column of Figure A.2.

At a still larger angle-of-attack $\alpha$ = 12°, represented in Figure A.5, the trajectories of the vorticity layers suggest a substantially separated flow at spanwise locations $\eta$ = 0.5 to 0.9. Indeed, regions of large spatial extent of zero or negative streamwise velocity $\langle u\rangle/U$ are evident in the right column of Figure A.5 for values of $\eta = 0.5$ through 0.9. The corresponding patterns of streamlines in Figure A.6 reinforce this observation, and the patterns of Reynolds stress correlation $\langle u'v'\rangle/U^2$ given in the right column of Figure A.6 show substantial values over a significant share of the wing section.

At the highest angle-of-attack $\alpha = 15°$, shown in Figure A.7, the trajectories of the vorticity layer suggest highly separated flow over spanwise locations $\eta = 0.5$ to 0.9 and, indeed, the regions of (dark blue) zero or negative streamwise velocity $\langle u \rangle / U$ are strikingly evident in the right column of Figure 8.7. Even at the extreme inboard location $\eta = 0.3$, a region of localized separation, i.e., a separation bubble, is located immediately downstream of the leading-edge. All of these features are in accord with the patterns of streamlines given in the left column of Figure A.8. The onset of substantial values of Reynolds stress correlation $\langle u'v' \rangle / U^2$ is quite clear at values of $x/C = 0.2$ at all values of $\eta = 0.3$ to 0.9.

***3.2 Effect of Reynolds Number on Flow Structure***

To investigate the effects of Reynolds number and free-stream velocity on the stationary wing, experiments were performed at four values of Reynolds number based on the mean aerodynamic chord: $Re_C = 5{,}976$, 17,927, 29,879 and 59,758. The results of time-averaged patterns of vorticity, velocity, streamlines and Reynolds stress, and instantaneous patterns of vorticity are presented in Figures A.9 through Figure A.16. For this investigation, the angle-of-attack is maintained at a value $\alpha = 12°$.

Figures A.9, A.11 and A.13 show contours of time-averaged dimensionless vorticity $\langle \omega \rangle C_{ROOT} / U$ and the streamwise component of velocity $\langle u \rangle / U$ for values of Reynolds number based on mean aerodynamic chord $Re_C = 5{,}976$, 17,927 and 59,758. The same parameters are shown in Figure A.5 for $Re_C = 29{,}879$. From the comparison of contours of $\langle \omega \rangle C_{ROOT} / U$, it is clearly seen that the extent of the peak (red) regions

of vorticity slightly increases for higher Reynolds numbers $Re_C$ = 17,927 and 29,879 relative to the lowest value, $Re_C$ = 5,976. On the other hand, at the highest value of $Re_C$ = 59,758, this extent of red region becomes shorter relative to Reynolds numbers $Re_C$ = 17,927 and 29,879. There appears to be a limit value of Reynolds number on extension of the region of high positive vorticity. By comparing the mean velocity contours $\langle u \rangle / U$ of the first three Reynolds numbers, it is found that the region of negative or very low (dark blue) regions become larger with increasing Reynolds number. In the other words, with increasing of Reynolds number, larger separated regions form along the wing. But, this negative region becomes smaller for the highest Reynolds number as shown in Figure A.13. At the same time, a similar effect of Reynolds number as seen on the limit of extension of vorticity and enlargement of the stall region.

Figures A.10, A.12, A.6 and A.14 show patterns of time-averaged streamlines $\langle \Psi \rangle$ (left column) and Reynolds stress correlation $\langle u'v' \rangle / U^2$ (right column) respectively for values of $Re_C$ = 5,976, 17,927, 29,879 and 59,758. The patterns of streamlines in Figure A.10 show an outward spiraling pattern at all spanwise locations, except $\eta$ = 0.3 for the case of $Re_C$ = 5,976. For the other values of $Re_C$ = 17,927, 29,879 and 59,758, at the spanwise location $\eta$ = 0.9, patterns of streamlines are very similar except the width of the regions of upstream-oriented streamlines. Those regions become narrower for the highest Reynolds number. At the spanwise location $\eta$ = 0.8, the center of upstream-oriented streamlines appears at a location upstream of the trailing-edge for $Re_C$ = 17,927, but it forms downstream of the trailing-edge for

higher Reynolds numbers $Re_C$ = 29,879 and 59,758 due to the high free-stream velocity. On the other hand, at the spanwise location $\eta$ = 0.5, upstream-oriented streamlines are observed closer to the leading-edge and the leading-edge separation bubble moves upstream along the surface of the wing with increasing Reynolds number. This inference is confirmed when the Reynolds stress correlations are compared. Increasing Reynolds number advances the onset of negative (green and blue) $<u'v'>/U^2$ towards the leading-edge of the wing. As shown in Figure A.10, the widest regions of high magnitude negative (dark blue) $<u'v'>/U^2$ are viewed at the lowest value of Reynolds number.

Further investigation of the effects of Reynolds number on the flow structure is given in Figures A.15 and A.16. Comparisons of instantaneous patterns of vorticity at four different Reynolds numbers are shown. The concentrations of small-scale vortical structures forming in the separated shear layer are well-defined for all values of $\eta$. As shown in the left column of Figure A.15, for the lowest Reynolds number, the vortex system is relatively coherent and larger-scale structures are present along the wing relative to cases of higher Reynolds number. From the interpretation of the wavelength $\lambda$ between the initially-formed vortices, it is also evident that the wavelength $\lambda$ becomes shorter, and formation of small-scale vortices appears closer to the leading-edge, with increasing Reynolds number. In Figure A.16, it is shown that large regions of more complex vortical structures are present for higher Reynolds numbers. Small-scale vortices in the separated shear layer come together and form a large and complex vortical group.

### *3.3 Comparison of Results with Previous Experimental and Computational Studies*

Figures A.17 through A.19 show comparison of dye visualization versus computational results of AFRL at three values of angle-of-attack $\alpha$ = 6°, 12° and 15°, for a Reynolds number based on mean aerodynamic chord of $Re_C$ = 32,000. As seen in Figure A.17, at $\alpha$ = 6°, a leading-edge vortex system is observed in both images of dye visualization and computed off-body streamlines. It is clearly seen that the leading-edge vortex forms at a location between $\eta$ = 0.5 and 0.3, as shown in dye visualization images. It also forms at a location well downstream of the apex in the computational images. In general, the vortex systems observed in the images of dye visualization and computations are similar. Both have a vortex system, with larger-scale structures present at the wingtip, and the leading-edge vortical structure follows nearly the same trajectory. Small scale vortices are present near the trailing-edge in the images of the computations. In the upper right dye visualization image, a similar structure is seen near the trailing-edge between the plane of symmetry and the spanwise location $\eta$ = 0.5.

Figure A.18 shows comparison of leading-edge vortical structures at angle-of-attack $\alpha$ = 12°. Both dye visualization and computational results show that a stronger and more complex vortical system emanates from the apex at $\alpha$ = 12°, relative to $\alpha$ = 6°. The trajectory and structure of the vortical system seen in dye visualization agree very well with computational results.

For $\alpha = 15°$ case, a considerably different vortical structure emerges, as shown in Figure A.19. Relative to the $\alpha = 6°$ and 12° cases, the vortical system becomes more complex and larger. Moreover, it bifurcates into two distinct vortical structures at a location very close to the apex of the wing. Those bifurcated vortical structures can be also seen in upper left dye visualization image. Furthermore, for the $\alpha = 12°$ and 15° cases, large regions of complex vortical flow appear over a wider area of the wing. As observed in previous cases, at $\alpha = 15°$, dye visualization and computational results show very similar trajectories and structure of the vortical system.

Figures A.20 and A.21 illustrate comparisons of PIV analysis of flow structures presented in this research and previous experimental and computational results of AFRL. Comparison is based on two values of angle-of-attack $\alpha = 6°$ and 12°, and two values of streamwise location $\eta = 0.9$ and 0.3 for a Reynolds number based on mean aerodynamic chord of $Re_C = 32{,}000$. Shown in Figure A.20 are comparisons of the time-averaged patterns of vorticity and Reynolds stress for $\alpha = 6°$. The contours of vorticity and Reynolds stress at $\eta = 0.3$ are very similar in all three set of images. All shows a thin region of reversed flow starting at approximately mid-chord, and negative Reynolds stresses at the trailing-edge. At the spanwise location $\eta = 0.9$, the thickness of negative (blue) regions of velocity appears larger in recent experimental and computational data relative to experimental data obtained by AFRL.

As shown in Figure A.21, which gives a comparison between recent experimental data and computations, contours of streamwise component of velocity

$\langle u \rangle / U$ show good qualitative agreement, while experimental results of AFRL designate a smaller separated region at $\eta$ = 0.9. From the comparison of Reynolds stress contours, it is evident that all sets of images show very similar results. Compared to experimental results, computational data exhibit larger separation region. Additionally, experimental results of AFRL show a slightly earlier separation region, relative to the computations and recent experimental results. At the spanwise location $\eta = 0.3$, very good agreement of Reynolds stress patterns and velocity contours is seen in computations and recent experiments.

## 4. FLOW STRUCTURE ON PERTURBED WING

In order to determine the effectiveness of perturbations on altering the stalled flow patterns, perturbed wing experiments were performed at an angle-of-attack $\alpha$ = 12° where a fully-stalled condition was observed. The value of Reynolds number, based on mean aerodynamic chord was $Re_C$ = 17,927. In addition to $Re_C$ = 17,927, a value of $Re_C$ = 32,000 was used for two values of excitation frequency in order to clarify the effects of perturbations at two different Reynolds numbers.

### *4.1 Time-Averaged Flow Structure*

In Figures AA.1 through AA.14, patterns of time-averaged dimensionless vorticity $\langle\omega\rangle C_{ROOT}/U$, Reynolds stress correlation $\langle u'v'\rangle/U^2$, streamwise component of velocity $\langle u\rangle/U$ and streamlines $\langle\Psi\rangle$ are represented. In Figures AA.1, AA.3, AA.5 and AA.7, the overviews of the time-averaged dimensionless vorticity $\langle\omega\rangle C_{ROOT}/U$ and Reynolds stress correlation $\langle u'v'\rangle/U^2$ are shown. Figures AA.2, AA.4, AA.6 and AA.8 provide patterns of the streamwise component of velocity $\langle u\rangle/U$ and streamlines $\langle\Psi\rangle$. In each set of images, in addition to the pattern corresponding to the stationary wing, the effects of increasing values of excitation frequency $f_e = f_o/8, f_o/4, f_o/2$, and $f_o$ are illustrated. The frequency $f_o$ represents the spanwise averaged value of the inherent instability frequency of small-scale vortex formation in the separated shear layer at the value of $Re_C$ = 17,927. The frequency $f_o$ corresponding to 2.5 Hz was calculated by averaging the values of frequency $f_o^*$ at each spanwise location $\eta$ which are determined using a global spectral analysis of the

unsteady vorticity. The spectrum of the vorticity fluctuation was determined at each of the 3999, 5022, 5096, 5612, and 4876 grid points in the image of the flow field at values of $\eta = 0.3, 0.5, 0.7, 0.8$ and 0.9.

In Figures AA.1, AA.3, AA.5 and AA.7, it can be observed that the patterns of dimensionless vorticity $<\omega>C_{ROOT}/U$, given in the left column indicate that at values of excitation frequency $f_e = f_o/8, f_o/4, f_o/2$, and $f_o$, the extent of the peak (red) regions of vorticity successively decrease at all spanwise locations, relative to the case of the stationary wing. In Figure AA.1, at spanwise location $\eta = 0.9$, for the cases of $f_e = f_o/2$ and $f_o$, it is shown that the initial region of peak (red) vorticity is attached to the leading-edge of the wing, and further downstream, the vorticity layer bifurcates into a higher magnitude region along the surface of the wing, and a lower magnitude region along the locus of the separated shear layer. For all spanwise locations, this bifurcation in vorticity layer occurs earlier at the highest value of excitation frequency $f_e = f_o$ relative to value of excitation frequency $f_e = f_o/2$. The flow structure at successive instants during the oscillation cycle, which are associated with the time-averaged patterns at $f_e = f_o/2$ are addressed subsequently in Figure AA.16. It is noticed that at $\eta = 0.9$, the streamwise extent of the higher level of vorticity along the surface of the wing is largest, and the residual vorticity in the trajectory of separated shear layer is smallest for $f_e = f_o/2$. As shown in Figure AA.7, at $\eta = 0.5$, excitation at $f_e = f_o/2$ eliminates the zone of separation, except for a separation bubble along the surface of the wing. At $f_e = f_o$, the separated region is nearly eliminated.

In the right columns of Figures AA.1, AA.3, AA.5 and AA.7, patterns of Reynolds stress correlation $<u'v'>/U^2$ are shown. For all spanwise locations from $\eta$ = 0.9 to from $\eta$ = 0.5 and for all excitation frequencies $f_e$, it is obviously seen that larger regions of large magnitude (dark blue) $<u'v'>/U^2$ originates toward to the leading-edge of the wing, relative to the case of the stationary wing. Only in spanwise location $\eta$ = 0.9, at higher values of both $f_e = f_o/2$ and $f_o$, alternating patterns of large magnitude negative (dark blue) and positive (dark red) Reynolds stress correlation are generated along the surface of the wing. At the spanwise locations $\eta$ = 0.8 and 0.7, this alternating patterns due to the correlations of irrotational fluctuations induced by the wing motion are observed only for excitation frequency $f_e = f_o$. It is also clearly observed that while the scale of the region of large negative (dark blue) $<u'v'>/U^2$ is larger at spanwise locations $\eta$ = 0.9, 0.8 and 0.7 for the cases of lower excitation frequencies $f_e = f_o/8$ and $f_o/4$, it becomes larger at spanwise location $\eta$ = 0.5 for the cases of higher excitation frequencies $f_e = f_o/2$ and $f_o$ especially in regions near the leading-edge of the wing.

Patterns of time-averaged streamwise velocity $u/U$ are shown in the left columns of Figures AA.2, AA.4, AA.6 and AA.8. At the spanwise locations $\eta$ = 0.9 and 0.8, it is observed that the effect of increasing frequency, up to a value of $f_e = f_o/2$ is to decrease the region of negative or very low (dark blue) streamwise velocity. At those spanwise locations, the flow forms an attached state along the entire streamwise extent of the wing section at $f_e = f_o/2$. At $f_e = f_o$, the effect of the vortical motion induced by the trailing-edge on the concentration of negative $u/U$ is clearly seen in

Figures AA.2, AA.4 and AA.6. This effect can be already seen in the pattern of $<\omega>C_{ROOT}/U$ at $f_e = f_o$ in Figure AA.1 and AA.3. At spanwise locations $\eta = 0.7$ and 0.5, the general effect of increasing values of excitation frequency $f_e$ is a decrease in the spatial extent of the large negative (dark blue) magnitudes as shown in Figures AA.6 and AA.8. When we examine the streamline patterns on the right columns, a region of substantial stall on the stationary wing is very significantly attenuated, relative to the case of the stationary wing, even for the lowest excitation frequency $f_e = f_o/8$ at $\eta = 0.5$.

A highly stalled region above the stationary wing can be detected from the patterns of streamlines given in Figures AA.2, AA.4, AA.6 and AA.8. From Figure AA.2, at $f_e = f_o/8$, a formation of limit cycle pattern of streamlines with an inward spiral towards the focus (center) can be seen. Examining the case of $f_e = f_o/4$, a separation bubble appears at approximately over the mid-chord and the flow reattaches close to the trailing-edge of the wing. At $f_e = f_o/2$, smaller separation bubble forms closer to the leading-edge. For $f_e = f_o$, a very small bubble can be detected on the leading edge and the flow is approximately parallel to the surface of the wing except at the trailing-edge. This form of an outward spiraling pattern is caused by the high frequency motion of the trailing-edge. As shown in Figure AA.4, stationary and $f_e = f_o/8$ cases have similar patterns of streamlines but $f_e = f_o/8$ has smaller stall region over the wing. At $f_e = f_o/4$, an inward spiraling pattern (focus of separation) is monitored over the wing. At $f_e = f_o/2$, a small form of separation bubble appears close to the leading-edge as seen at spanwise location $\eta = 0.9$, but trailing-edge motion highly

affects on the flow at $\eta = 0.8$ in such a way that a second form of separation appears close to the trailing-edge. Compared to spanwise location $\eta = 0.8$, similar patterns of streamlines are seen at $\eta = 0.7$ in Figure AA.6 except for $f_e = f_o/4$ case. For this case, the inward spiraling pattern disappears and a stall region emerges along the wing. At $f_e = f_o/2$, a separation bubble can be still detected very close to the leading-edge. From Figure AA.8, at spanwise location $\eta = 0.5$, it is evident that the separated layer is closer to the surface of the wing, and the spatial extent of separated flow is smaller for all excitation frequencies relative to stationary case. Excitation at $f_e = f_o/2$ eliminates the zone of separation, except for a separation bubble along the surface of the wing. At $f_e = f_o$, the separated region is nearly eliminated.

Due to the sweep of the leading-edge of the wing, the dimensionless magnitude of the unsteady displacement of the leading-edge of the wing $\Delta y_{LE}/C^*$ get a specific value at each spanwise location between 0.03678 and 0.00233 as shown in Figure 3. The minimum deflection of the leading-edge is at $\eta = 0.5$ due to its closeness to the axis of perturbation motion. In Figure 3, values of dimensionless sectional chord length $C^*/C$ are represented for each $\eta$. 3-D model of UCAV 1303 is made of PVC material so computational and experimental measurements of displacement of leading-edge are compared to show effect of bending on the wing due to perturbation motion. Solidworks software was employed to simulate the motion. While blue solid line represents the experimental values, dashed red line represents values of computational simulation. It is seen from the graph that there is a very small deflection between

computational and experimental curves at spanwise locations $\eta = 0.8$ and 0.9 due to bending of the wing.

As a summation of results in Figures AA.1 through AA.8, it can be concluded that the higher values of excitation frequency $f_e = f_o/2$ and $f_o$ are the most effective in altering the flow structure along the sectional chord of the wing in such a way as to promote reattachment of the flow to the wing surface. For stationary wing, at all spanwise locations, it is observed that deflection of the separated shear layer from the surface of the wing is large, and the corresponding region of separated flow has a large extent. Compared to stationary wing, excitation at $f_e = f_o/2$ has no large regions of separated. Moreover, excitation at $f_e = f_o/2$ does not have vortical motion in the vicinity of the trailing-edge compared to excitation at $f_e = f_o$. It is decided that excitation at $f_e = f_o/2$ has the most effective in altering the flow structure and favorable for attenuation of region of substantial stall so the flow structure is addressed in further detail for excitation at $f_e = f_o/2$ in the following.

In Figures AA.11 through AA.14, comparison of the flow structure on the stationary wing section (left column) and excitation at $f_e = f_o/2$ (right column) are shown at five different spanwise sections from $\eta = 0.3$ to 0.9. From Figure AA.11, it can be seen that the streamwise extent of the high magnitude (red) region of $<\omega>C_{ROOT}/U$ is decreased by the excitation at all spanwise locations in comparison with patterns on the stationary wing. At all spanwise locations, the high magnitude (red) region of $<\omega>C_{ROOT}/U$ is formed closer to the wing surface with existence of excitation, relative to its trajectory from the stationary wing. In the other words, the

initial region of the separated shear layer is drawn closer to the wing by the excitation. At $\eta = 0.3$, while a leading-edge separation bubble appears on the stationary wing, it is eliminated by the perturbation.

In Figure AA.12, the comparison of Reynolds stress correlation $<u'v'>/U^2$ is shown for all spanwise locations $\varepsilon$. The effect of excitation is to substantially advance the onset of high magnitude negative (dark blue) $<u'v'>/U^2$ towards the leading-edge of the wing, relative to the corresponding patterns on the stationary wing. Moreover, the high magnitude negative (dark blue) region is formed closer to the wing surface with existence of excitation. At $\eta = 0.3$ close to the plane of symmetry, only a small-scale leading-edge separation bubble is formed and high magnitude negative (dark blue) Reynolds stress is not generated.

Figures AA.13 compares patterns of time-averaged streamwise velocity $u/U$. For all spanwise locations $\eta$, the region of negative or very low (dark blue) streamwise velocity is eliminated in presence of excitation. Therefore, the large stall region on the stationary wing is attenuated and an attached form of flow is observed along the entire streamwise extent of the wing section. At spanwise locations $\eta = 0.8$ and 0.7, the effect of the vortical motion induced by the trailing-edge on the concentration of negative $u/U$ is clearly seen.

From the patterns of time-averaged streamlines, as shown in Figure AA.14, the spatial extent of regions of large-scale flow separation is significantly reduced and, furthermore, regions of upstream-oriented streamlines, so prevalent on the stationary wing is no longer evident. At values of $\eta = 0.7$, 0.8 and 0.9, a small-scale, leading-

edge separation bubble persists and, at $\eta$ = 0.5, the location of this bubble moves downstream along the surface of the wing. At $\eta$ = 0.3, the leading-edge separation bubble is eliminated.

### *4.2 Instantaneous and Phase-Referenced Flow structure*

Figures AA.15 through AA.23 show patterns of phase-averaged vorticity over an entire oscillation cycle at spanwise locations $\eta$ = 0.9, 0.7 and 0.5 respectively for the cases of the wing perturbed at frequencies $f_e = f_o/4$, $f_o/2$ and $f_o$. The instantaneous vertical displacement of the leading-edge of the wing is designated as $h(t)$ in the schematic. Each image has a specified value of $t/T$, in which $t$ is time and $T$ is the period of the wing motion. In each figure, the image at the upper left corresponds to the maximum-positive displacement and that at the upper right represents the maximum-negative displacement. In the following, the cases of stationary and the most effective frequency $f_o/2$ are examined in further detail.

Figure AA.29 shows patterns of instantaneous and phase-averaged vorticity for the case of the stationary wing. In each pattern of instantaneous vorticity, the location of the first pronounced concentration of vorticity formed in a separated shear layer served as the phase-reference. Small-scale vortical structures form in the separated shear layer. For all values of $\eta$, the concentrations are well-defined. The images of Figure AA.29 provide a basis for interpretation of the wavelength $\lambda$ between the initially-formed vortices, normalized by the mean aerodynamic chord $C$,. i.e.,$\lambda/C$ = 0.065, 0.072, 0.076 and 0.11 at values of $\eta$ = 0.5, 0.7, 0.8 and 0.9. These values of wavelength may also be normalized with respect to the sectional chord $C^*$ at each

value of $\eta$. With this normalization, $\lambda/C^{*}$ = 0.11, 0.17, 0.21 and 0.43 for the respective values of $\eta$ indicated in the foregoing. These images of the vortex pattterns in Figure AA.29 provide a basis for comparison with corresponding patterns of vorticity for the perturbed wing, which can be fundamentally different.

For the case of excitation at $f_e = f_o/2$, as shown in Figure AA.16, at $t//T = 0$, an extended layer of vorticity exists along nearly the entire chord and close to the surface of the wing. High magnitude (red) vorticity layer appears in the vicinity of the leading-edge. This overall pattern persists at $t/T$ = 0.1 and 0.2, while the previously formed concentration of vorticity, represented by the large (green-yellow) cluster, continues to translate downstream. At $t/T$ = 0.3, the elongated layer of high magnitude (red) vorticity in the vicinity of the leading-edge starts to partition into two discrete concentrations, and this process continues at $t/T$ = 0.4, 0.5 and 0.6. At $t/T$ = 0.7, the segregation of vorticity concentrations is complete, and the larger-scale concentration starts to move along the trajectory of the separated shear layer, while the concentration in the vicinity of the leading-edge becomes increasingly elongated, and eventually merges into the layer that extends along the entire surface of the wing. The bifurcation of the time-averaged pattern of vorticity shown in Figure AA.1 therefore involves: the averaged consequence of discrete vortical structures originating from that portion of partitioned vorticity shed from the surface of the wing; and the averaged form of that region of the partitioned vorticity that remains along the surface of the wing. As suggested by a reviewer, it is possible that reattachment in planes located in board of the plane of interest contributes to the wall vorticity layer of Figure 6.

The overview of Figure AA.24 shows the effect of excitation frequency $f_e = f_o$, $f_o/2$ and $f_o/4$ at $\eta = 0.9$. Images in the left column are phase-referenced according to the appearance of cluster *a* at the same location. The right column of Figure AA.24 shows images one-half cycle later. At $f_e = f_o$ and $f_o/2$, in the left column of images at $t = t_r$, an elongated region of high level (red) vorticity is formed along the leading-edge. At $f_e = f_o$, this high level layer becomes part of a lower level layer that exists over approximately one-half chord of the wing. At $f_e = f_o/2$, the lower level layer exists over the entire chord of the wing. Moreover, at $f_e = f_o$, a concentration of vorticity exists in the separated layer between the leading-edge and cluster *a*. On the other hand, at $f_e = f_o/2$, no such concentration exists in the separated layer; rather, it appears to remain attached to the surface of the wing as part of the high concentration (red) layer at the leading-edge. Furthermore, the images at $t_e = t_r + T_e/2$ shows that, at $f_e = f_o$, the vorticity concentration leaves the surface at the leading-edge, whereas at $f_e = f_o/2$, its departure is delayed until about one-third chord. This delay in departure no doubt contributes to the extension of the surface vorticity layer over the entire chord of the wing section. Finally, at the low value of excitation frequency $f_e = f_o/4$ in Figure AA.24, well-defined, smaller-scale vorticity concentrations are not formed in the immediate vicinity of the leading-edge. The large-scale concentration *a* represents an agglomeration of vorticity in the separated shear layer.

Figure AA.26 shows the patterns of vortex formation at $\eta = 0.5$. As in Figure AA.24, concentrations of vorticity designated as *a* serve as the phase-reference. At all values of excitation frequency, the region of high magnitude (red) vorticity is formed

at the leading-edge is significantly reduced in spatial extent, relative to the case of the stationary wing. Furthermore, the initially formed concentration $a$ has a significantly reduced value of peak vorticity. These initial concentrations of $a$ in presence of excitation are located closer to the surface of the wing section than for the stationary wing. As represented by the images in the right column of Figure AA.26, the vortical activity close to the surface of the wing section is particularly evident at excitation frequencies $f_e = f_o$ and $f_o/2$. These observations are associated with a substantial reduction in the extent of the region of flow separation, as indicated in Figure AA.14.

In the foregoing, a range of excitation frequency has been considered, and these frequencies are represented by the inherent instability frequency $f_o$ averaged along the span, and its subharmonics. High-frequency excitation of flat delta wings is addressed in the investigation of Vardaki et al. (2008). They found that the most effective frequencies, for inducement of flow reattachment, were in the range $fC/U = 1$ to 2. The present configuration is a substantial departure from a flat delta wing, that is, the existence of the crank configuration of the trailing-edge yields unusual variations of sectional chord $C^*$ as a function of dimensionless spanwise location $\eta$. Furthermore, the central portion of the wing is thick and the flow is essentially attached in that region, A well-defined separated shear layer exists at the spanwise locations in the outboard region, $\eta$ = 0.5, 0.7, and 0.9. So, direct comparison of the most effective frequencies of a flat delta wing and the high of the three-dimensional configuration of interest herein should be done with caution. If the fundamental frequency $f_o$ is employed as a basis for comparison, the dimensionless frequencies based on local

chord $C^*$ are $f_o C^*/U = 4.86, 2.56$ and $1.44$ at $\eta = 0.5, 0.7$, and $0.9$. On the other hand, if one views excitation at the subharmonic component $f_o/2$ as the most effective frequency, then the corresponding dimensionless frequencies are 2.43, 1.28, and 0.72 at $\eta = 0.5, 0.7$, and 0.9. These dimensionless frequencies are of the same order as those determined by Vardaki et al. (2008) for the flat delta wing.

## 5. CONCLUSIONS

The main goal of this study was to quantitatively characterize the flow structure along the 1303 UCAV configuration as a function of both angle-of-attack and Reynolds number. Evaluation of the results obtained from stationary wing experiments led to a study that focused on control of the flow structure at high angle-of-attack. An open-loop active control technique was employed to induce controlled perturbations of the wing. The flow structure along both the stationary and perturbed wing were determined in terms of patterns of mean velocity, vorticity, streamlines and Reynolds stress, in conjunction with dye visualization.

For the case of the stationary wing, a dominant region of separated flow, i.e., stall, was observed in the outboard part of the wing. The scale of the stall region increases and extends to the inboard region of the wing with increasing angle-of-attack. Regarding the effects of Reynolds number, in general, it was found that the scale of the stall region increases with increasing Reynolds number. There appears, however, to be a limiting value of Reynolds number for attaining enlargement of the stall region. Moreover, the leading-edge separation bubble moves upstream along the surface of the wing with increasing Reynolds number. When fully separated flow occurs, instantaneous patterns of vorticity show that, for increasing Reynolds number, smaller-scale vortical structures are present in the separated layer. Correspondingly, the wavelength $\lambda$ between the initially-formed vortices becomes smaller, and their onset occurs closer to the leading-edge.

A global spectral analysis of the unsteady vorticity in the separated shear layer from the leading-edge of the stationary wing provided the spanwise-averaged frequency of the natural instability. Small amplitude perturbations (0.45 degrees) were applied over a range of frequencies corresponding to the fundamental and subharmonics of the inherent instability frequency. In order to understand the flow physics arising from perturbations of the flow structure, various representations of the phase- and time-averaged flow structure were determined and analyzed in detail. The principal findings are as follows.

1. Time-averaged patterns of streamwise velocity and streamline topology indicate that excitation at either the fundamental or subharmonic of the inherent instability frequency is particularly effective in altering the flow structure at high angle-of-attack. It is possible to nearly eliminate large-scale stalled regions, and attain reattachment of the flow, except for smaller-scale separation bubbles.
2. The foregoing reduction in spatial extent of the separation zone is accompanied by: a substantial reduction in the streamwise extent of the high-magnitude, time-averaged vorticity in the separating shear layer; and an increase in magnitude of the Reynolds stress, as well as advancement of the regions of high Reynolds stress towards the leading-edge of the wing.
3. The physical mechanisms associated with the preceding changes have been characterized in terms of patterns of phase-averaged vorticity, acquired during the oscillation cycle of the wing perturbation. In essence, a layer of high-magnitude vorticity attached to the leading-edge is partitioned into two regions: one part

forms a sequence of discrete clusters of vorticity shed from the surface of the wing; and the other part merges into the vorticity layer along the surface of the wing. For the latter, its streamwise extent is related to the delay in departure of the vorticity concentration from the surface, which is a function of the excitation frequency. All of the foregoing features are sectional cuts of three-dimensional flow structures. In future investigations, it would be insightful to address the degree to which three-D features are significant.

4. The foregoing conclusions focus on the response to excitation at the fundamental and first subharmonic of the inherent instability frequency of the separating shear layer. It is possible, however, to induce significant changes of the time-averaged patterns of the flow structure, even when the excitation frequency is well separated from the inherent instability frequency, e.g., a value as low as one-eighth of this frequency and, for transverse displacements of the leading-edge as small as 0.2 percent of the local chord. This finding indicates that very small, self-excited elastic perturbations of the wing, or small perturbations in the inflow, can significantly alter the time-averaged flow structure.

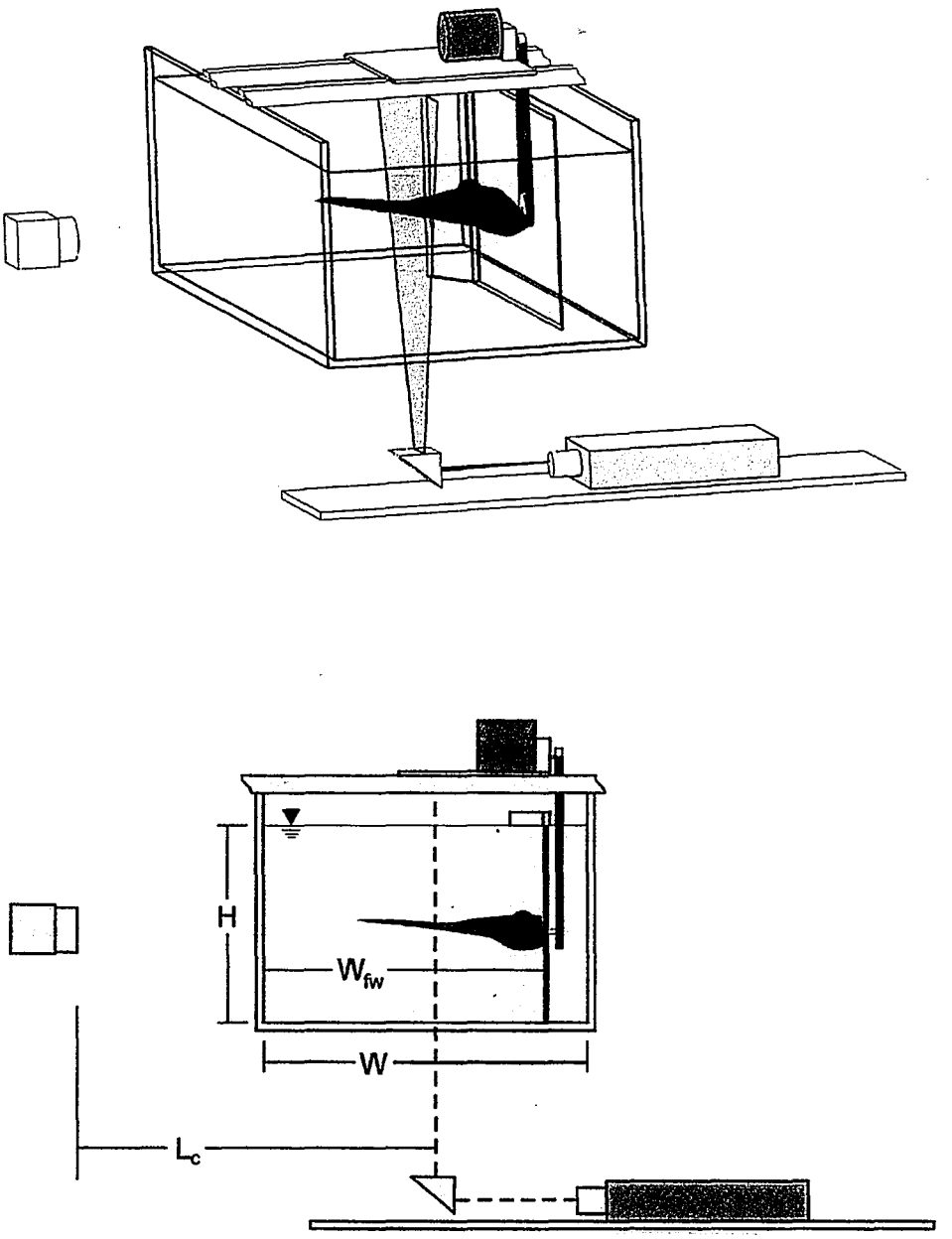


**Figure 1a**: Overview of experimental system showing arrangement for particle image velocimetry system in relation to half- wing mounted in water channel.

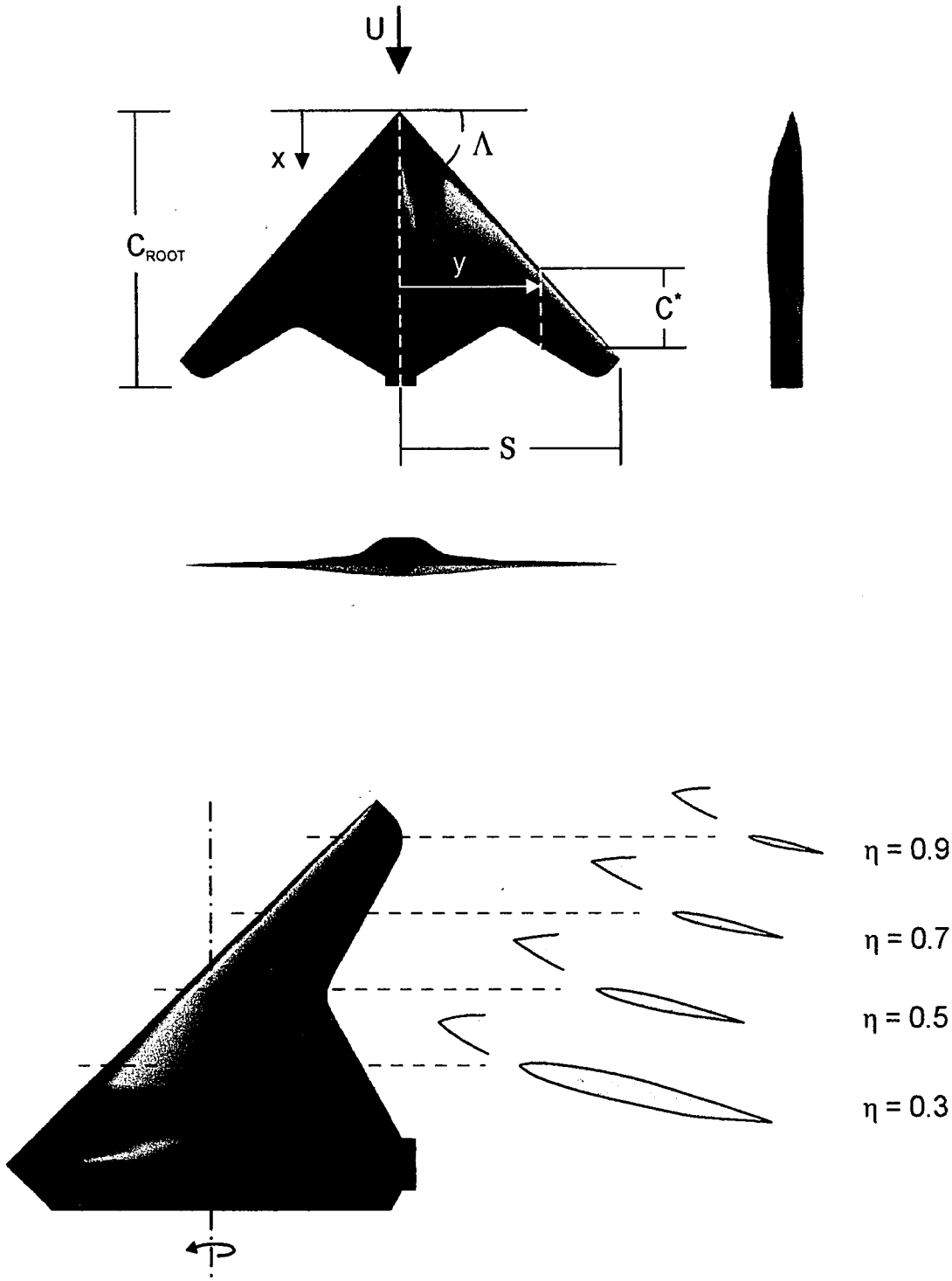


**Figure 1b**: Definitions of parameters and zoomed-in views of half wing in relation to full wing.

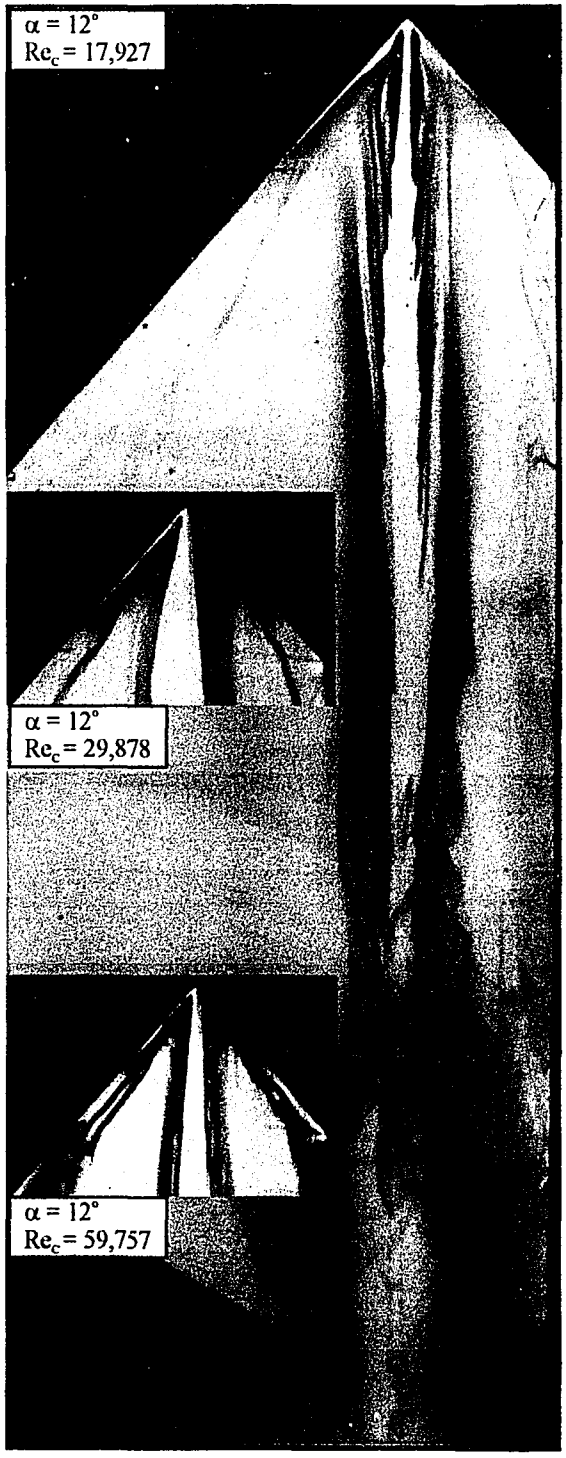


**Figure 1c**: Dye visualization of flow pass center body and APEX region of wing

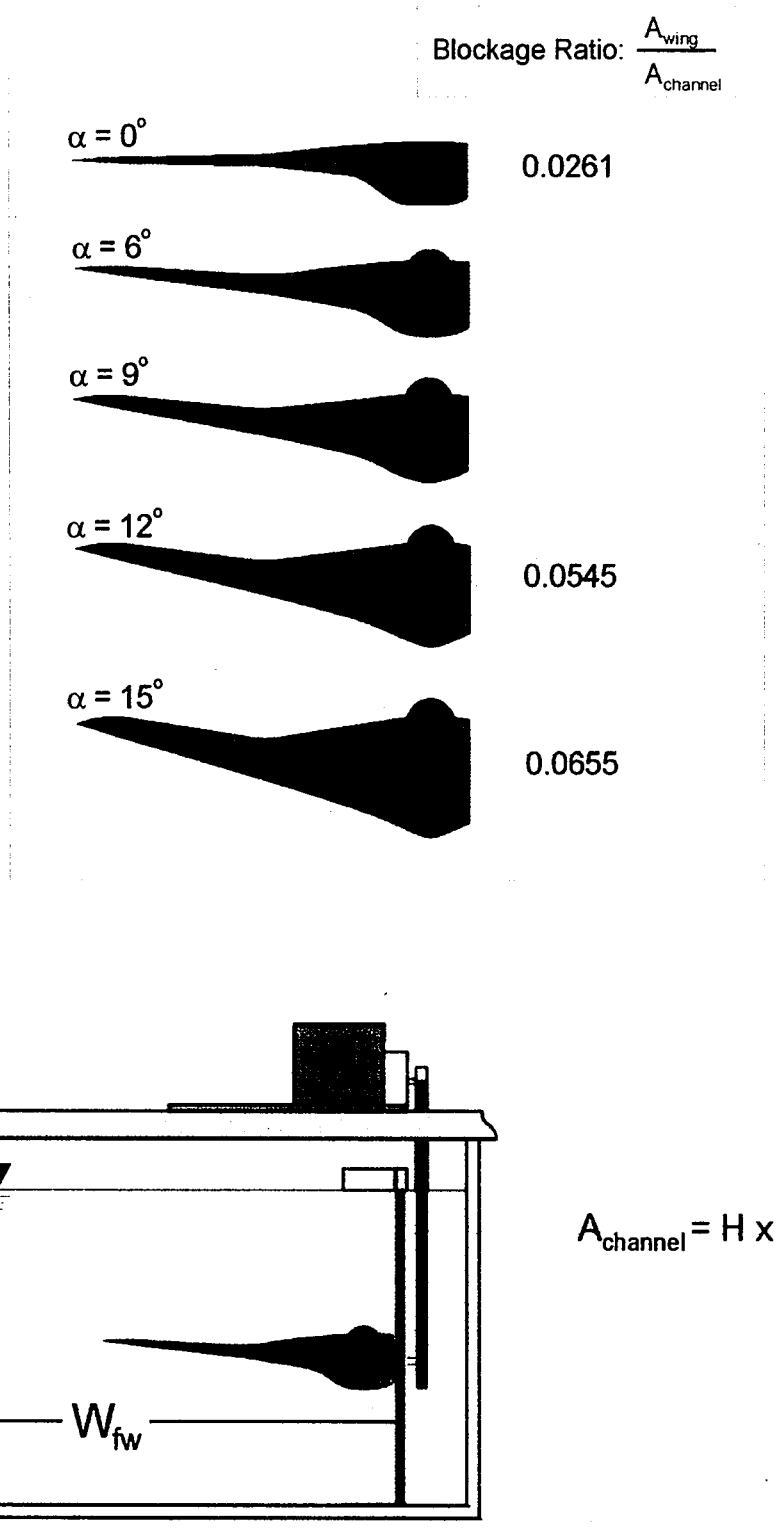


**Figure 2**: Illustration of projected wing area as a function of angle-of-attack, which is used in calculation of the blockage ratio.

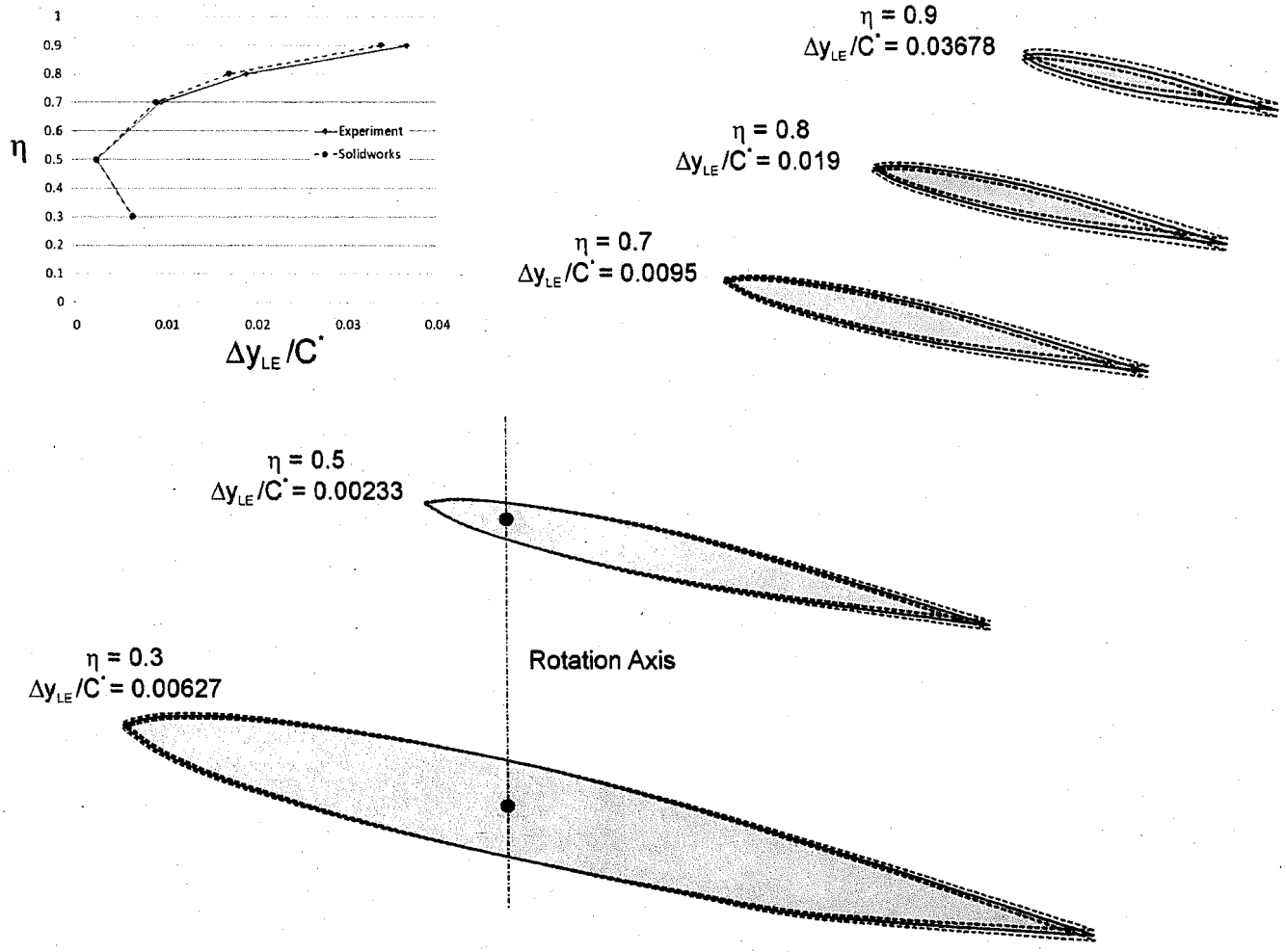


**Figure 3**: Extreme positions of wing section during small-amplitude perturbations of angle-of-attack of 0.45 degrees, at various spanwise locations along the three-dimensional wing.

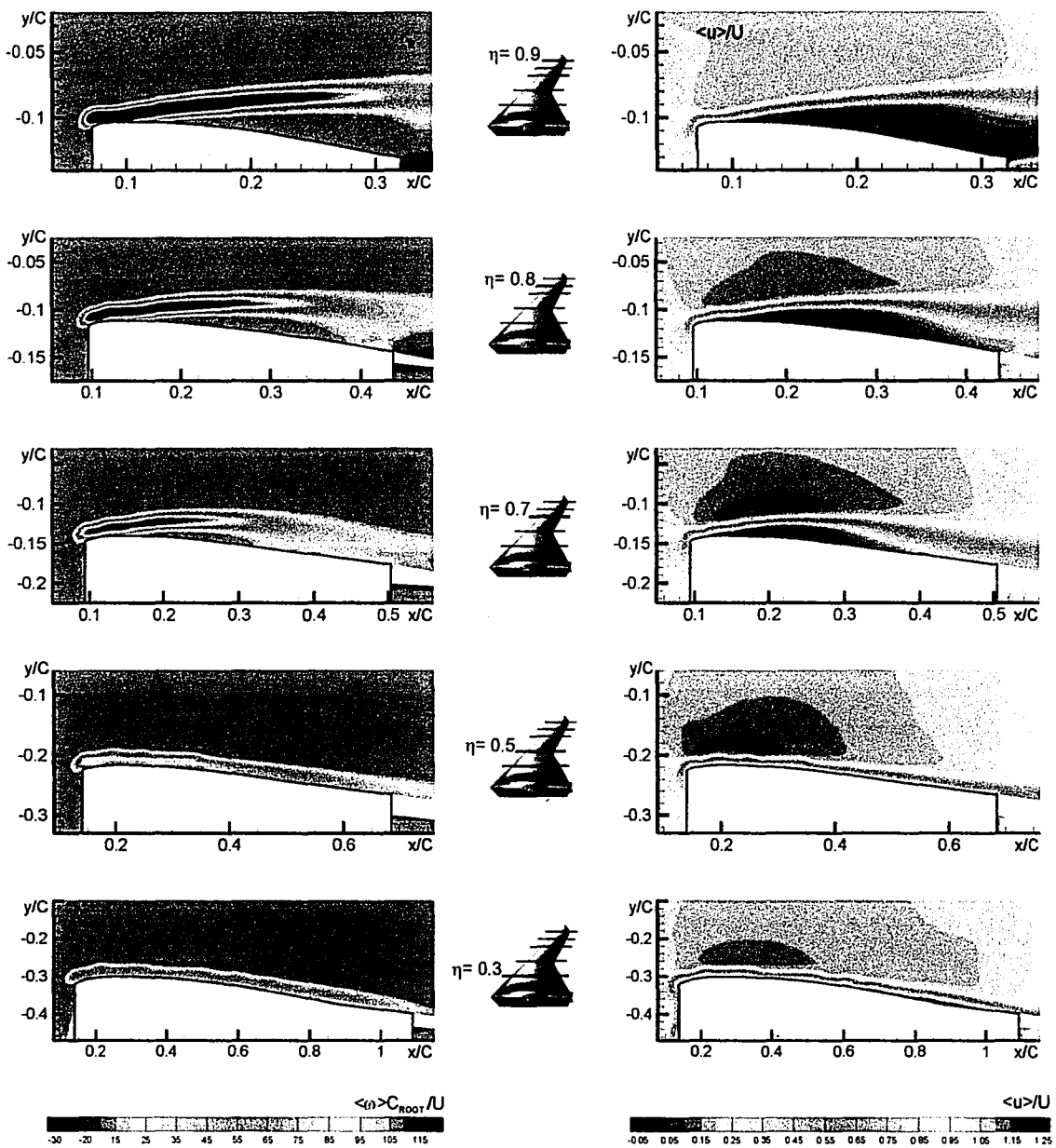


**Figure A.1**: Time-averaged vorticity and streamwise velocity component for stationary wing at angle-of-attack $\alpha = 6^{\circ}$. Reynolds number based on mean aerodynamic chord is $Re_c = 29879$.

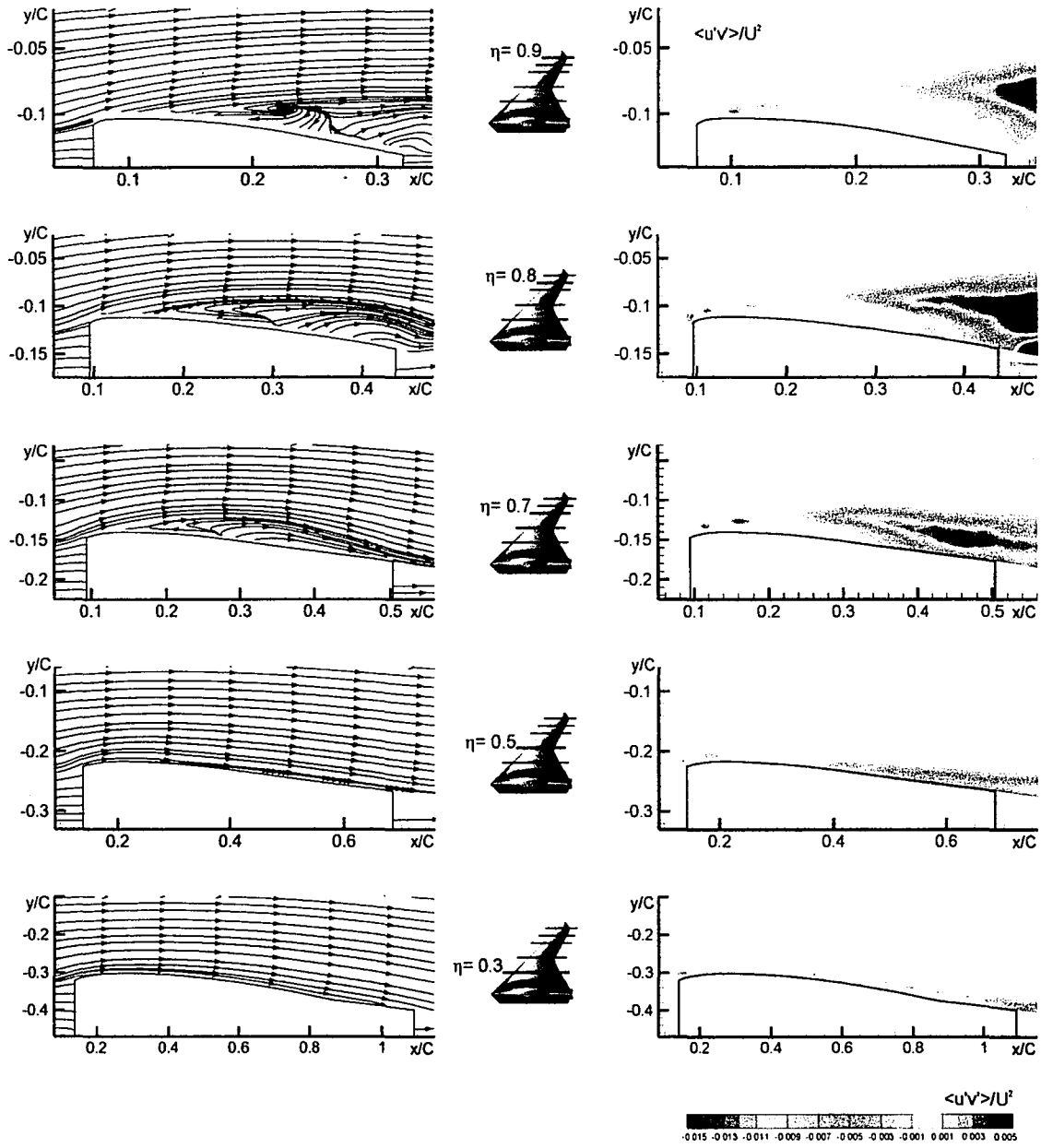


**Figure A.2**: Time-averaged streamlines and Reynolds stress correlation for stationary wing at angle-of-attack $\alpha = 6°$. Reynolds number based on mean aerodynamic chord is $Re_c = 29879$.

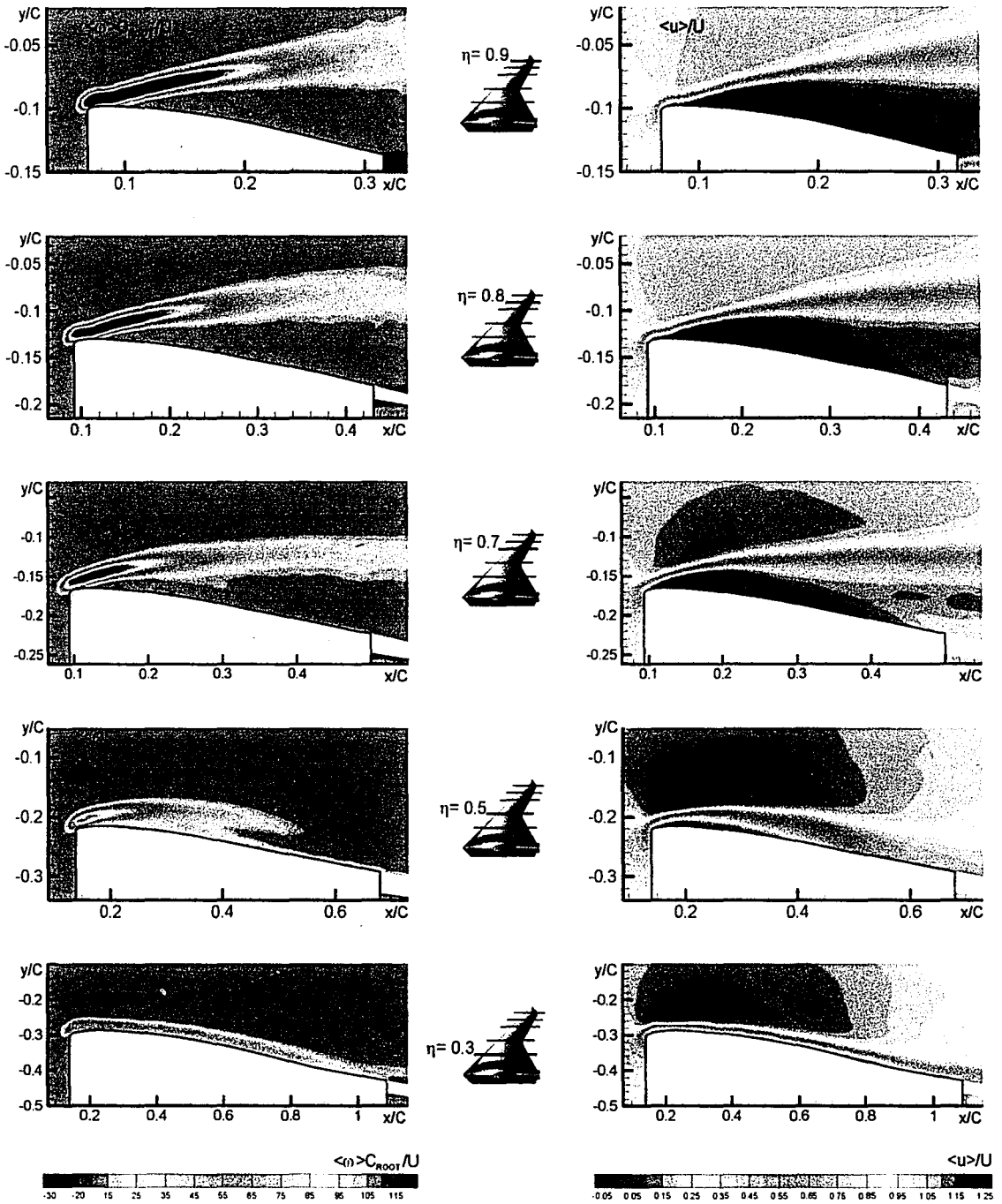


**Figure A.3**: Time-averaged vorticity and streamwise velocity component for stationary wing at angle-of-attack $\alpha = 9°$. Reynolds number based on mean aerodynamic chord is $Re_c = 29879$.

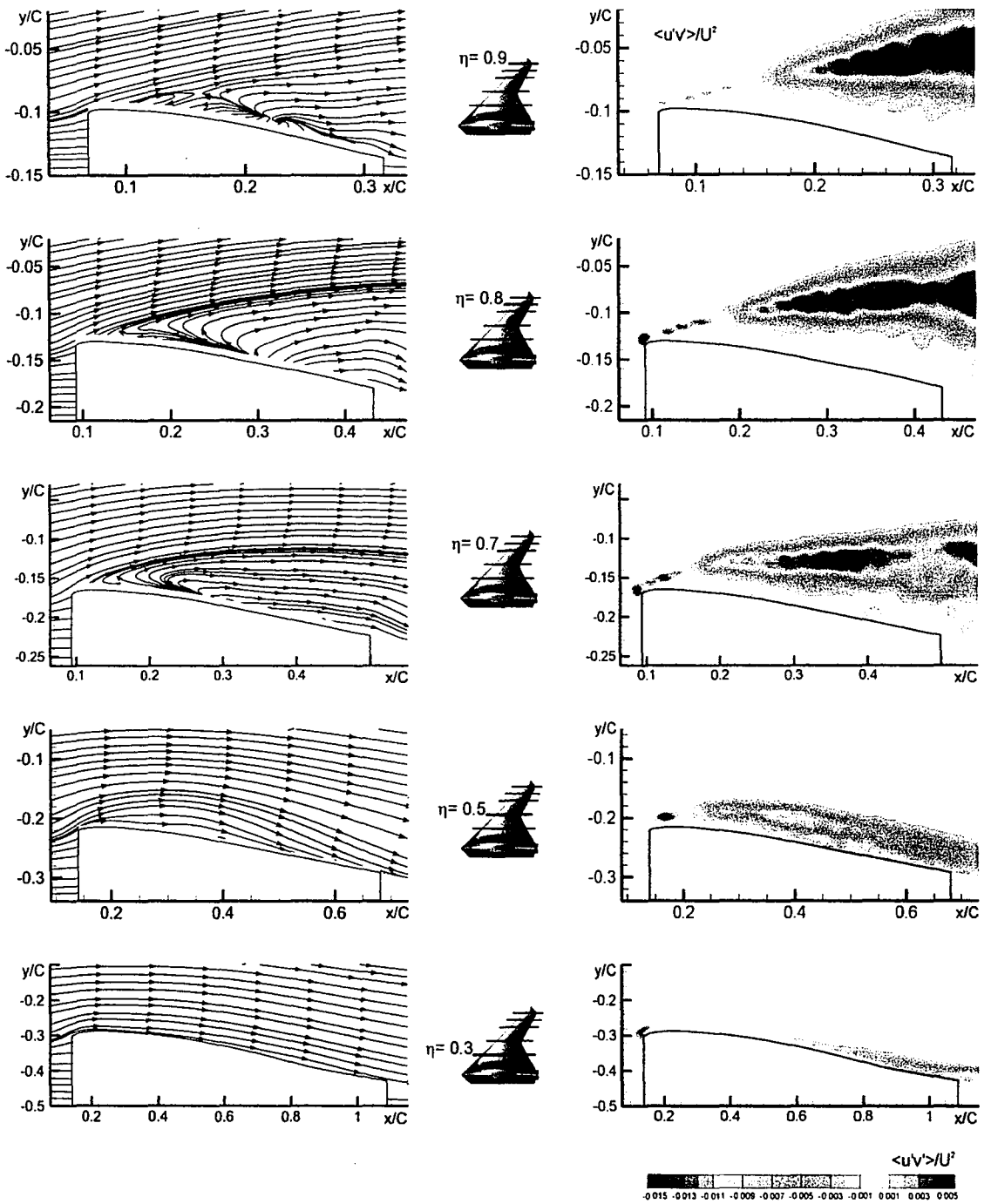


**Figure A.4**: Time-averaged streamlines and Reynolds stress correlation for stationary wing at angle-of-attack $\alpha = 9°$. Reynolds number based on mean aerodynamic chord is $Re_c = 29879$.

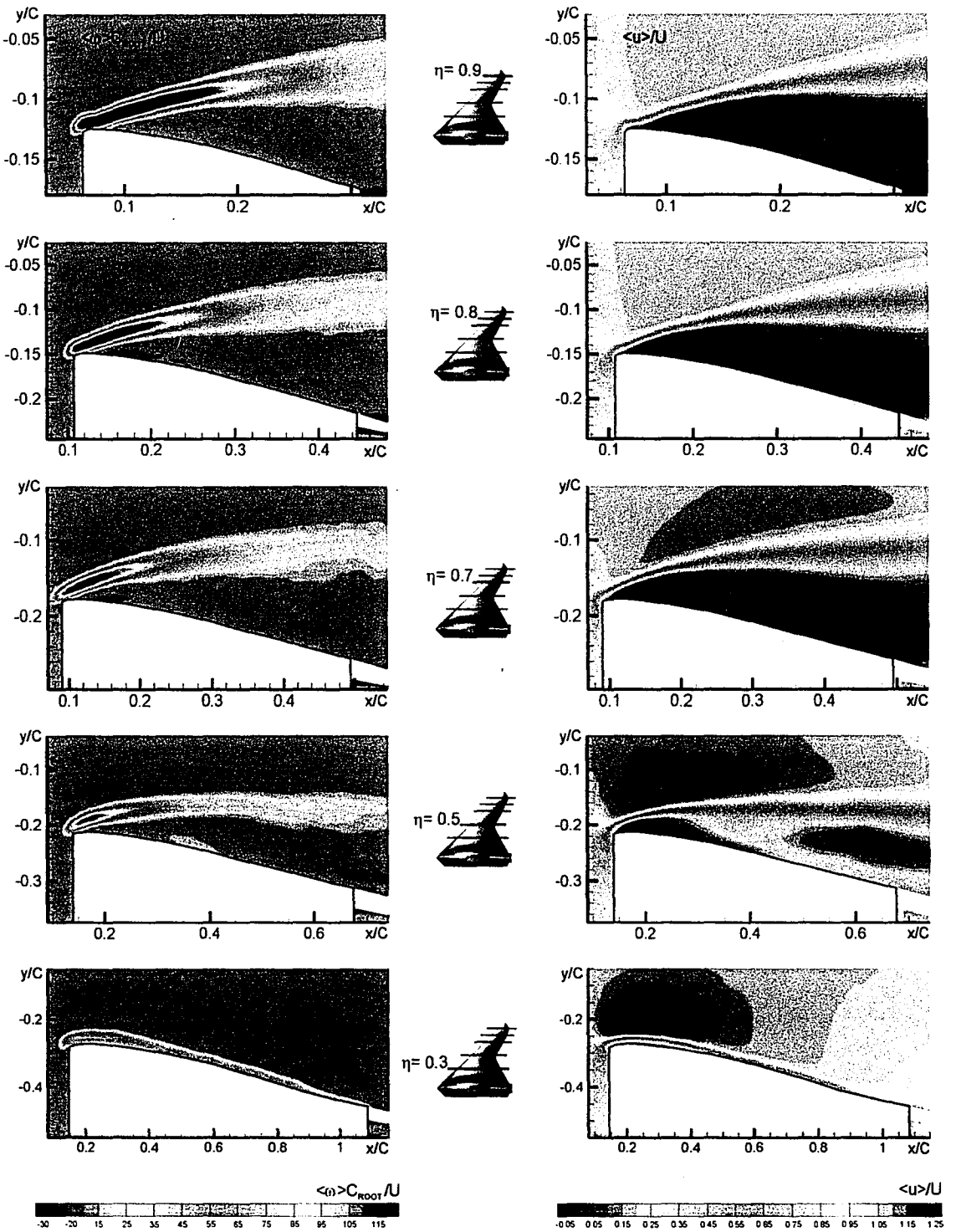


**Figure A.5**: Time-averaged vorticity and streamwise velocity component for stationary wing at angle-of-attack $\alpha = 12°$. Reynolds number based on mean aerodynamic chord is $Re_c = 29879$.

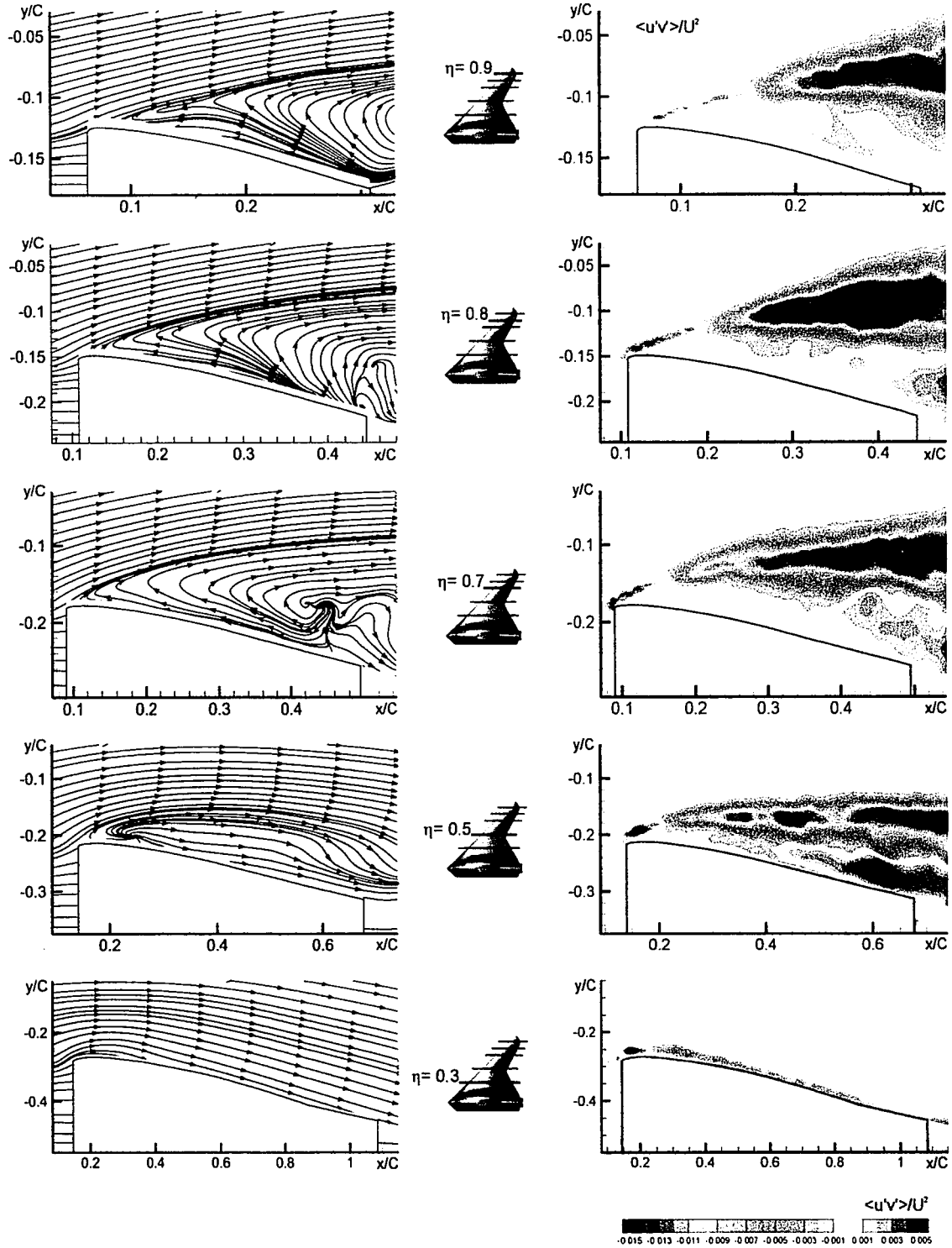


**Figure A.6**: Time-averaged streamlines and Reynolds stress correlation for stationary wing at angle-of-attack $\alpha = 12°$. Reynolds number based on mean aerodynamic chord is $Re_c = 29879$.

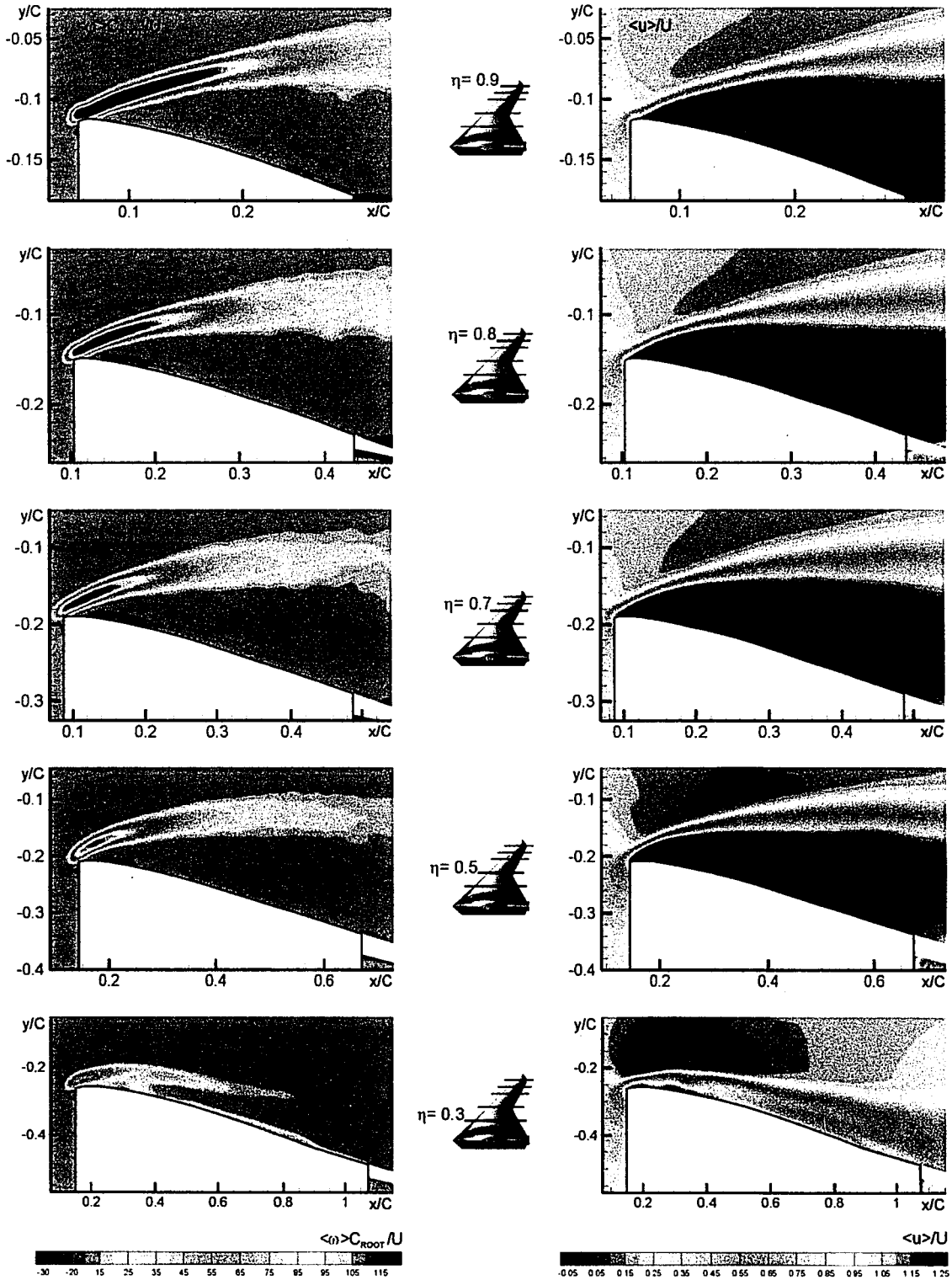


**Figure A.7**: Time-averaged vorticity and streamwise velocity component for stationary wing at angle-of-attack $\alpha = 15°$. Reynolds number based on mean aerodynamic chord is $Re_c = 29879$.

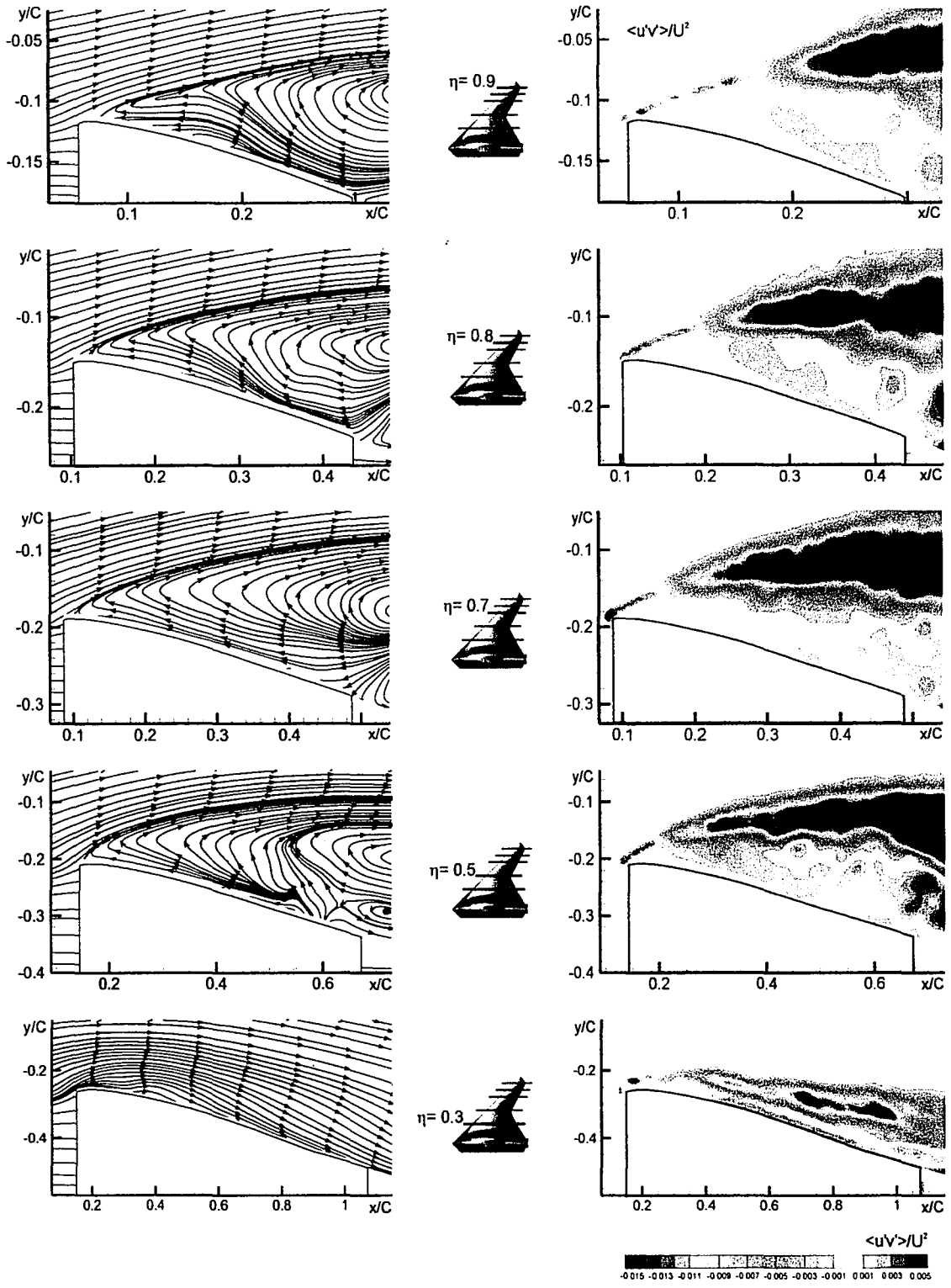


**Figure A.8**: Time-averaged streamlines and Reynolds stress correlation for stationary wing at angle-of-attack $\alpha = 15°$. Reynolds number based on mean aerodynamic chord is $Re_c = 29879$.

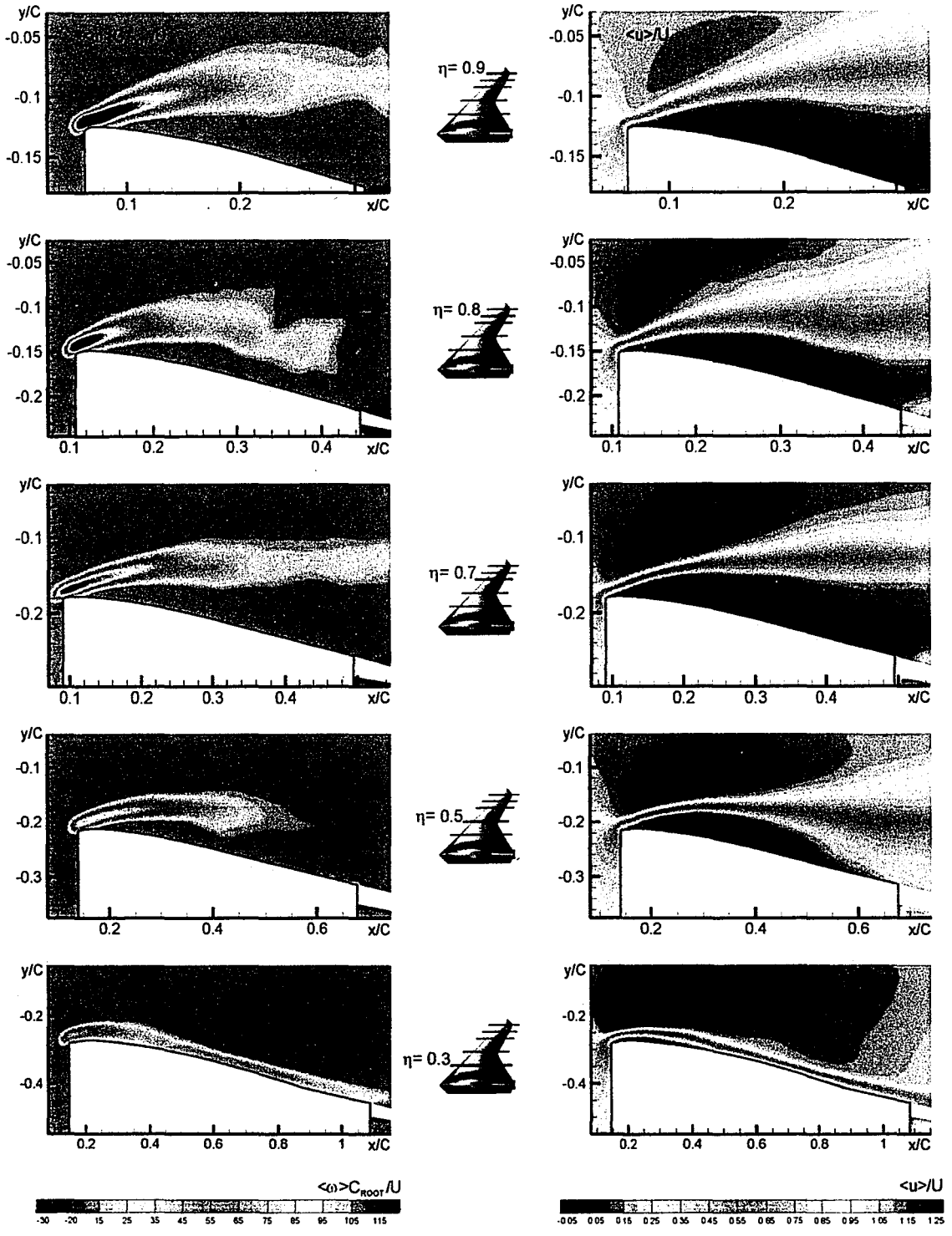


**Figure A.9**: Time-averaged vorticity and streamwise velocity component for stationary wing at angle-of-attack $\alpha = 12°$. Reynolds number based on mean aerodynamic chord is $Re_c = 5976$.

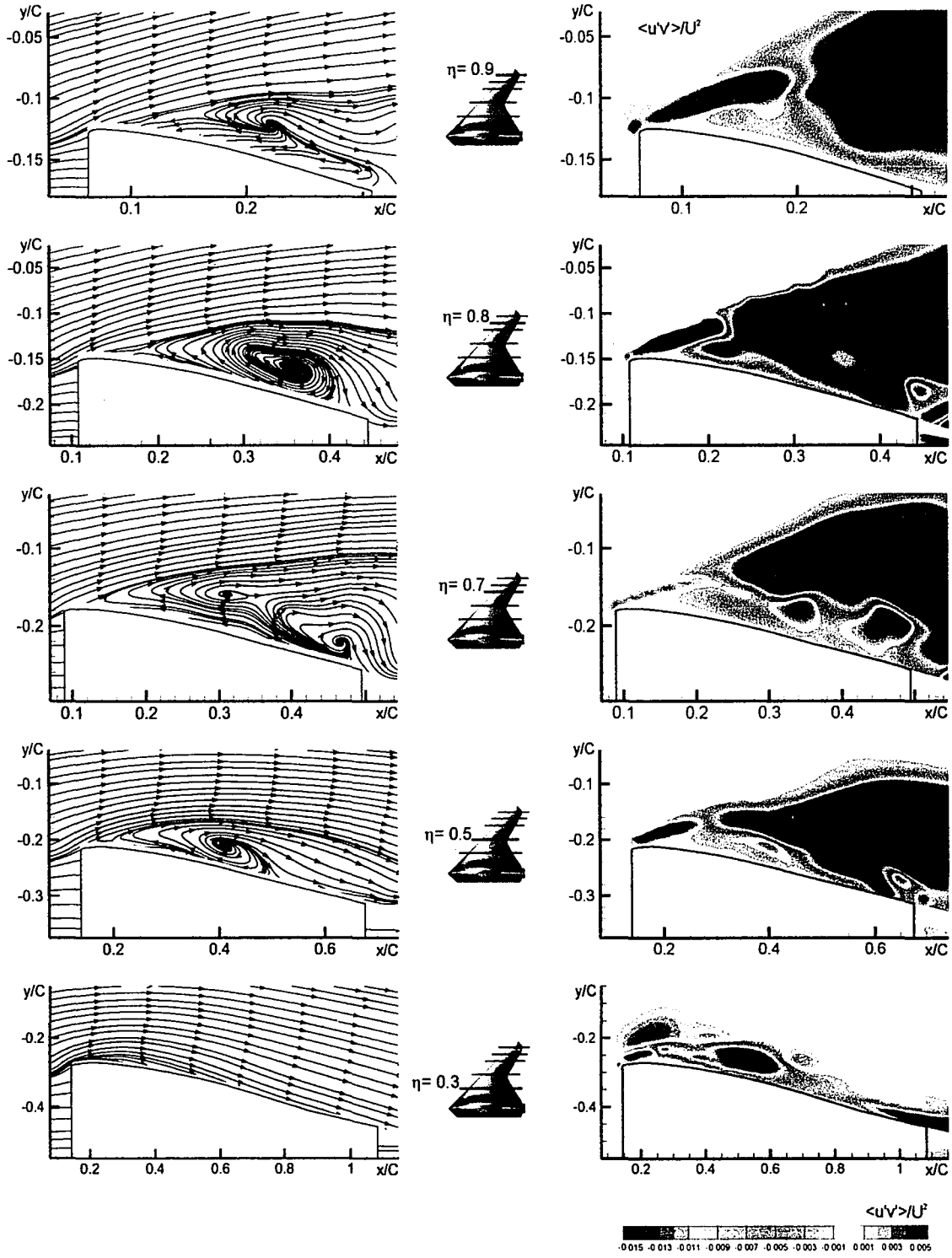


**Figure A.10**: Time-averaged streamlines and Reynolds stress correlation for stationary wing at angle-of-attack $\alpha = 12°$. Reynolds number based on mean aerodynamic chord is $Re_c = 5976$.

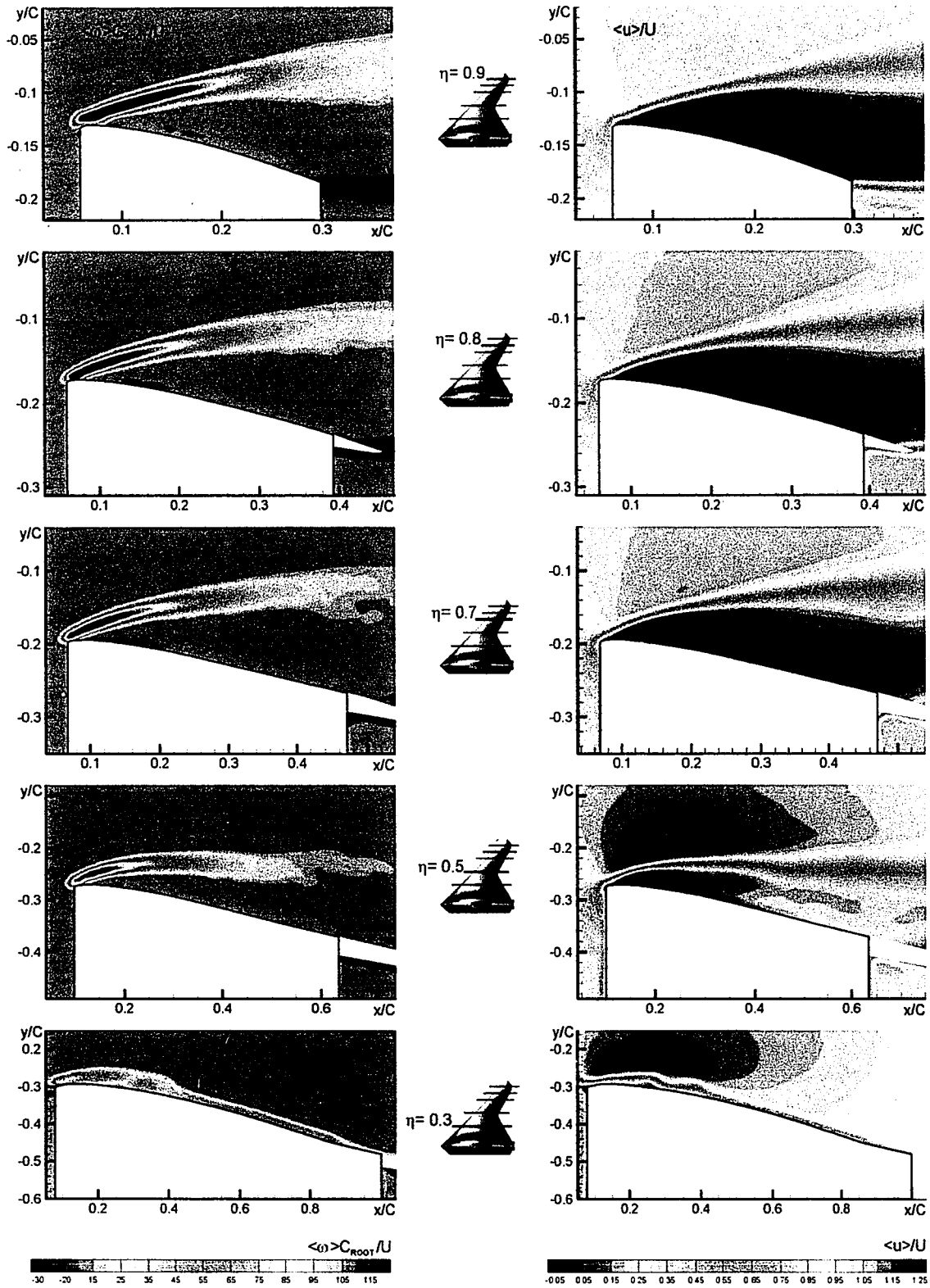


**Figure A.11**: Time-averaged vorticity and streamwise velocity component for stationary wing at angle-of-attack $\alpha = 12°$. Reynolds number based on mean aerodynamic chord is $Re_c = 17927$.

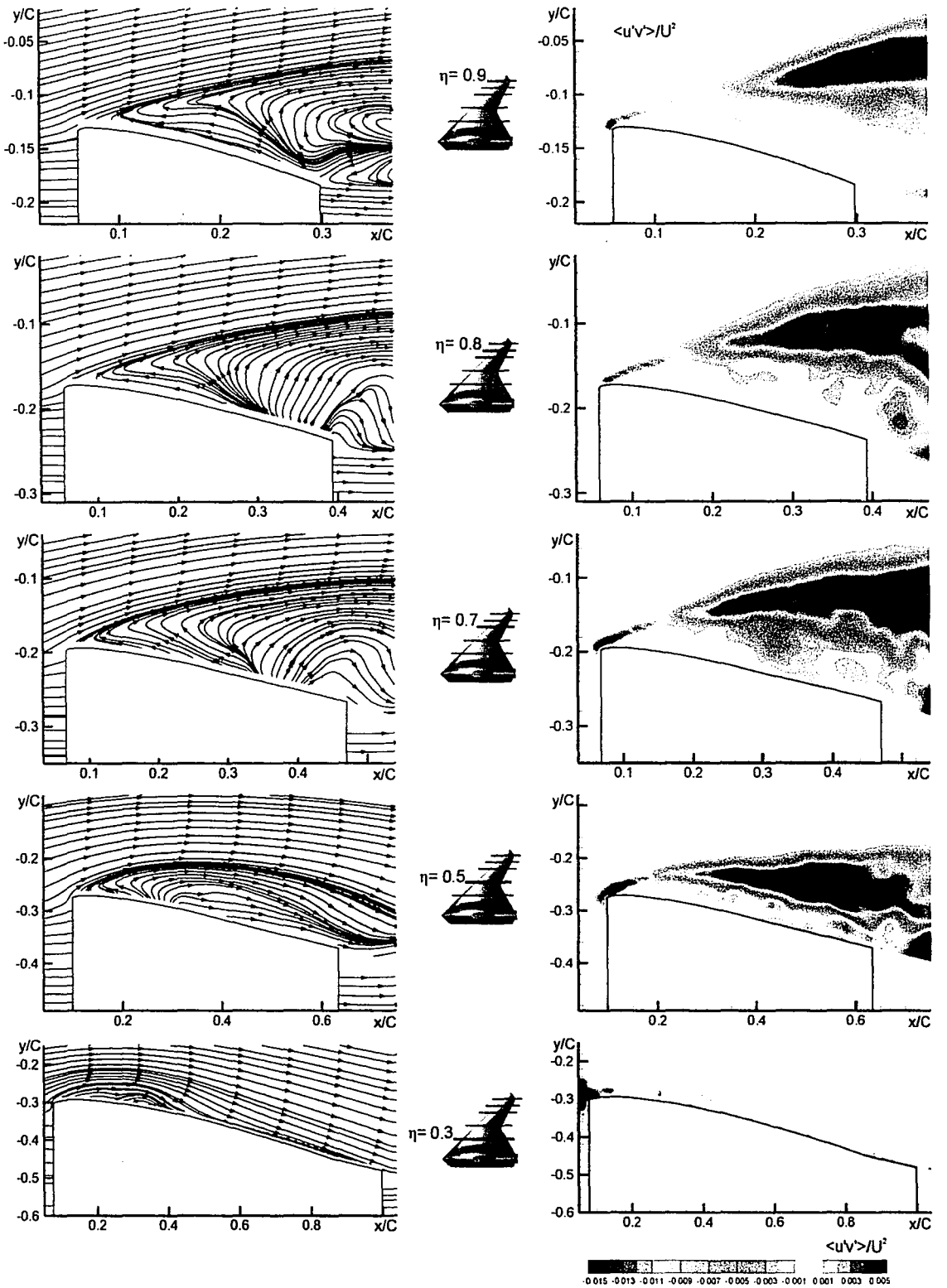


**Figure A.12**: Time-averaged streamlines and Reynolds stress correlation for stationary wing at angle-of-attack $\alpha = 12°$. Reynolds number based on mean aerodynamic chord is $Re_c = 17927$.

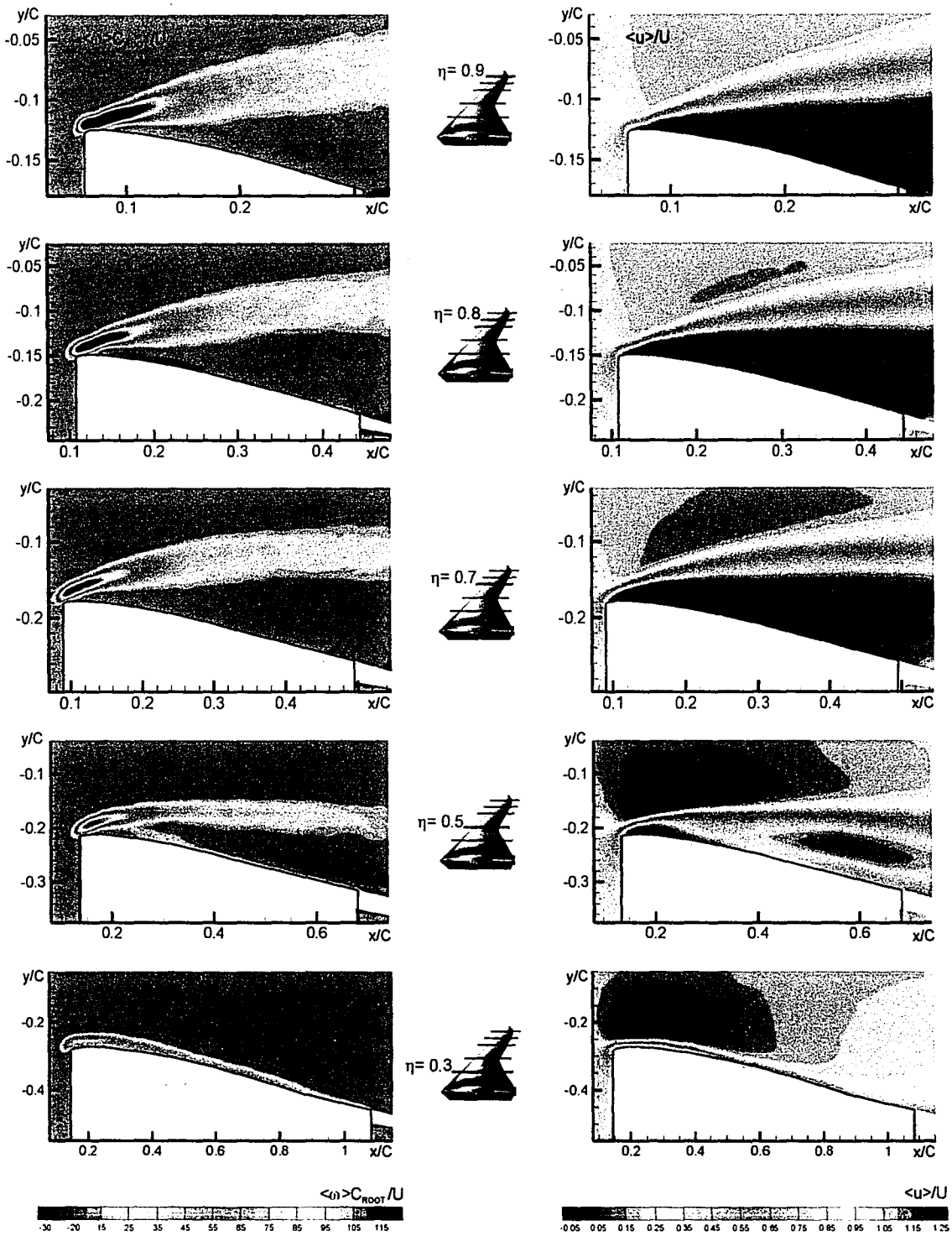


**Figure A.13**: Time-averaged vorticity and streamwise velocity component for stationary wing at angle-of-attack $\alpha = 12°$. Reynolds number based on mean aerodynamic chord is $Re_c = 59758$.

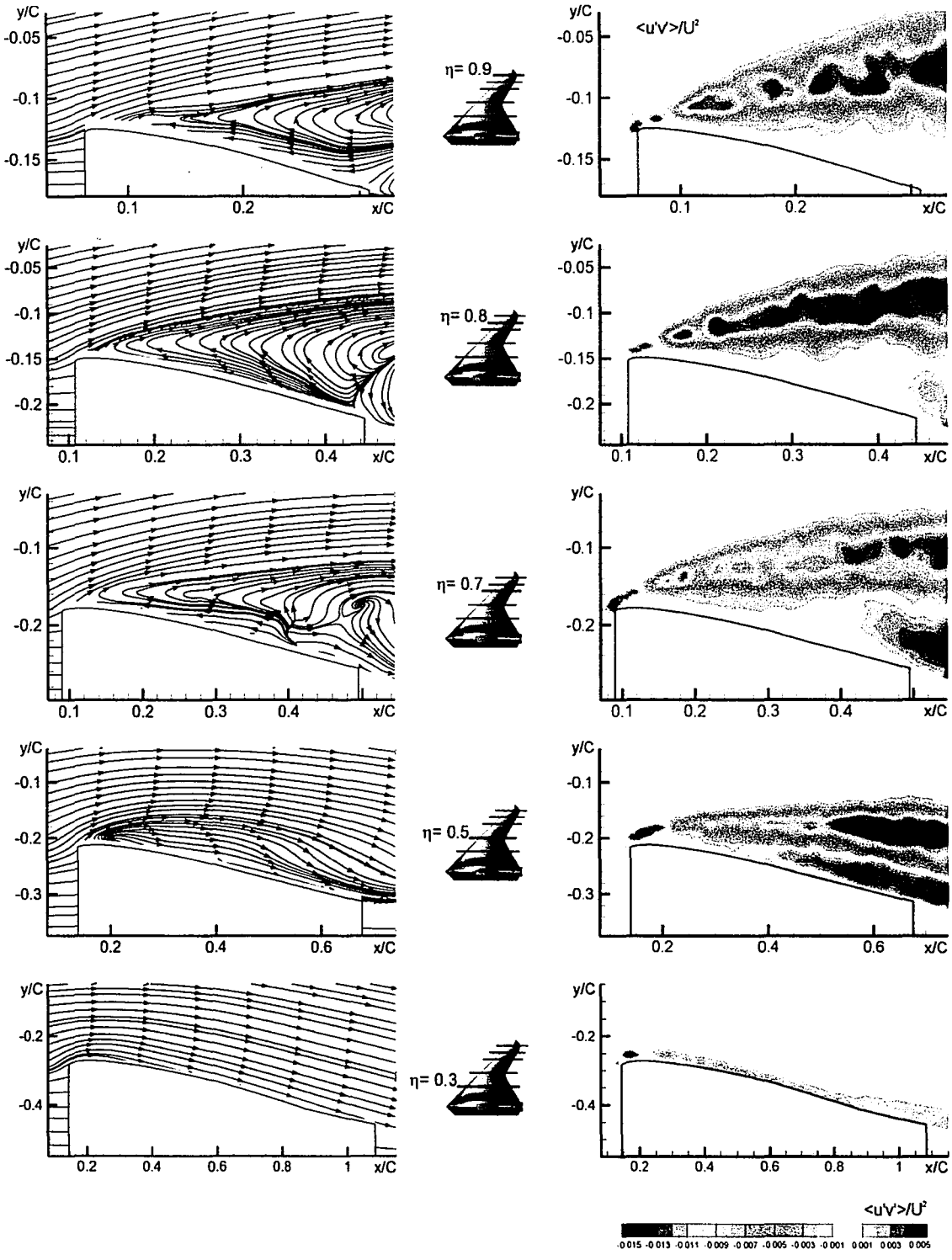


**Figure A.14**: Time-averaged streamlines and Reynolds stress correlation for stationary wing at angle-of-attack $\alpha = 12°$. Reynolds number based on mean aerodynamic chord is $Re_c = 59758$.

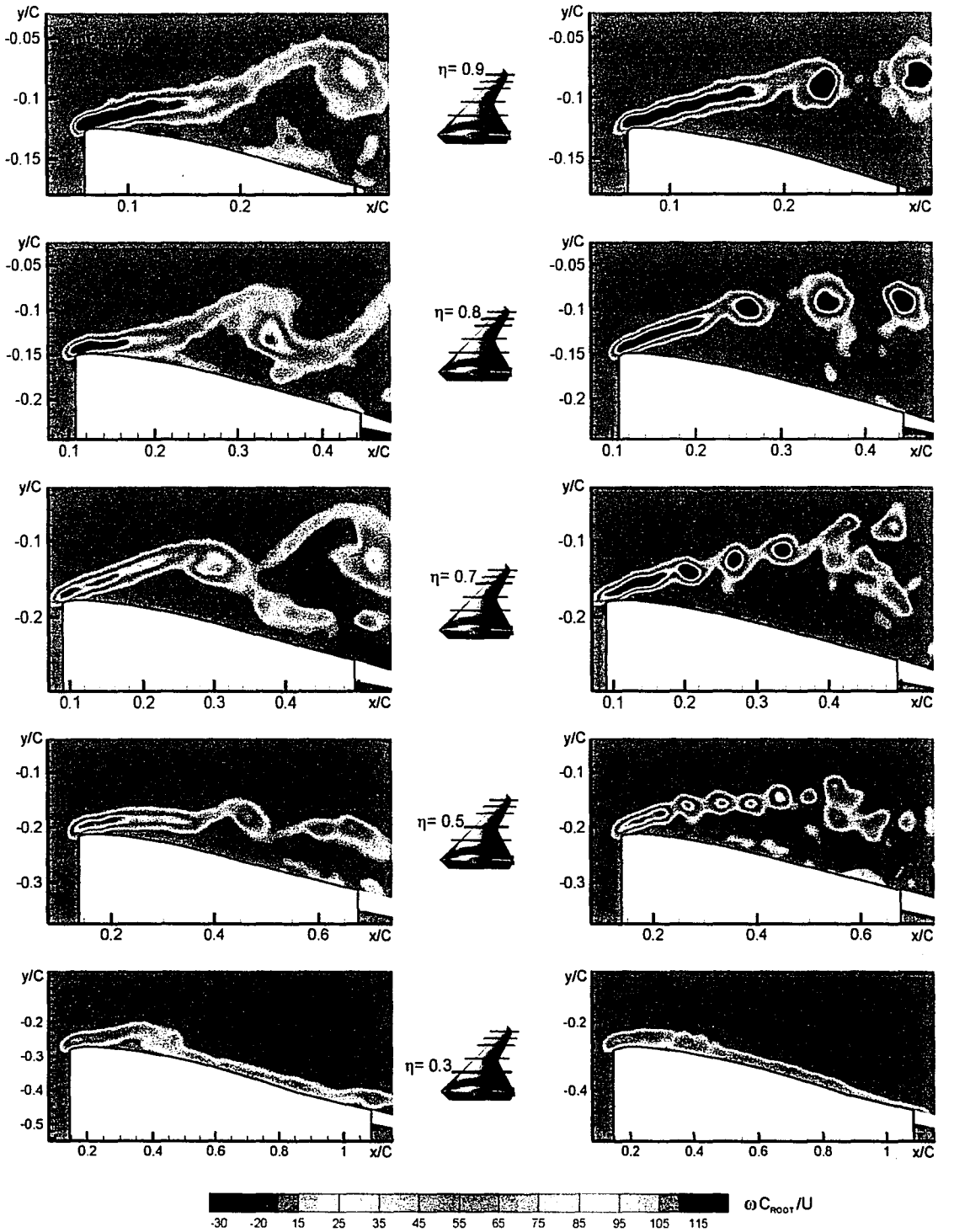


**Figure A.15**: Comparison of instantaneous patterns of vorticity at two values of Reynolds number based on mean aerodynamic chord, $Re_c = 5976$ (left column) and $Re_c = 17927$ (right column), for stationary wing at angle-of-attack $\alpha = 12°$.

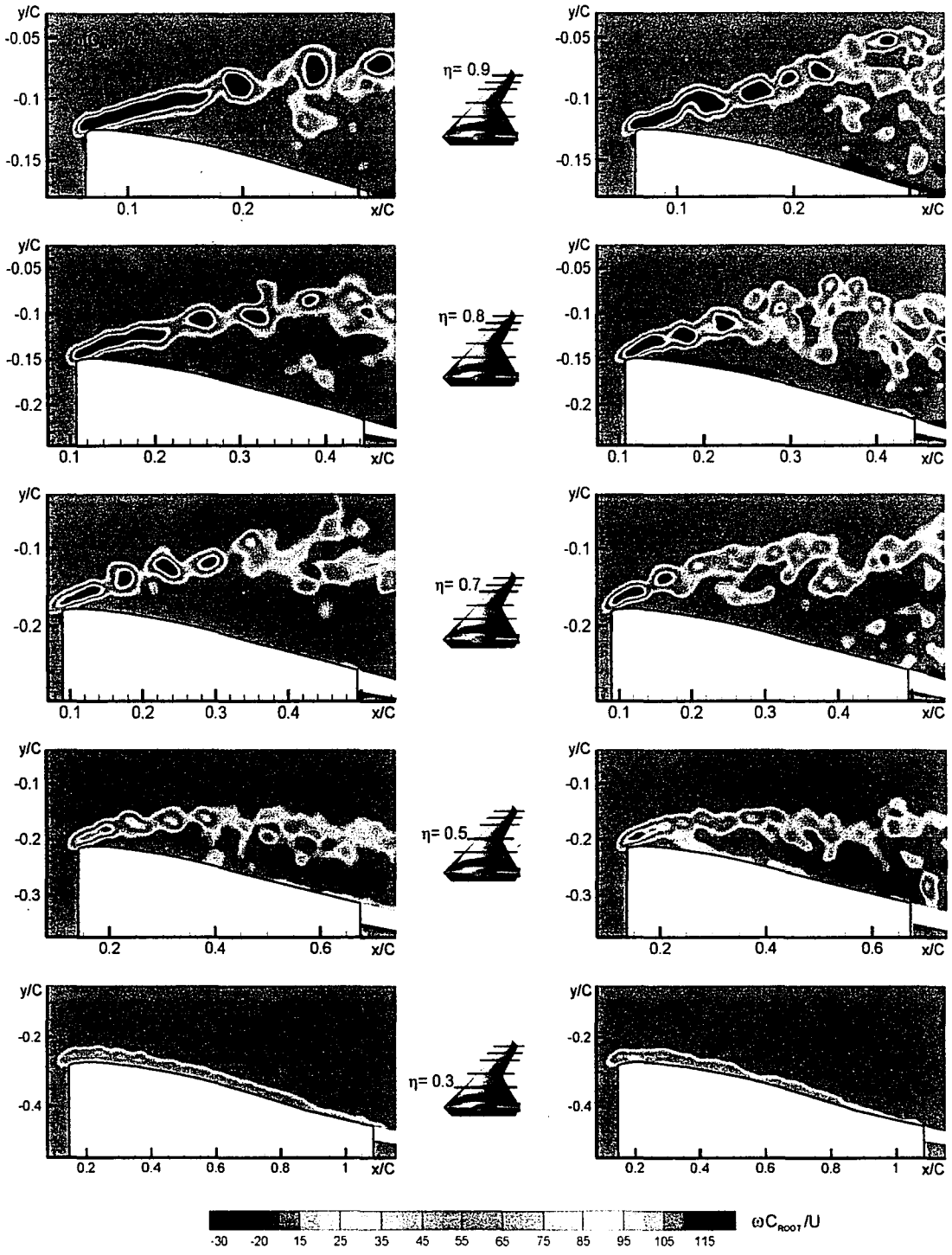


**Figure A.16**: Comparison of instantaneous patterns of vorticity at two values of Reynolds number based on mean aerodynamic chord. $Re_c$ = 29879 (left column) and $Re_c$ = 59758 (right column), for stationary wing at angle-of-attack $\alpha$ = 12°.

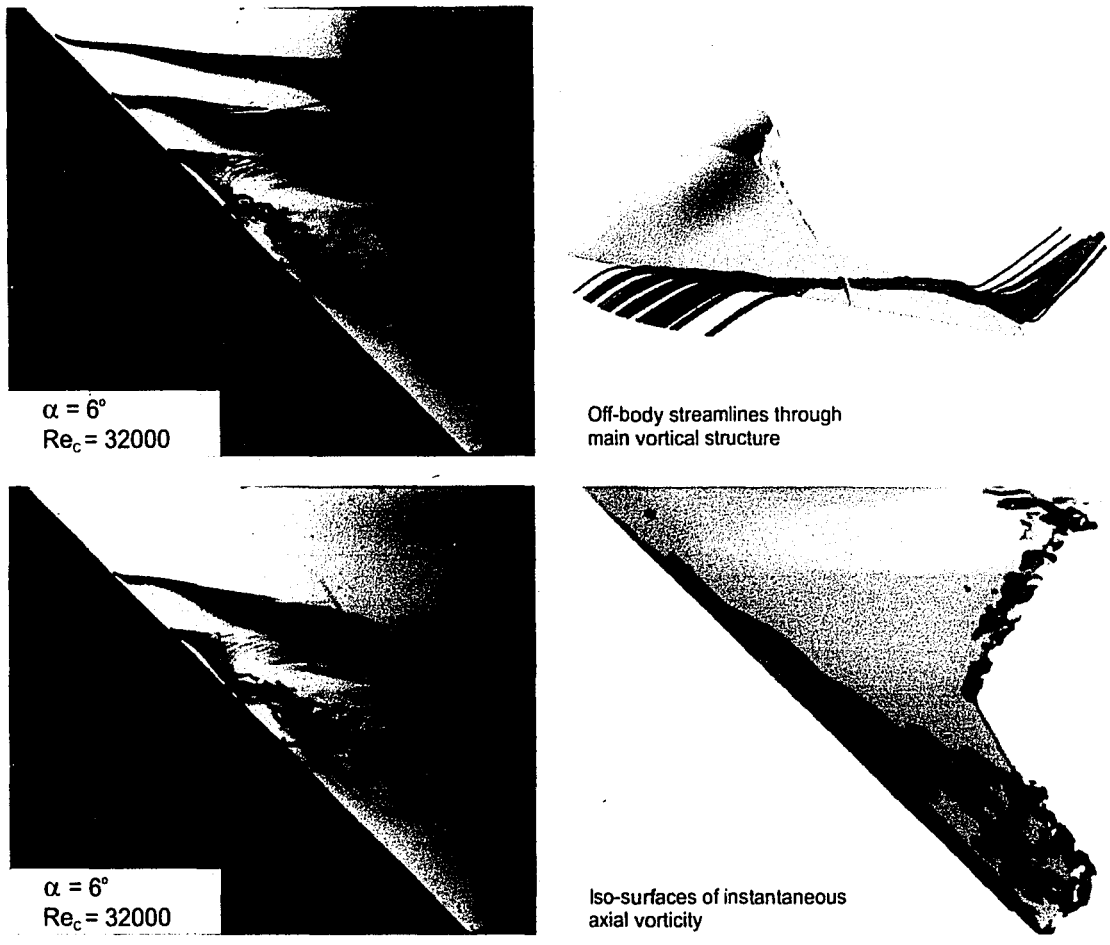


**Figure A.17**: Comparison of dye visualization versus computational results of vortical structure at angle-of-attack $\alpha = 6°$. Reynolds number based on mean aerodynamic chord is $Re_c = 32000$.

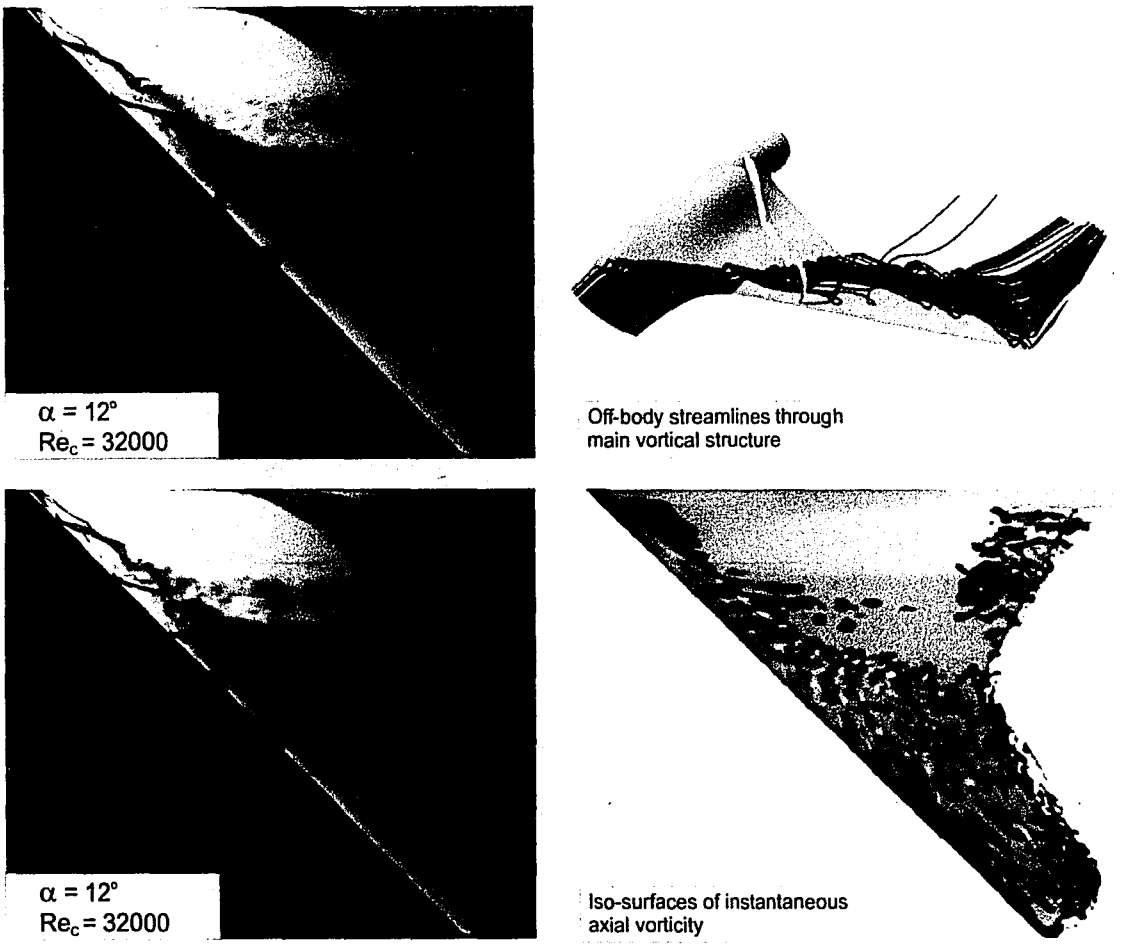


**Figure A.18**: Comparison of dye visualization versus computational results of vortical structure at angle-of-attack $\alpha = 12°$. Reynolds number based on mean aerodynamic chord is $Re_c = 32000$.

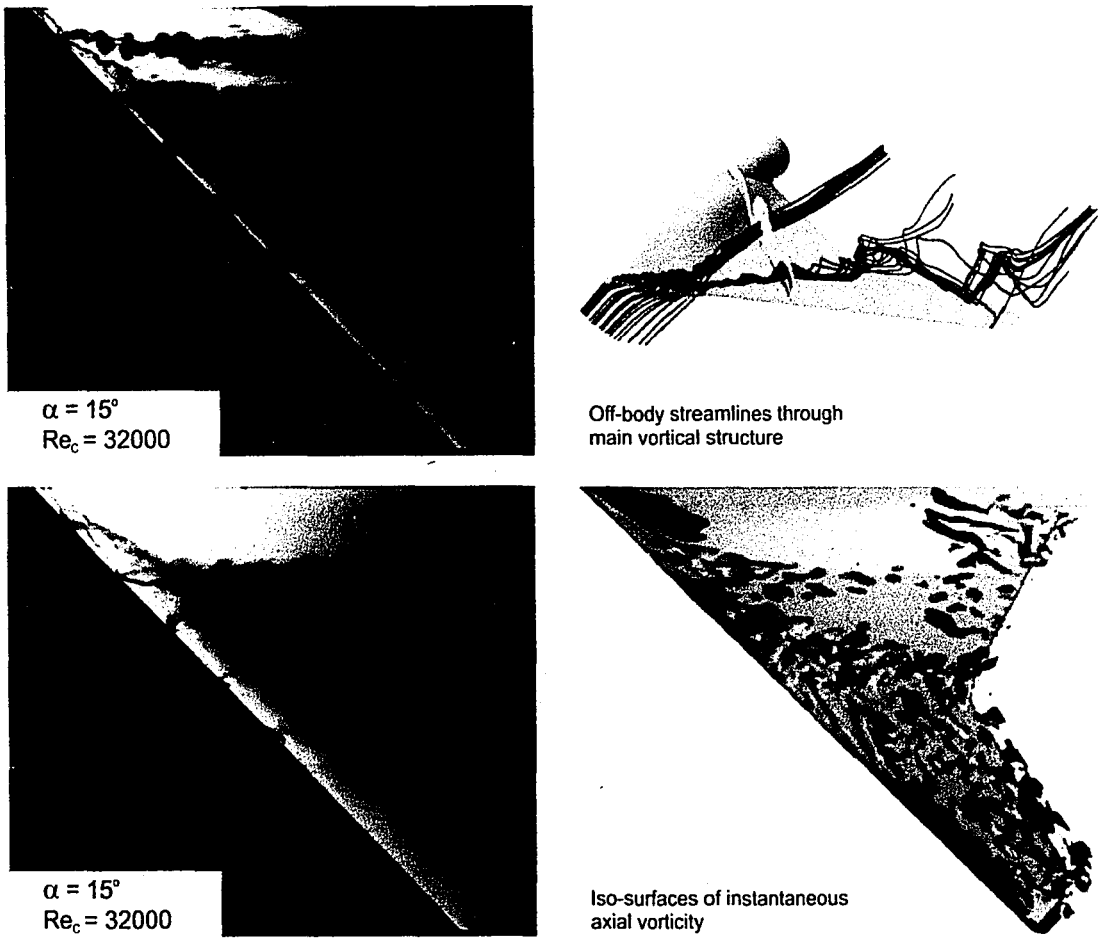


**Figure A.19**: Comparison of dye visualization versus computational results of vortical structure at angle-of-attack α = 15°. Reynolds number based on mean aerodynamic chord is $Re_c$ = 32000.

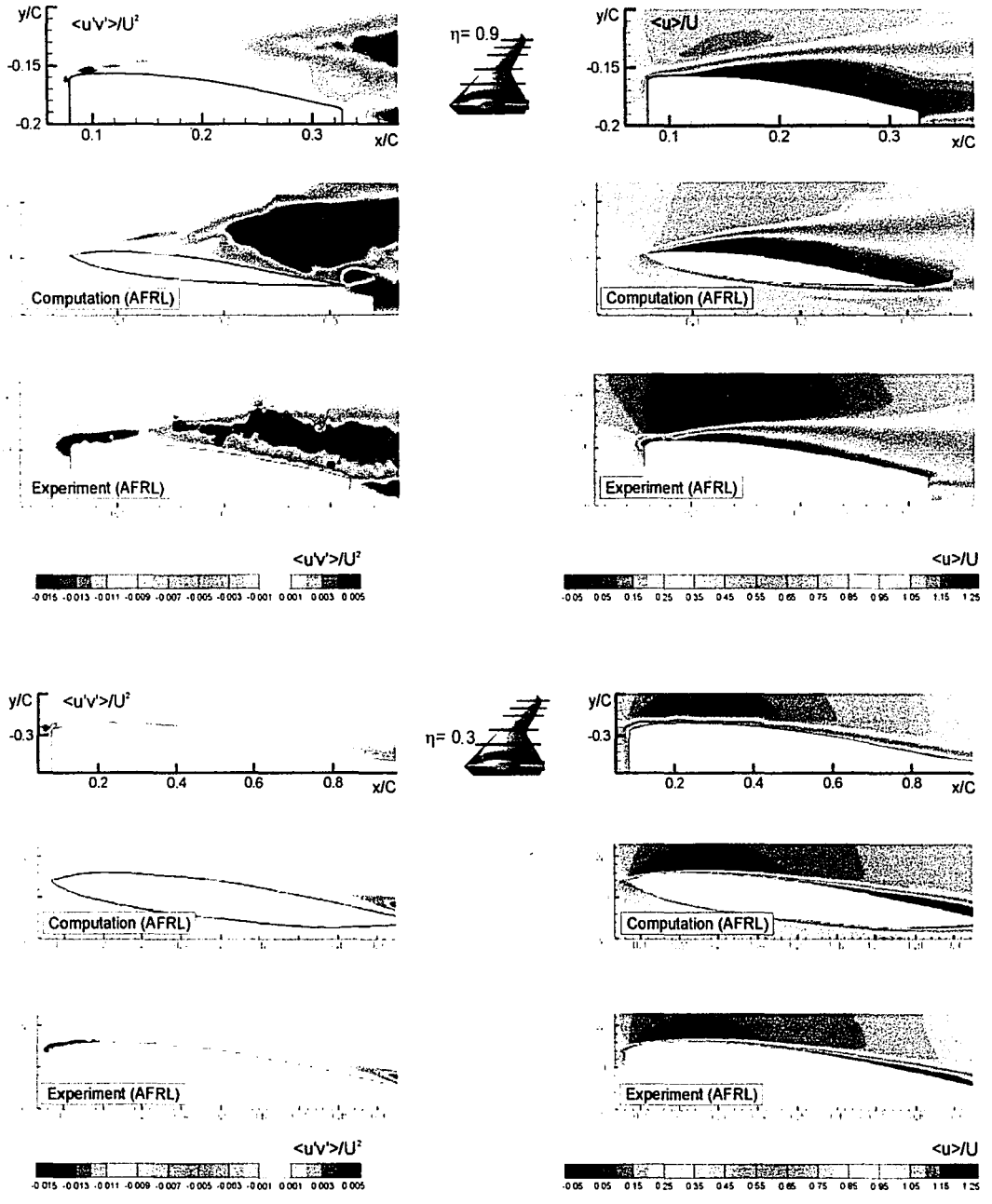


**Figure A.20**: Comparison of experimental and computational results of time-averaged patterns of vorticity and Reynolds stress at $\alpha = 6°$. Reynolds number based on mean aerodynamic chord is $Re_c = 32000$.

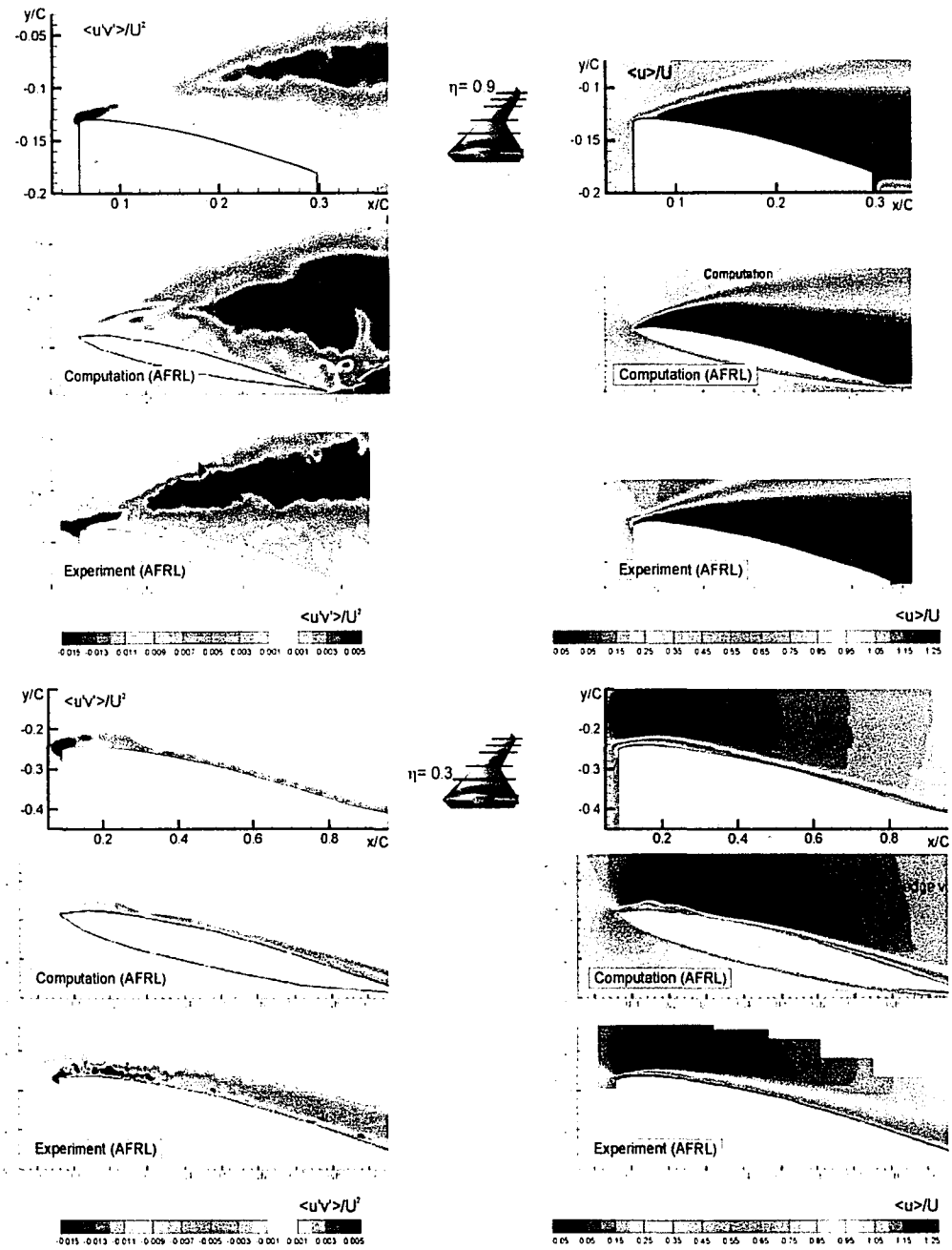


**Figure A.21**: Comparison of experimental and computational results of time-averaged patterns of vorticity and Reynolds stress at $\alpha = 12^{\circ}$. Reynolds number based on mean aerodynamic chord is $Re_c = 32000$.

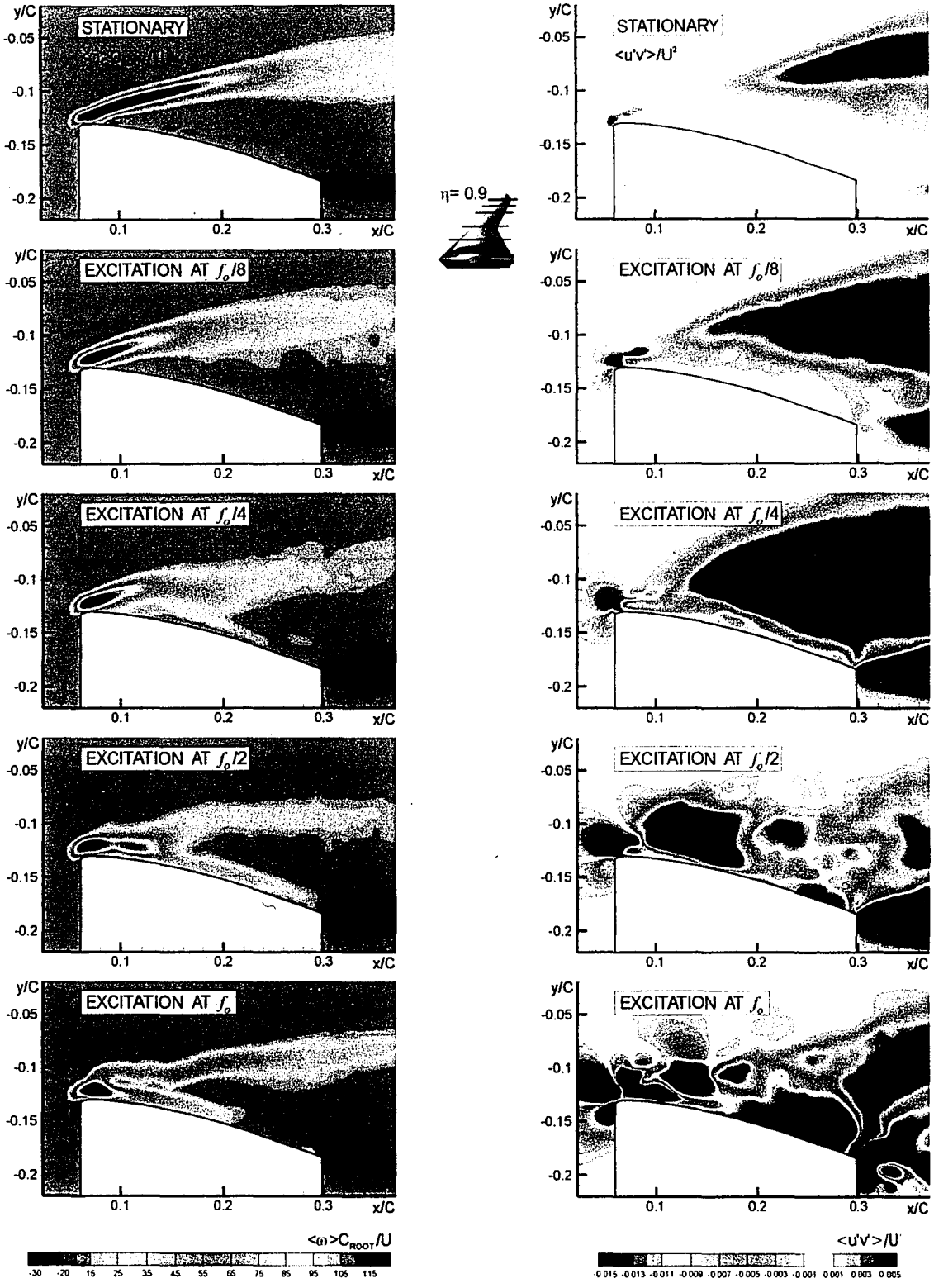


**Figure AA.1**: Time-averaged vorticity and Reynolds stress contours for case of wing subjected to perturbations of angle-of-attack according to $\alpha = \bar{\alpha} + \alpha_\epsilon \sin 2\pi f_\epsilon t$ ; $\bar{\alpha} = 12°$, $\alpha_\epsilon = 0.45°$ and $f_\epsilon = f_o/8, f_o/4, f_o/2$, and $f_o$ where $f_o$ is the inherent instability frequency of separating shear layer. Reynolds number based on mean aerodynamic chord is $Re_c = 17927$

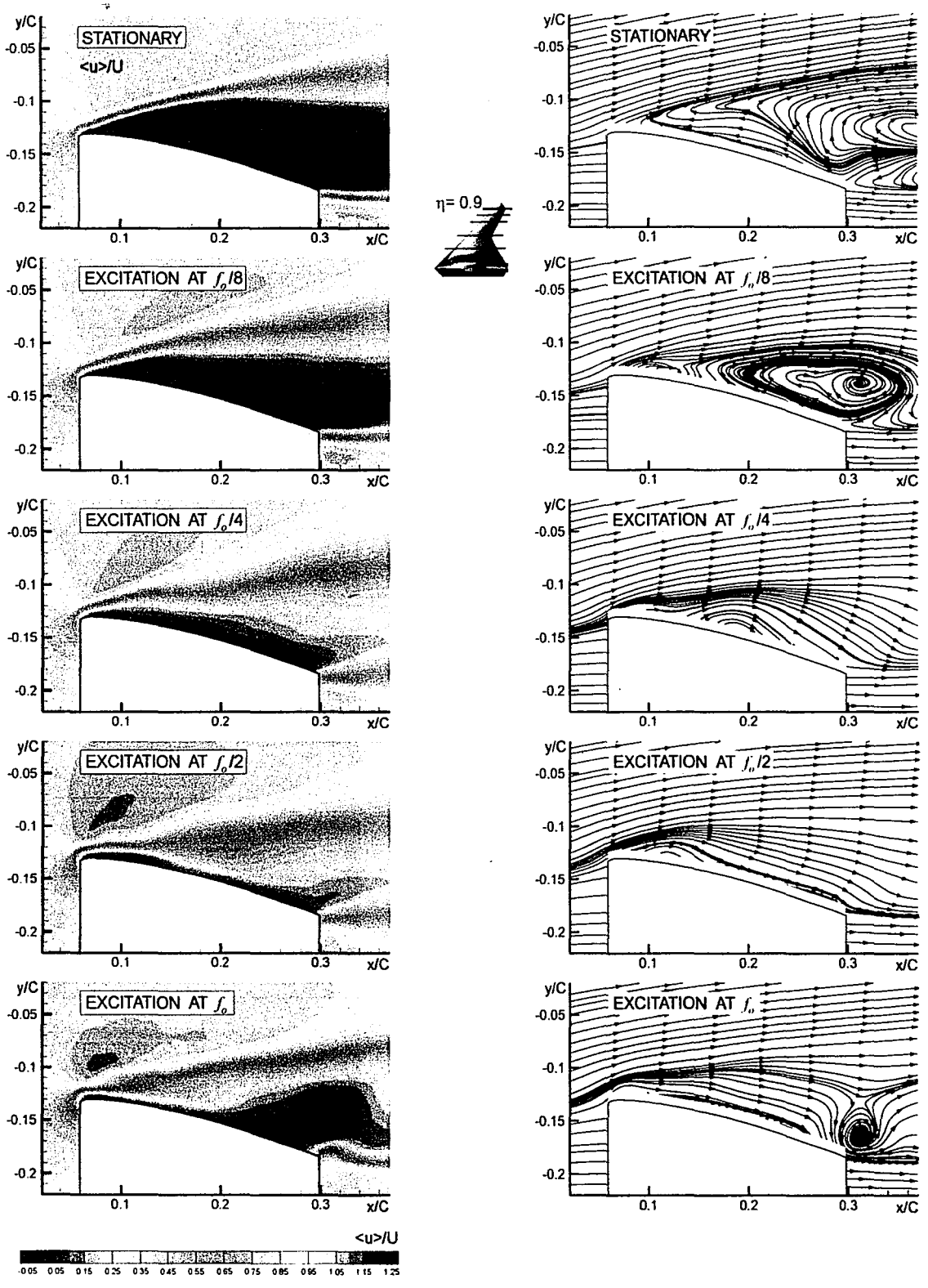
STATIONARY
<u>/U
EXCITATION AT $f_o$/8
EXCITATION AT $f_o$/4
EXCITATION AT $f_o$/2
EXCITATION AT $f_o$
η= 0.9
y/C
x/C
<u>/U</u>

**Figure AA.2**: Time-averaged streamwise velocity contours and streamlines for case of wing subjected to perturbations of angle-of-attack according to $\alpha = \bar{\alpha} + \alpha_e \sin 2\pi f_e t$ ; $\bar{\alpha} = 12°$, $\alpha_e = 0.45°$ and $f_e = f_o/8, f_o/4, f_o/2$, and $f_o$ where $f_o$ is the inherent instability frequency of separating shear layer. Reynolds number based on mean aerodynamic chord is $Re_c = 17927$

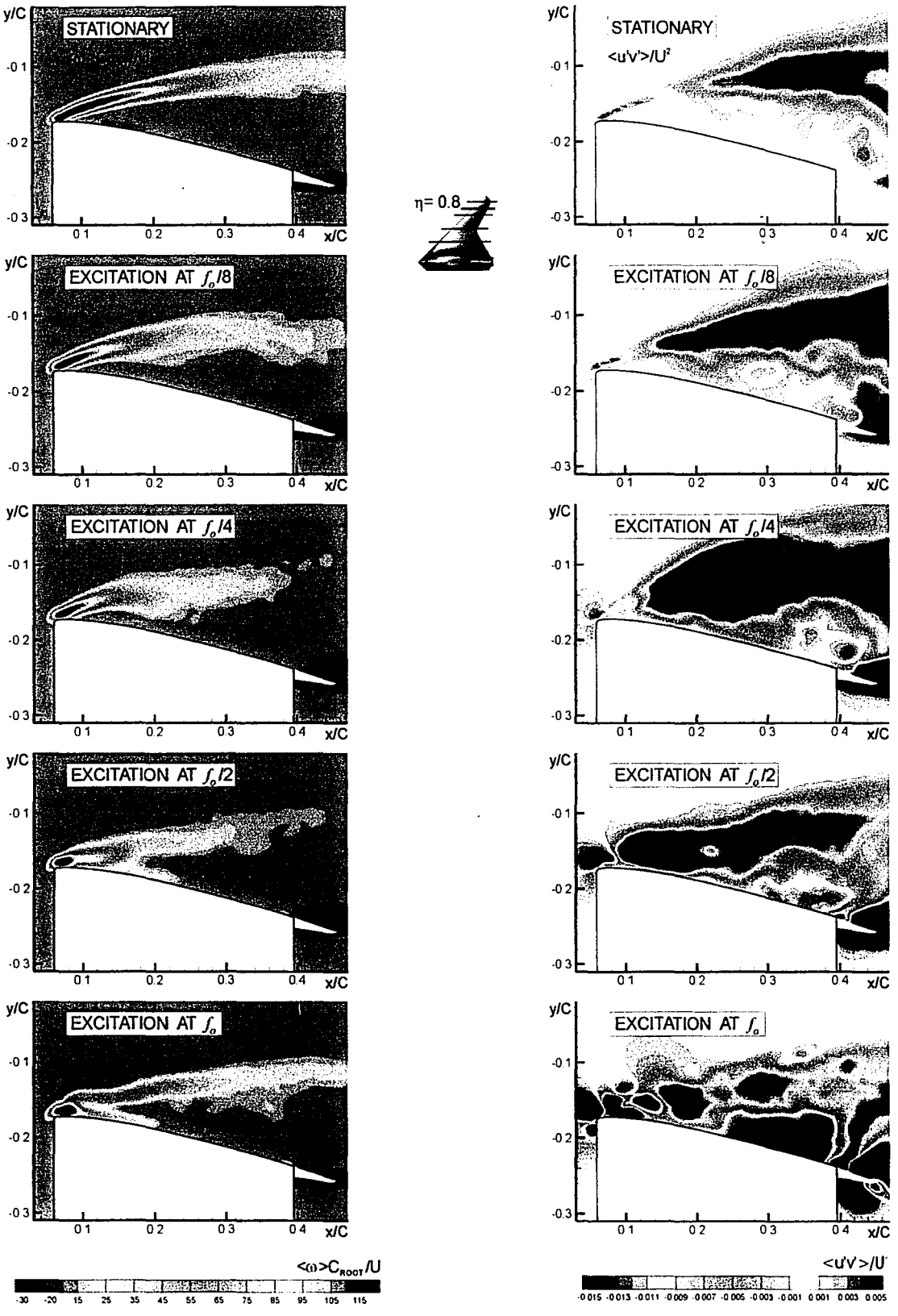


**Figure AA.3**: Time-averaged vorticity and Reynolds stress contours for case of wing subjected to perturbations of angle-of-attack according to $\alpha = \bar{\alpha} + \alpha_e \sin 2\pi f_e t$ ; $\bar{\alpha} = 12°$, $\alpha_e = 0.45°$ and $f_e = f_o/8, f_o/4, f_o/2$, and $f_o$ where $f_o$ is the inherent instability frequency of separating shear layer. Reynolds number based on mean aerodynamic chord is $Re_c = 17927$

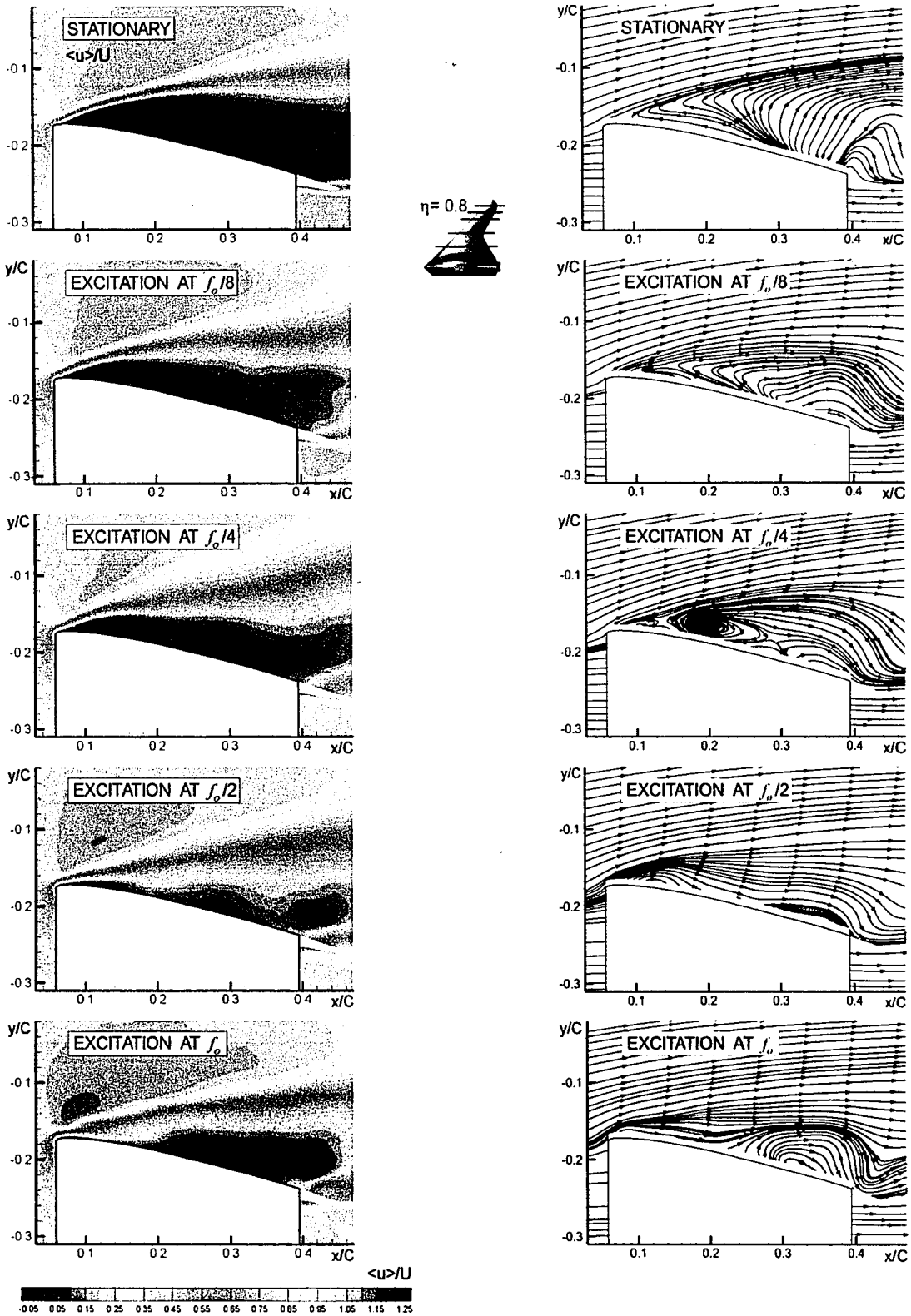


**Figure AA.4**: Time-averaged streamwise velocity contours and streamlines for case of wing subjected to perturbations of angle-of-attack according to $\alpha = \bar{\alpha} + \alpha_e \sin 2\pi f_e t$ ; $\bar{\alpha} = 12°$, $\alpha_e = 0.45°$ and $f_e = f_o/8, f_o/4, f_o/2$, and $f_o$ where $f_o$ is the inherent instability frequency of separating shear layer. Reynolds number based on mean aerodynamic chord is $Re_c = 17927$

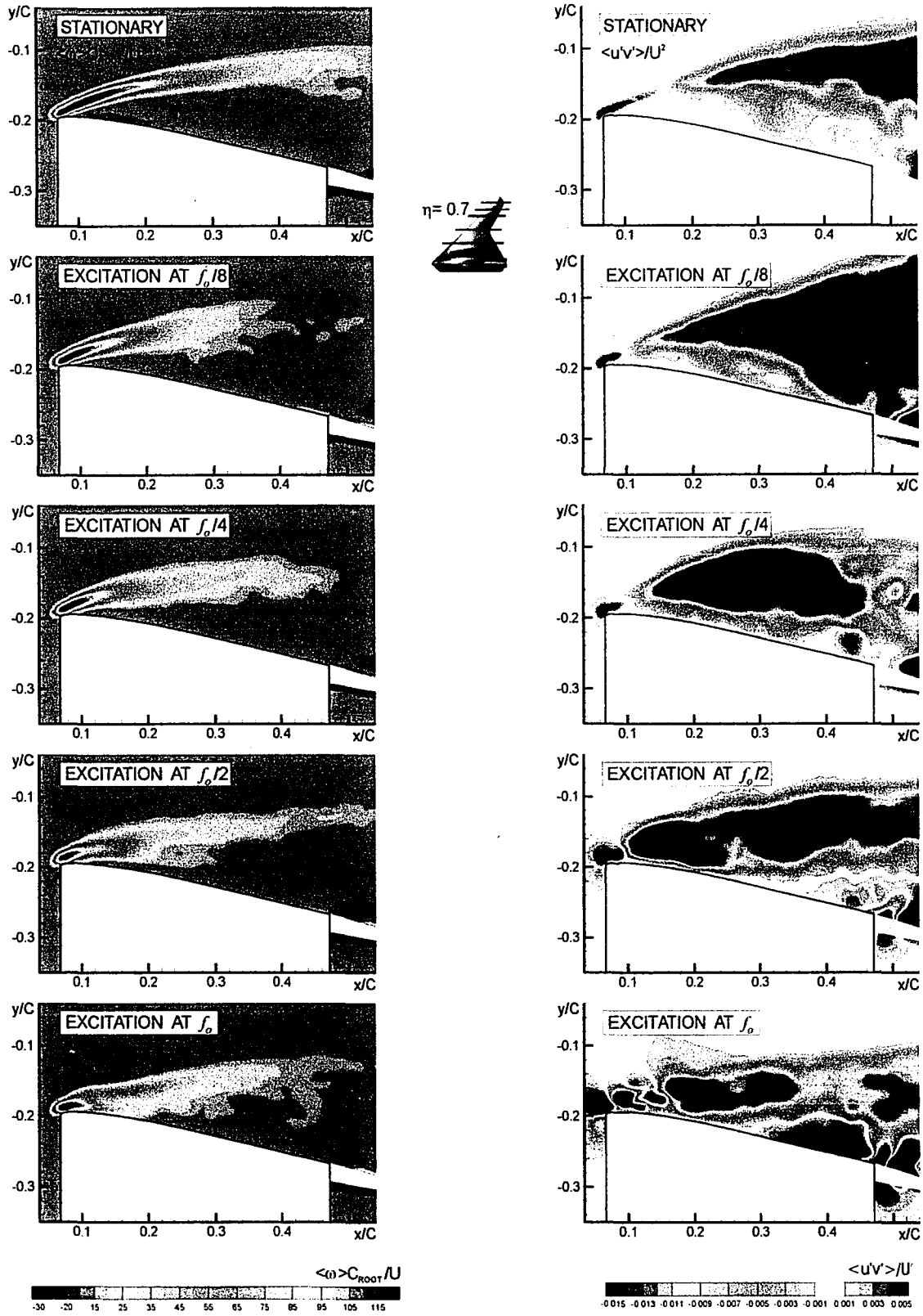


**Figure AA.5**: Time-averaged vorticity and Reynolds stress contours for case of wing subjected to perturbations of angle-of-attack according to $\alpha = \bar{\alpha} + \alpha_\epsilon \sin 2\pi f_\epsilon t$ ; $\bar{\alpha} = 12°$, $\alpha_\epsilon = 0.45°$ and $f_\epsilon = f_o/8, f_o/4, f_o/2$, and $f_o$ where $f_o$ is the inherent instability frequency of separating shear layer. Reynolds number based on mean aerodynamic chord is $Re_c = 17927$

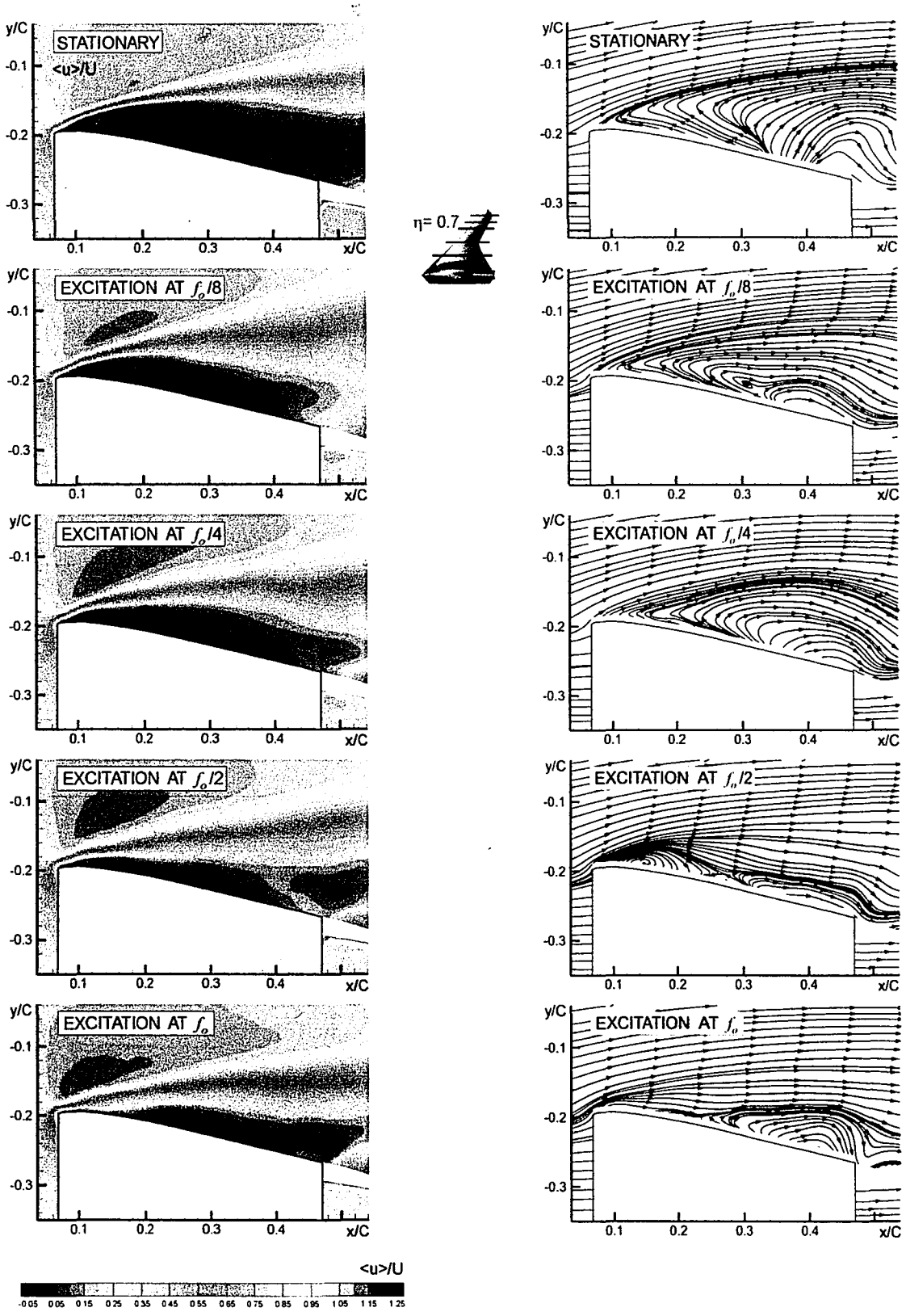


**Figure AA.6**: Time-averaged streamwise velocity contours and streamlines for case of wing subjected to perturbations of angle-of-attack according to $\alpha = \bar{\alpha} + \alpha_e \sin 2\pi f_e t$ ; $\bar{\alpha} = 12°$, $\alpha_e = 0.45°$ and $f_e = f_o/8, f_o/4, f_o/2$, and $f_o$ where $f_o$ is the inherent instability frequency of separating shear layer. Reynolds number based on mean aerodynamic chord is $Re_c = 17927$

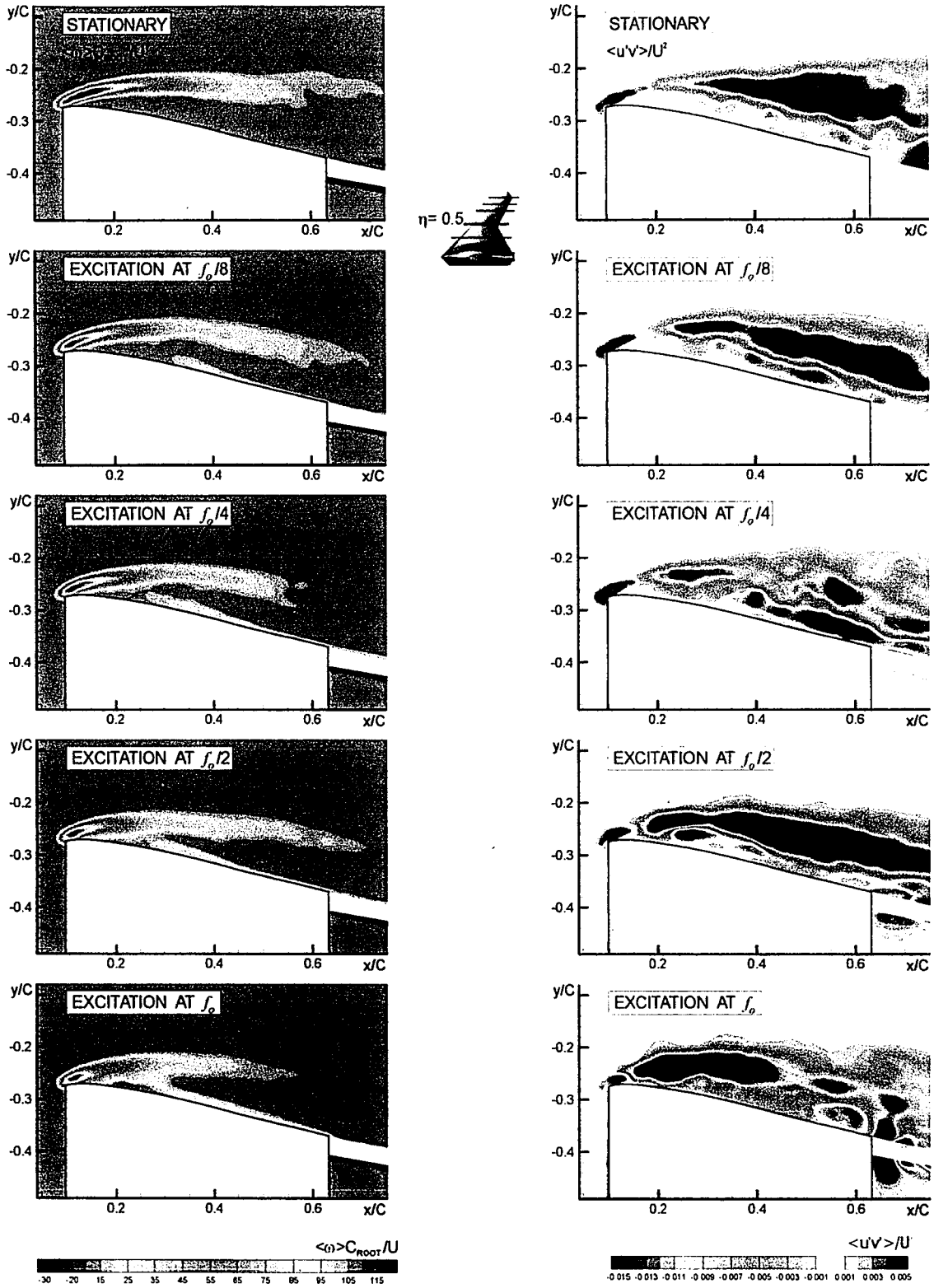


**Figure AA.7**: Time-averaged vorticity and Reynolds stress contours for case of wing subjected to perturbations of angle-of-attack according to $\alpha = \bar{\alpha} + \alpha_e \sin 2\pi f_e t$ ; $\bar{\alpha} = 12°$, $\alpha_e = 0.45°$ and $f_e = f_o/8, f_o/4, f_o/2$, and $f_o$ where $f_o$ is the inherent instability frequency of separating shear layer. Reynolds number based on mean aerodynamic chord is $Re_c = 17927$

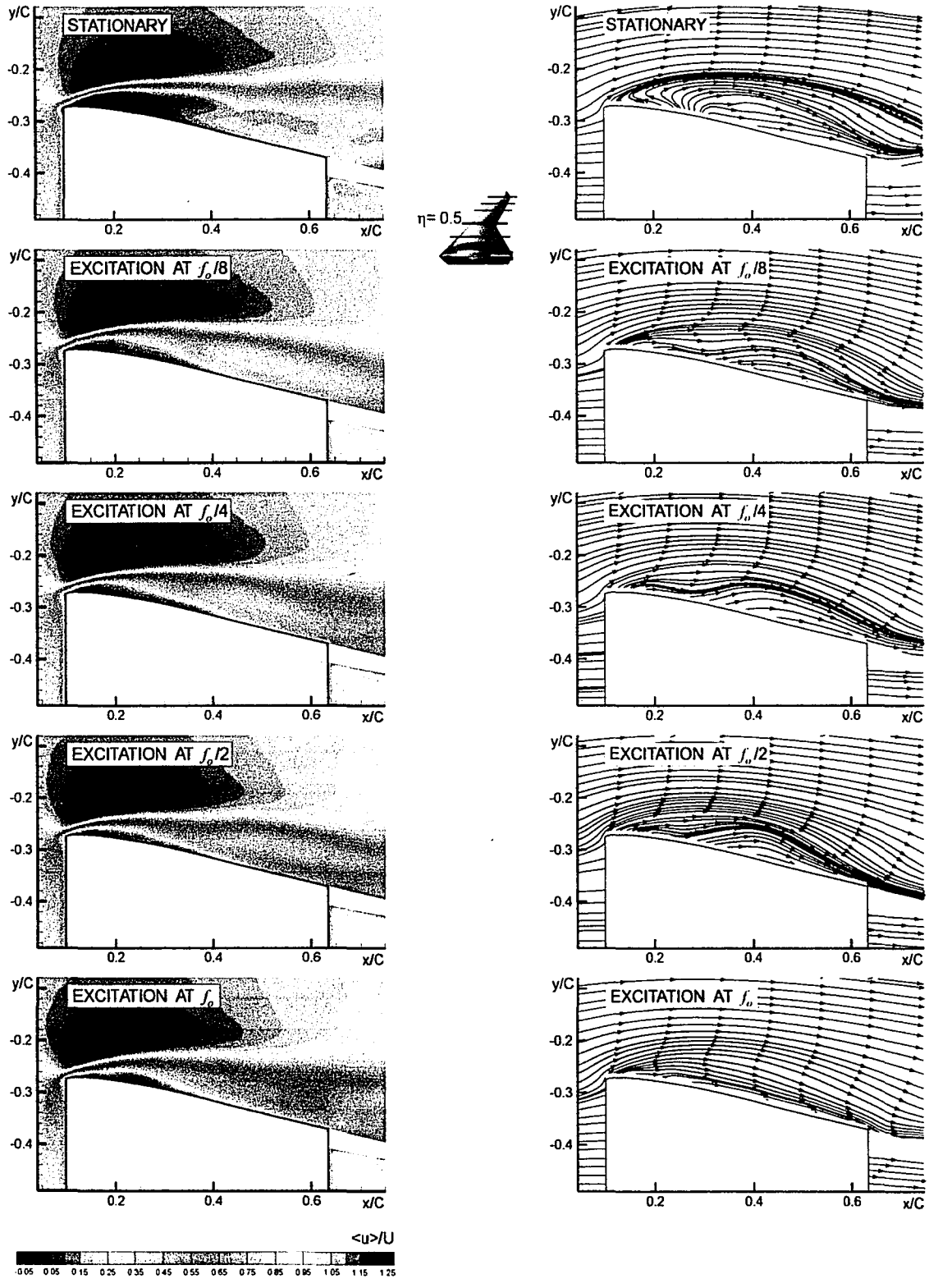


**Figure AA.8**: Time-averaged streamwise velocity contours and streamlines for case of wing subjected to perturbations of angle-of-attack according to $\alpha = \bar{\alpha} + \alpha_\epsilon \sin 2\pi f_\epsilon t$ ; $\bar{\alpha} = 12°$, $\alpha_\epsilon = 0.45°$ and $f_\epsilon = f_o/8, f_o/4, f_o/2$, and $f_o$ where $f_o$ is the inherent instability frequency of separating shear layer. Reynolds number based on mean aerodynamic chord is $Re_c = 17927$

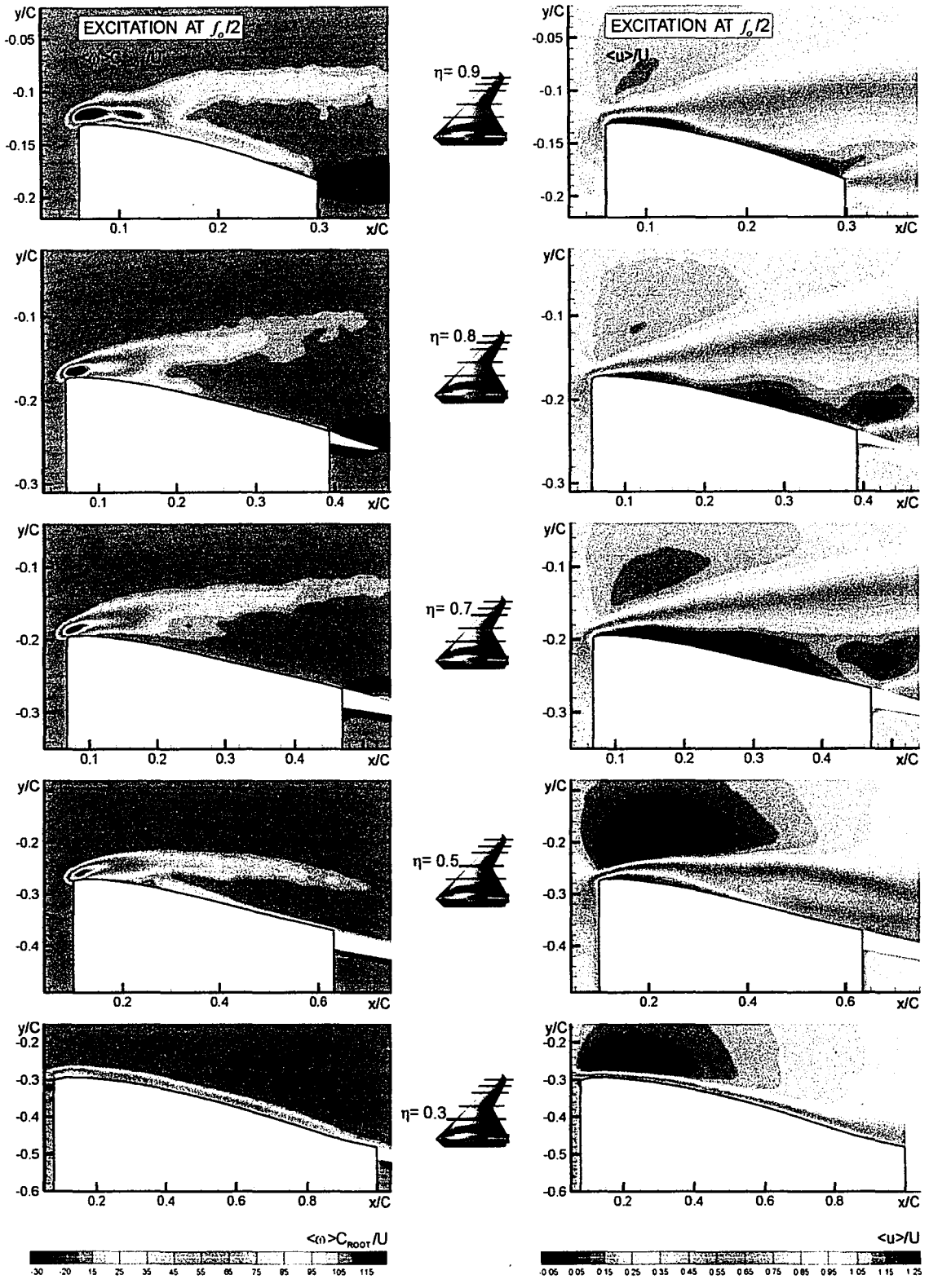


**Figure AA.9**: Time-averaged vorticity and streamwise velocity contours for case of wing subjected to perturbations of angle-of-attack according to $\alpha = \bar{\alpha} + \alpha_e \sin 2\pi f_e t$ ; $\bar{\alpha} = 12°$, $\alpha_e = 0.45°$ and $f_e = f_o/2$, where $f_o$ is the inherent instability frequency of separating shear layer. Reynolds number based on mean aerodynamic chord is $Re_c = 17927$

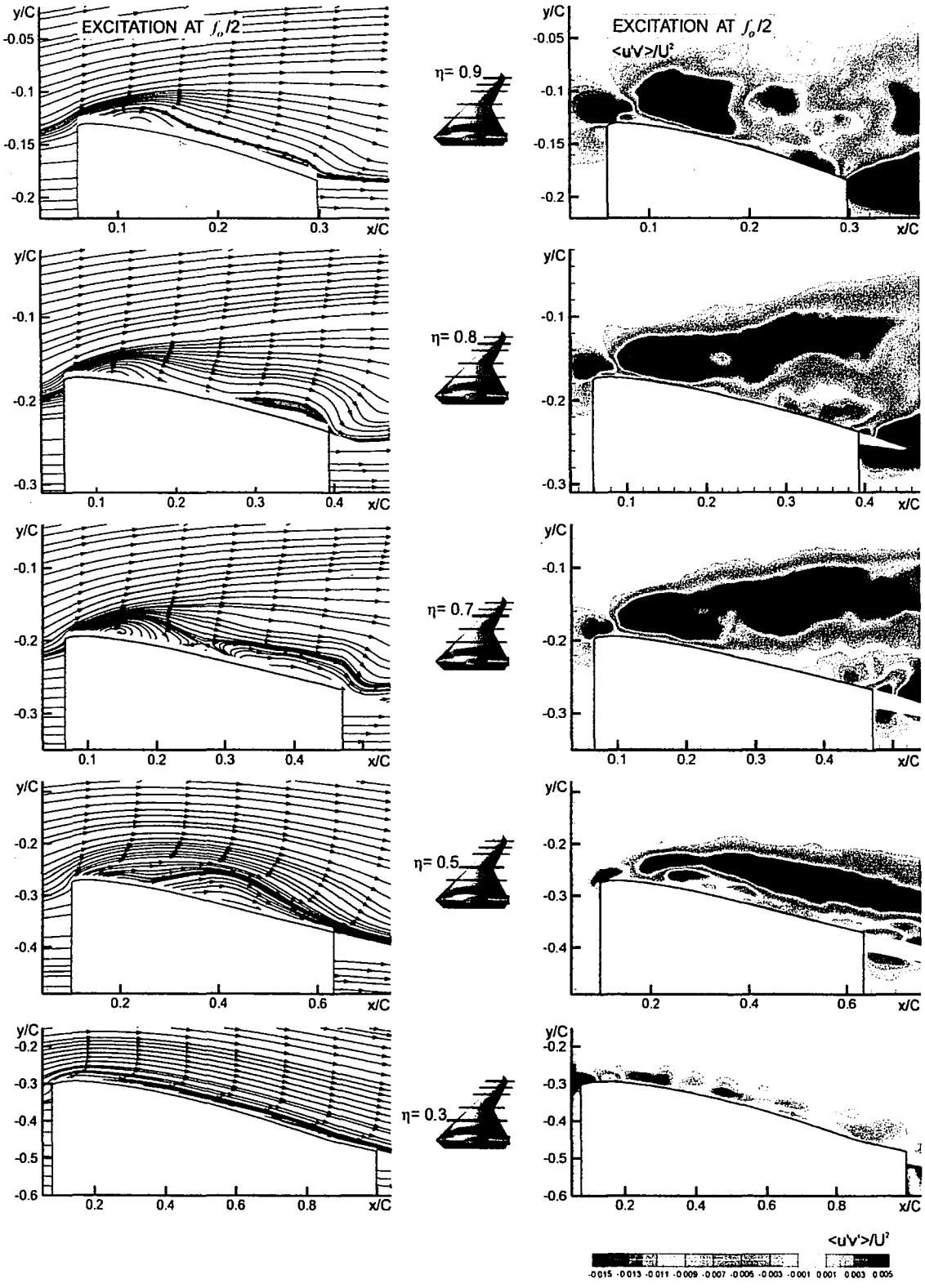


**Figure AA.10**: Time-averaged streamlines and Reynolds stress contours for case of wing subjected to perturbations of angle-of-attack according to $\alpha = \bar{\alpha} + \alpha_e \sin 2\pi f_e t$ ; $\bar{\alpha} = 12°$, $\alpha_e = 0.45°$ and $f_e = f_o/2$, where $f_o$ is the inherent instability frequency of separating shear layer. Reynolds number based on mean aerodynamic chord is $Re_c = 17927$

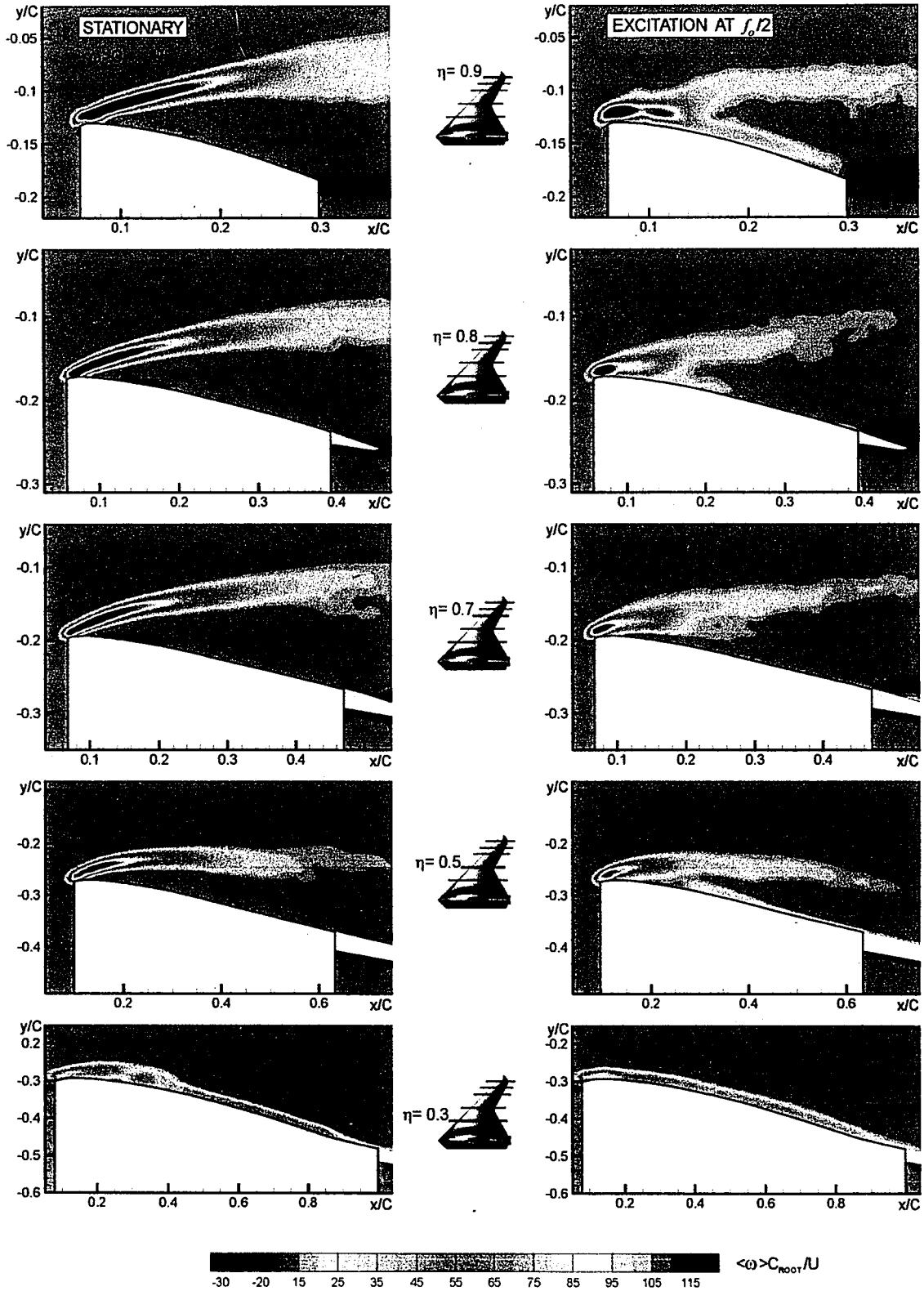


**Figure AA.11**: Time-averaged vorticity contours for case of wing subjected to perturbations of angle-of-attack according to $\alpha = \bar{\alpha} + \alpha_e \sin 2\pi f_e t$ ; $\bar{\alpha} = 12°$, $\alpha_e = 0.45°$ and $f_e = f_o/2$, where $f_o$ is the inherent instability frequency of separating shear layer. Reynolds number based on mean aerodynamic chord is $Re_c = 17927$

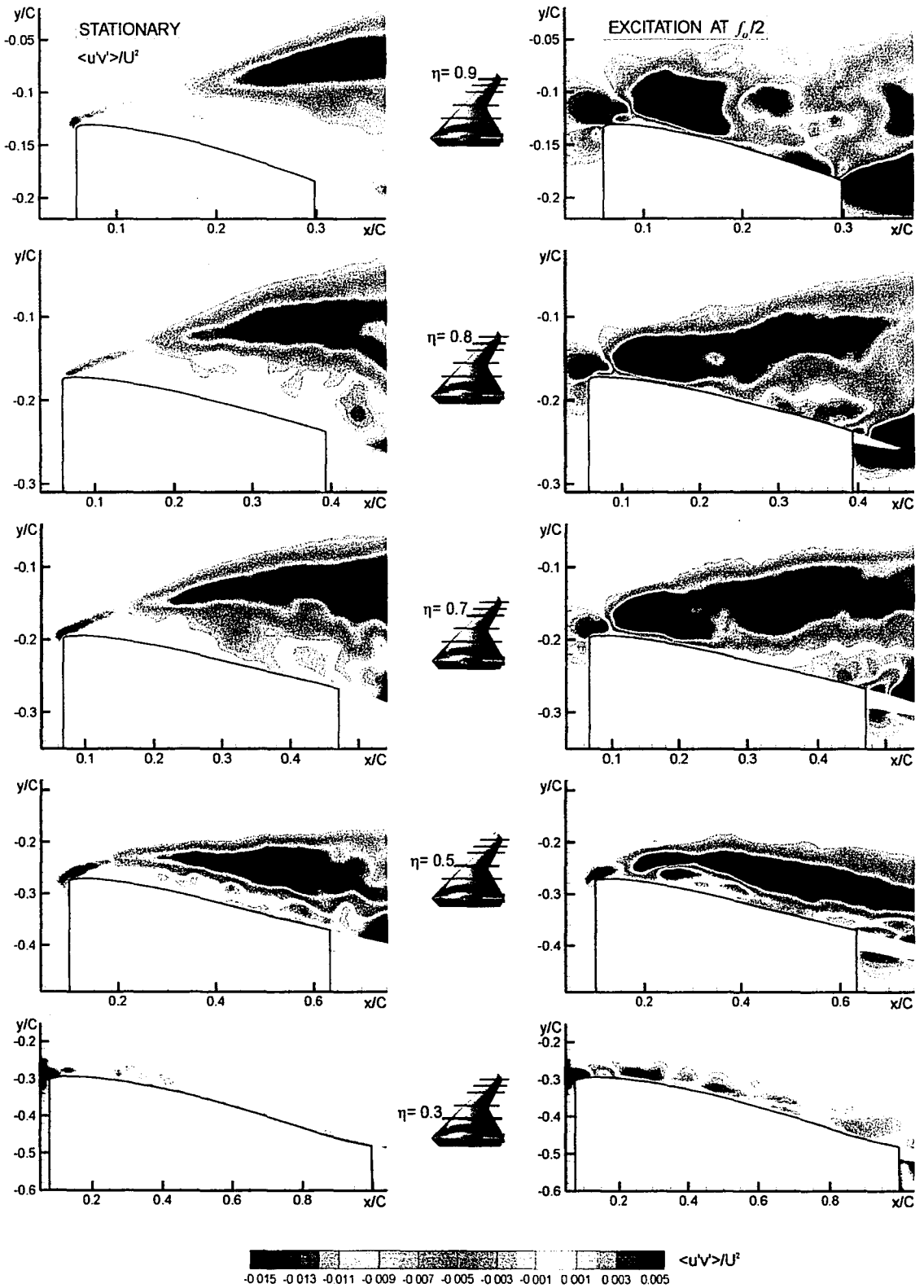


**Figure AA.12**: Time-averaged Reynolds stress contours for case of wing subjected to perturbations of angle-of-attack according to $\alpha = \bar{\alpha} + \alpha_e \sin 2\pi f_e t$ ; $\bar{\alpha} = 12°$, $\alpha_e = 0.45°$ and $f_e = f_o/2$, where $f_o$ is the inherent instability frequency of separating shear layer. Reynolds number based on mean aerodynamic chord is $Re_c = 17927$

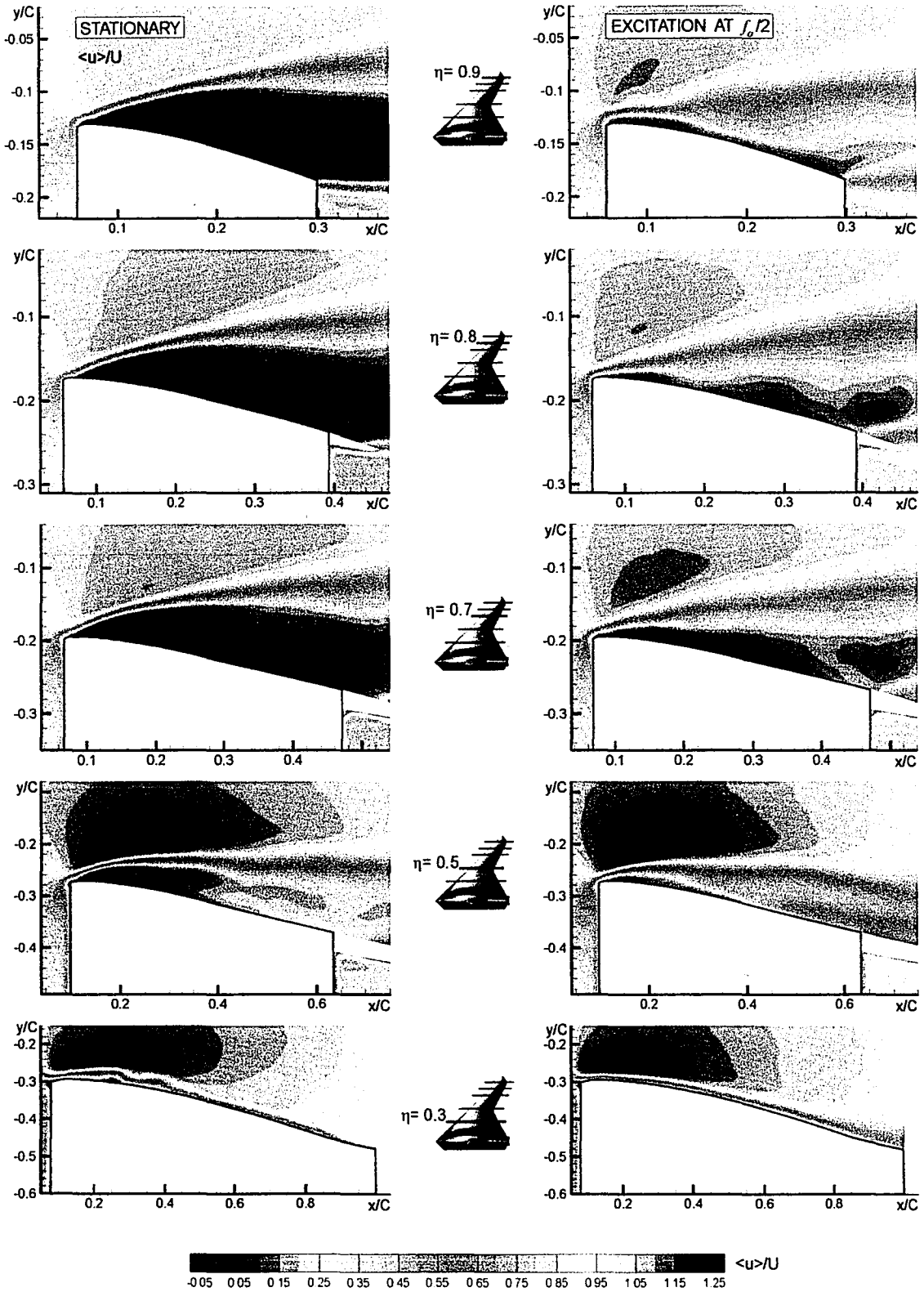


**Figure AA.13**: Time-averaged streamwise velocity contours for case of wing subjected to perturbations of angle-of-attack according to $\alpha = \bar{\alpha} + \alpha_e \sin 2\pi f_e t$ ; $\bar{\alpha} = 12°$, $\alpha_e = 0.45°$ and $f_e = f_o/2$, where $f_o$ is the inherent instability frequency of separating shear layer. Reynolds number based on mean aerodynamic chord is $Re_c = 17927$

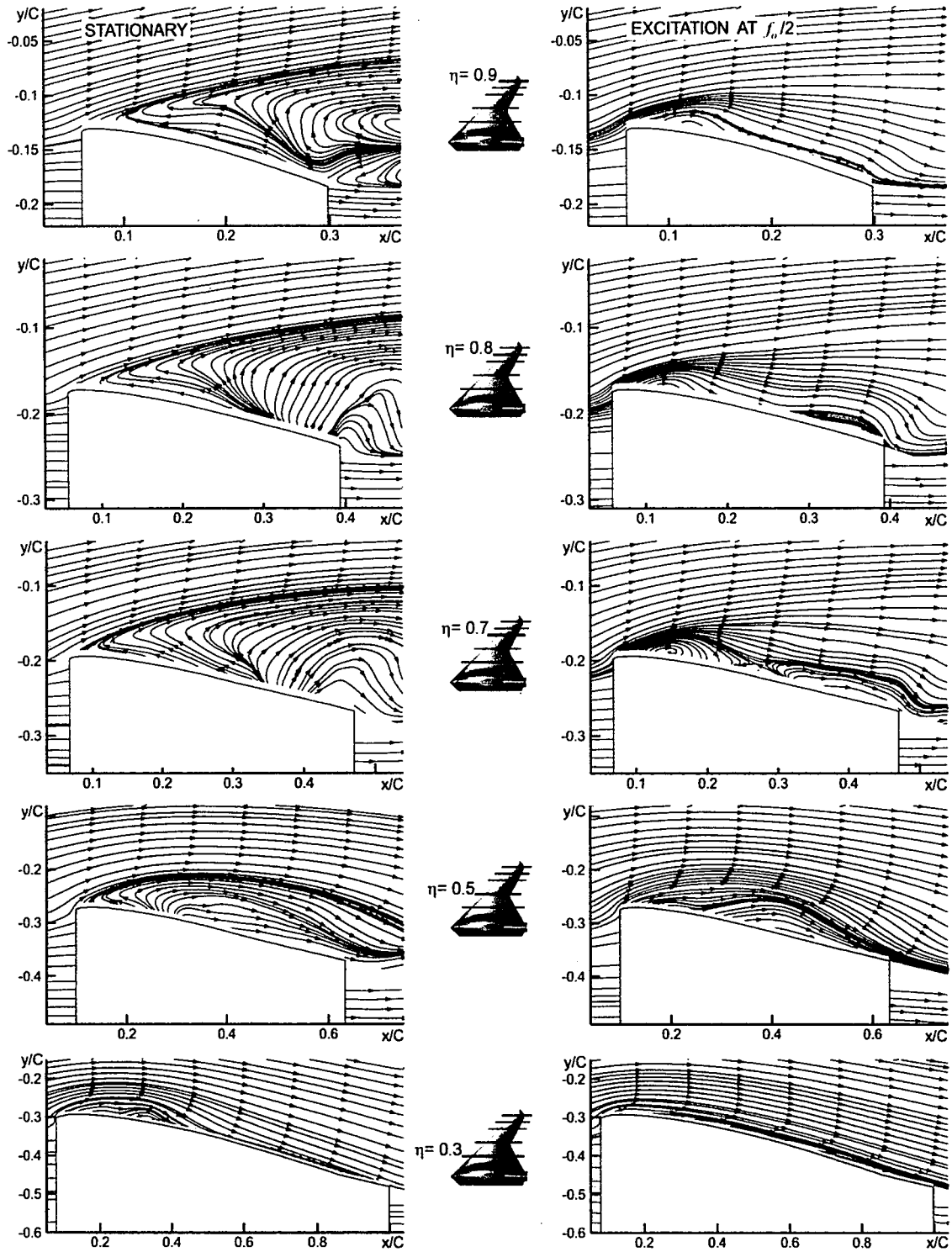


**Figure AA.14**: Time-averaged streamlines for case of wing subjected to perturbations of angle-of-attack according to $\alpha = \bar{\alpha} + \alpha_e \sin 2\pi f_e t$ ; $\bar{\alpha} = 12°$, $\alpha_e = 0.45°$ and $f_e = f_o/2$, where $f_o$ is the inherent instability frequency of separating shear layer. Reynolds number based on mean aerodynamic chord is $Re_c = 17927$

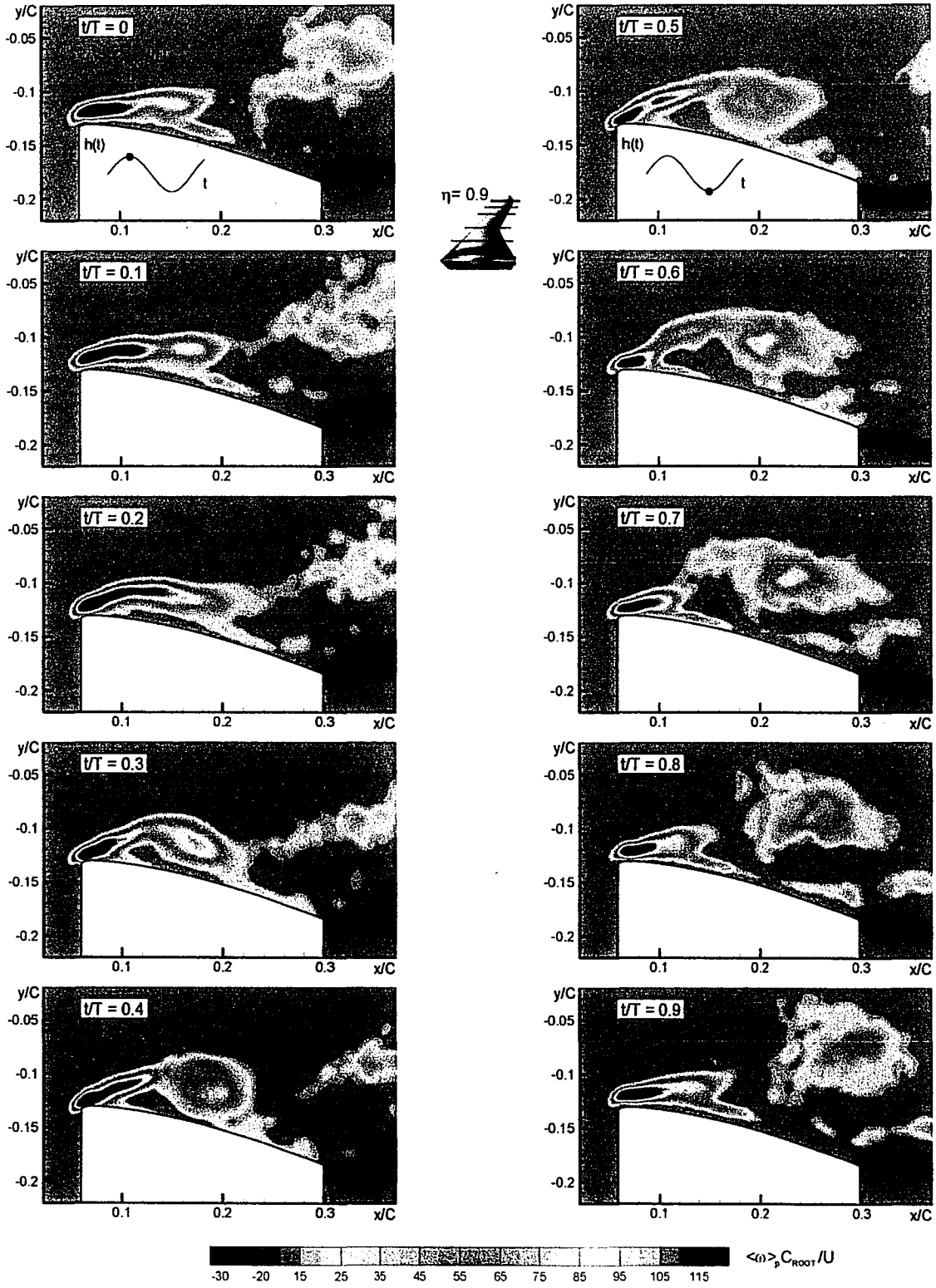


**Figure AA.15**: Phase-averaged vorticity contours for case of wing subjected to perturbations of angle-of-attack according to $\alpha = \bar{\alpha} + \alpha_e \sin 2\pi f_e t$ ; $\bar{\alpha} = 12°$, $\alpha_e = 0.45°$ and $f_e = f_o/4$, where $f_o$ is the inherent instability frequency of separating shear layer. Reynolds number based on mean aerodynamic chord is $Re_c = 17927$

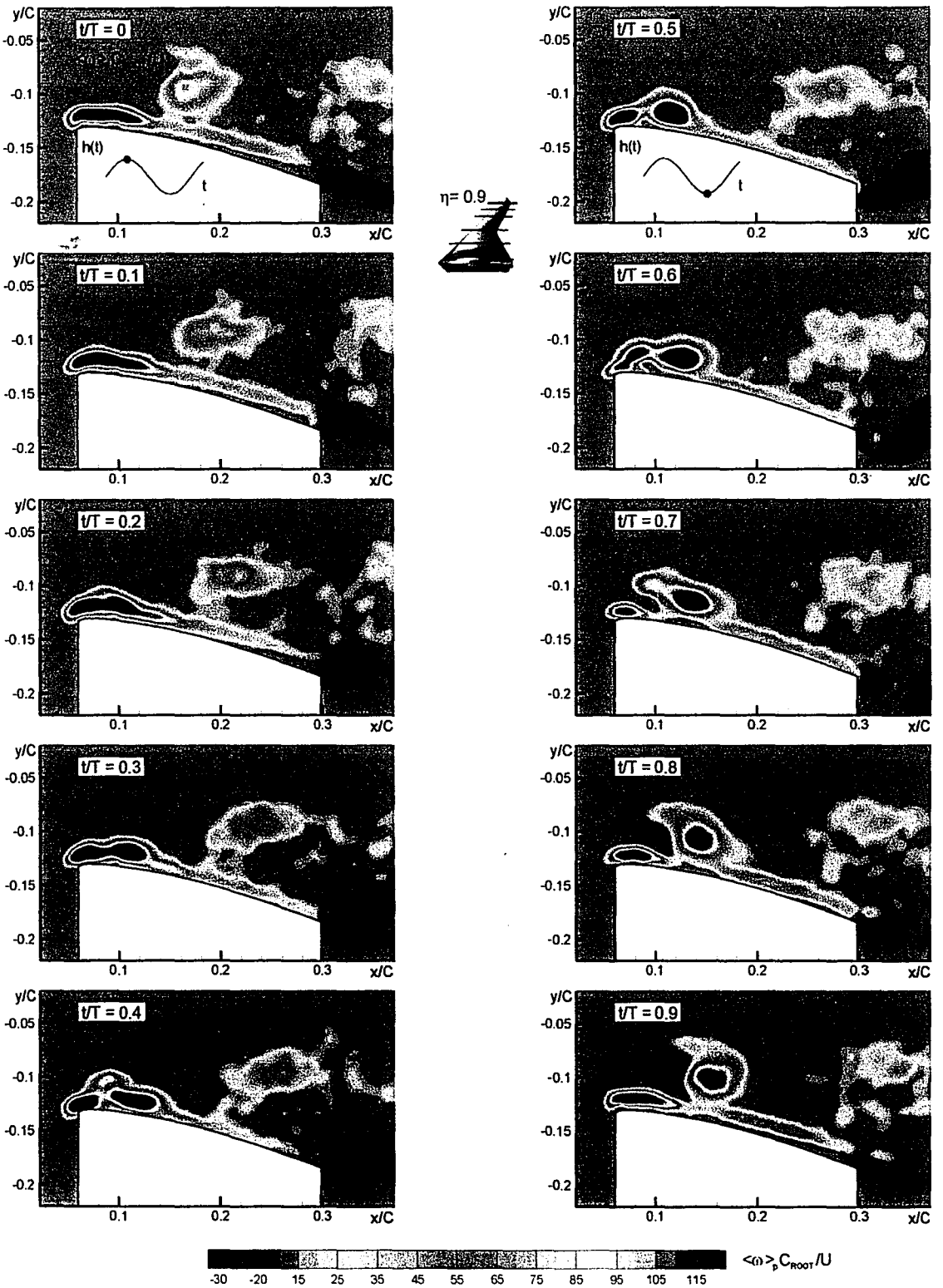


**Figure AA.16**: Phase-averaged vorticity contours for case of wing subjected to perturbations of angle-of-attack according to $\alpha = \bar{\alpha} + \alpha_e \sin 2\pi f_e t$ ; $\bar{\alpha} = 12°$, $\alpha_e = 0.45°$ and $f_e = f_o/2$, where $f_o$ is the inherent instability frequency of separating shear layer. Reynolds number based on mean aerodynamic chord is $Re_c = 17927$

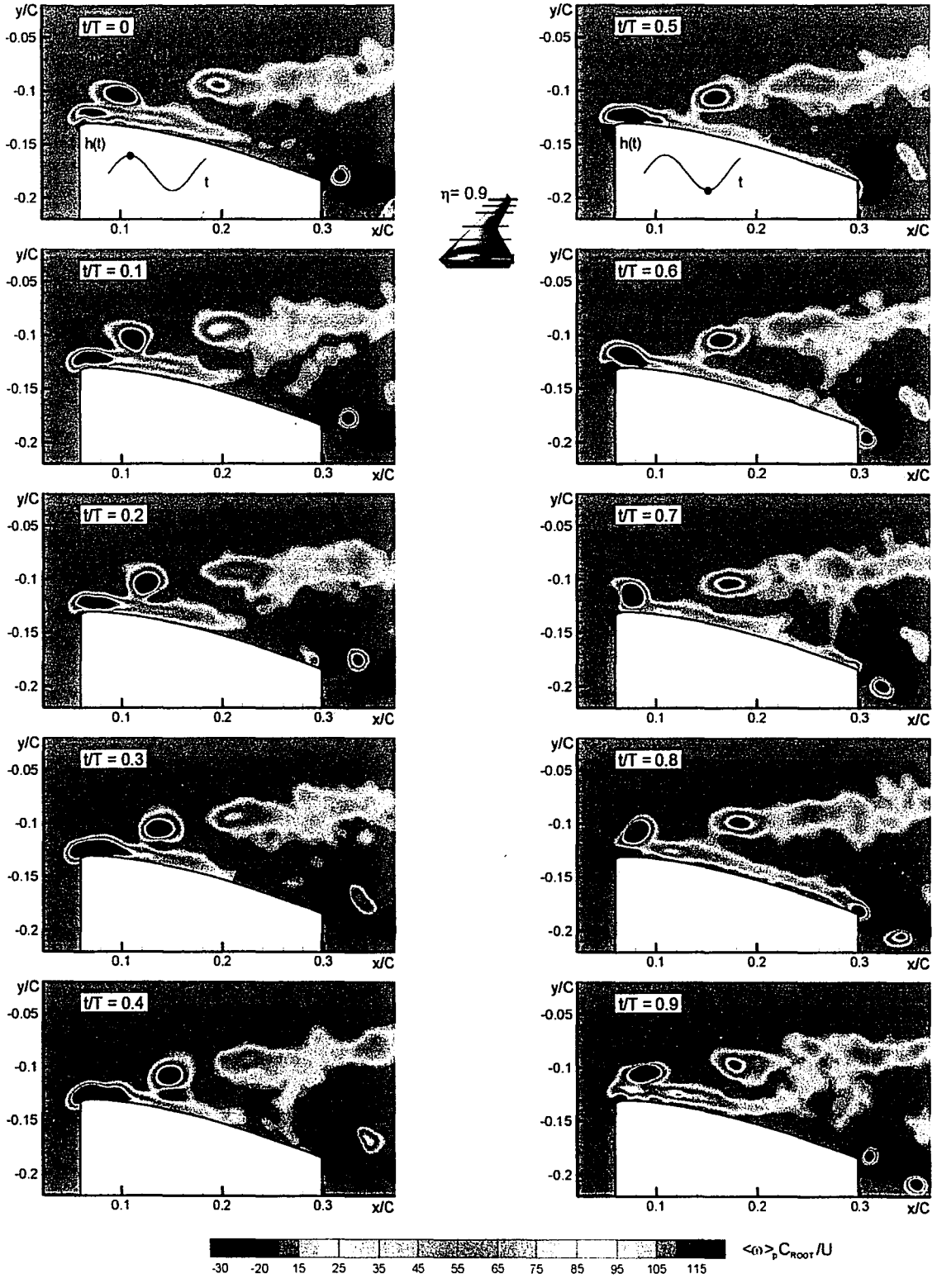


**Figure AA.17**: Phase-averaged vorticity contours for case of wing subjected to perturbations of angle-of-attack according to $\alpha = \bar{\alpha} + \alpha_e \sin 2\pi f_e t$ ; $\bar{\alpha} = 12°$, $\alpha_e = 0.45°$ and $f_e = f_o$, where $f_o$ is the inherent instability frequency of separating shear layer. Reynolds number based on mean aerodynamic chord is $Re_c = 17927$

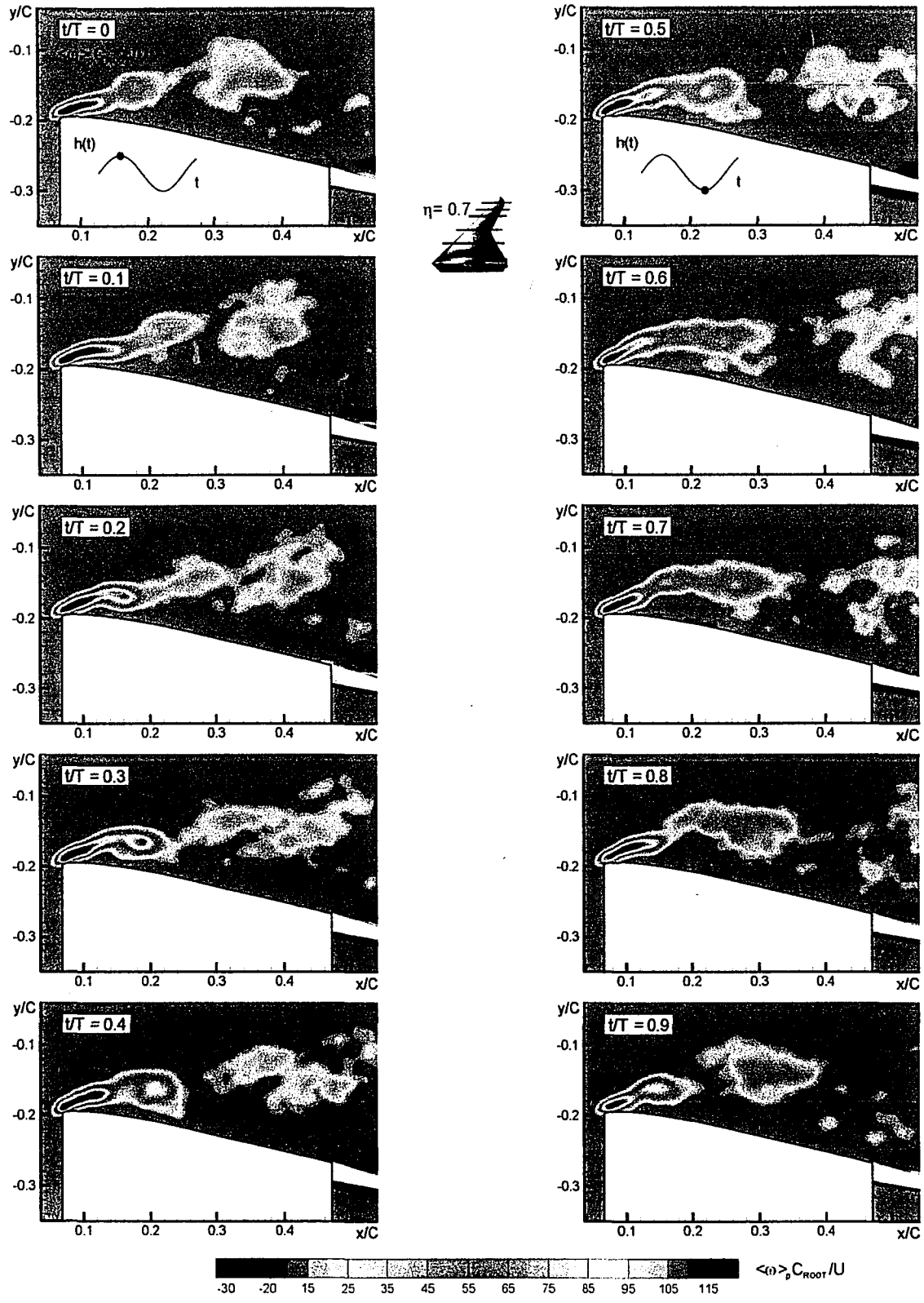


**Figure AA.18**: Phase-averaged vorticity contours for case of wing subjected to perturbations of angle-of-attack according to $\alpha = \bar{\alpha} + \alpha_e \sin 2\pi f_e t$ ; $\bar{\alpha} = 12°$, $\alpha_e = 0.45°$ and $f_e = f_o/4$, where $f_o$ is the inherent instability frequency of separating shear layer. Reynolds number based on mean aerodynamic chord is $Re_c = 17927$

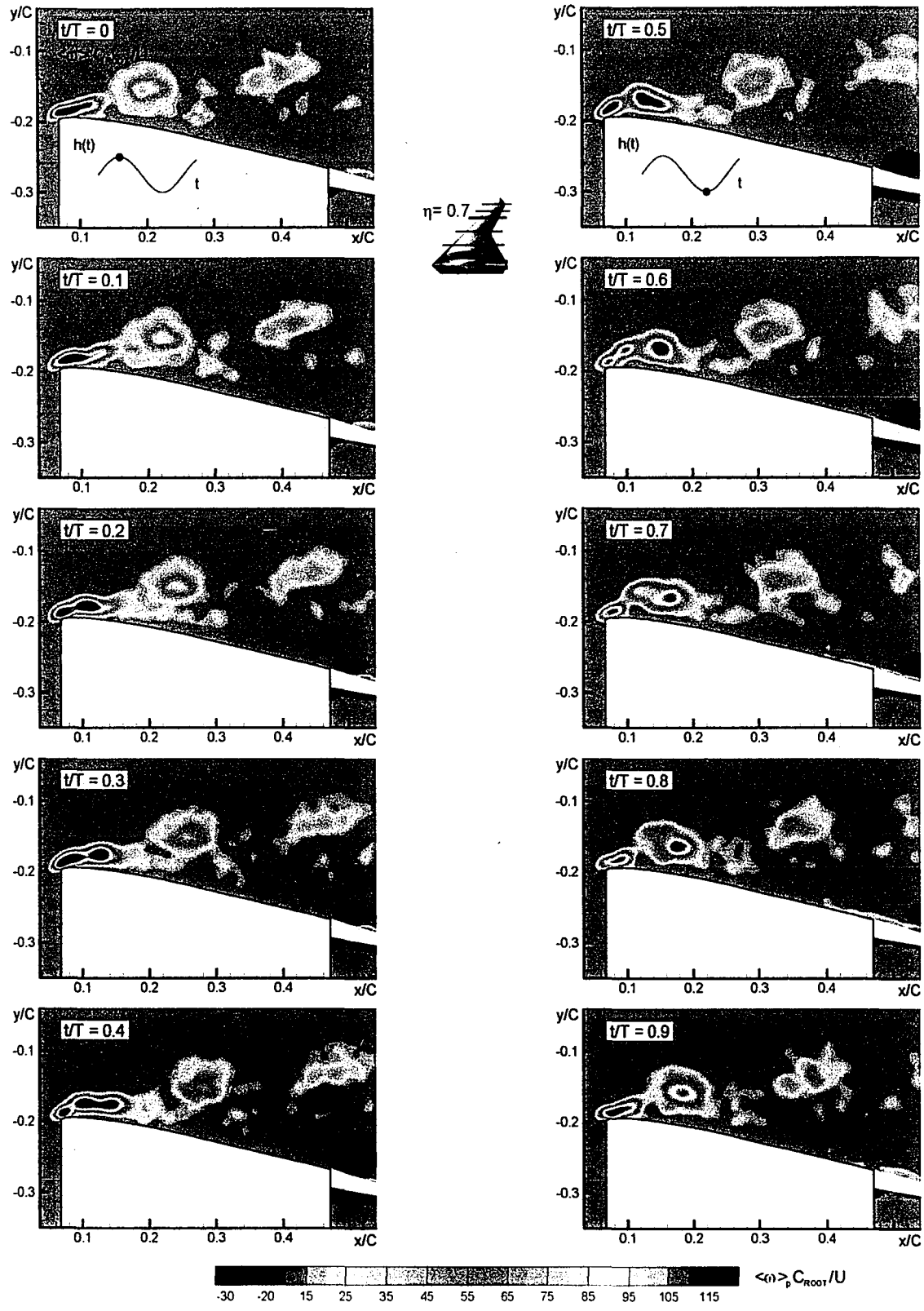


**Figure AA.19**: Phase-averaged vorticity contours for case of wing subjected to perturbations of angle-of-attack according to $\alpha = \bar{\alpha} + \alpha_e \sin 2\pi f_e t$ ; $\bar{\alpha} = 12°$, $\alpha_e = 0.45°$ and $f_e = f_o/2$, where $f_o$ is the inherent instability frequency of separating shear layer. Reynolds number based on mean aerodynamic chord is $Re_c = 17927$

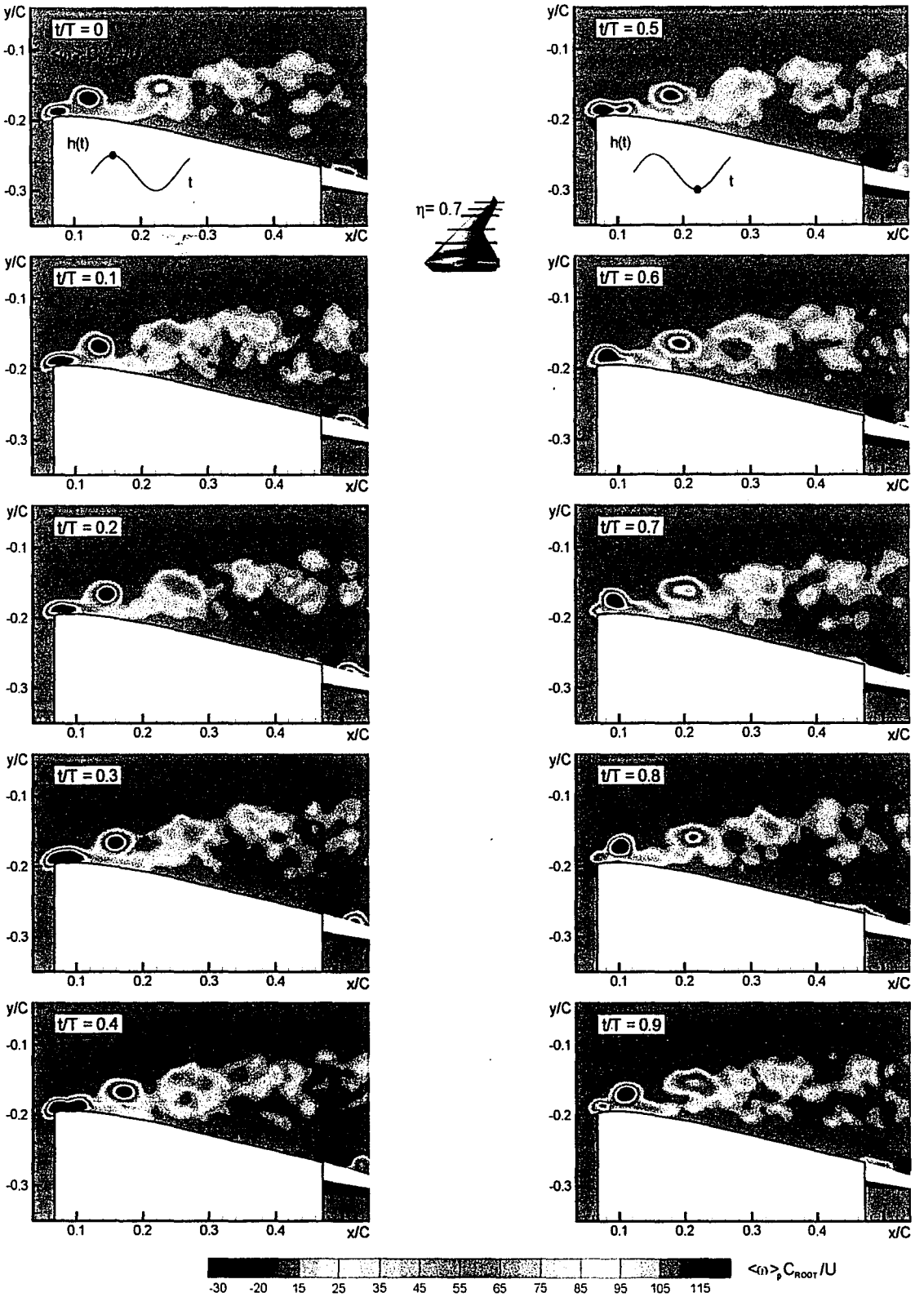


**Figure AA.20**: Phase-averaged vorticity contours for case of wing subjected to perturbations of angle-of-attack according to $\alpha = \bar{\alpha} + \alpha_e \sin 2\pi f_e t$ ; $\bar{\alpha} = 12°$, $\alpha_e = 0.45°$ and $f_e = f_o$, where $f_o$ is the inherent instability frequency of separating shear layer. Reynolds number based on mean aerodynamic chord is $Re_c = 17927$

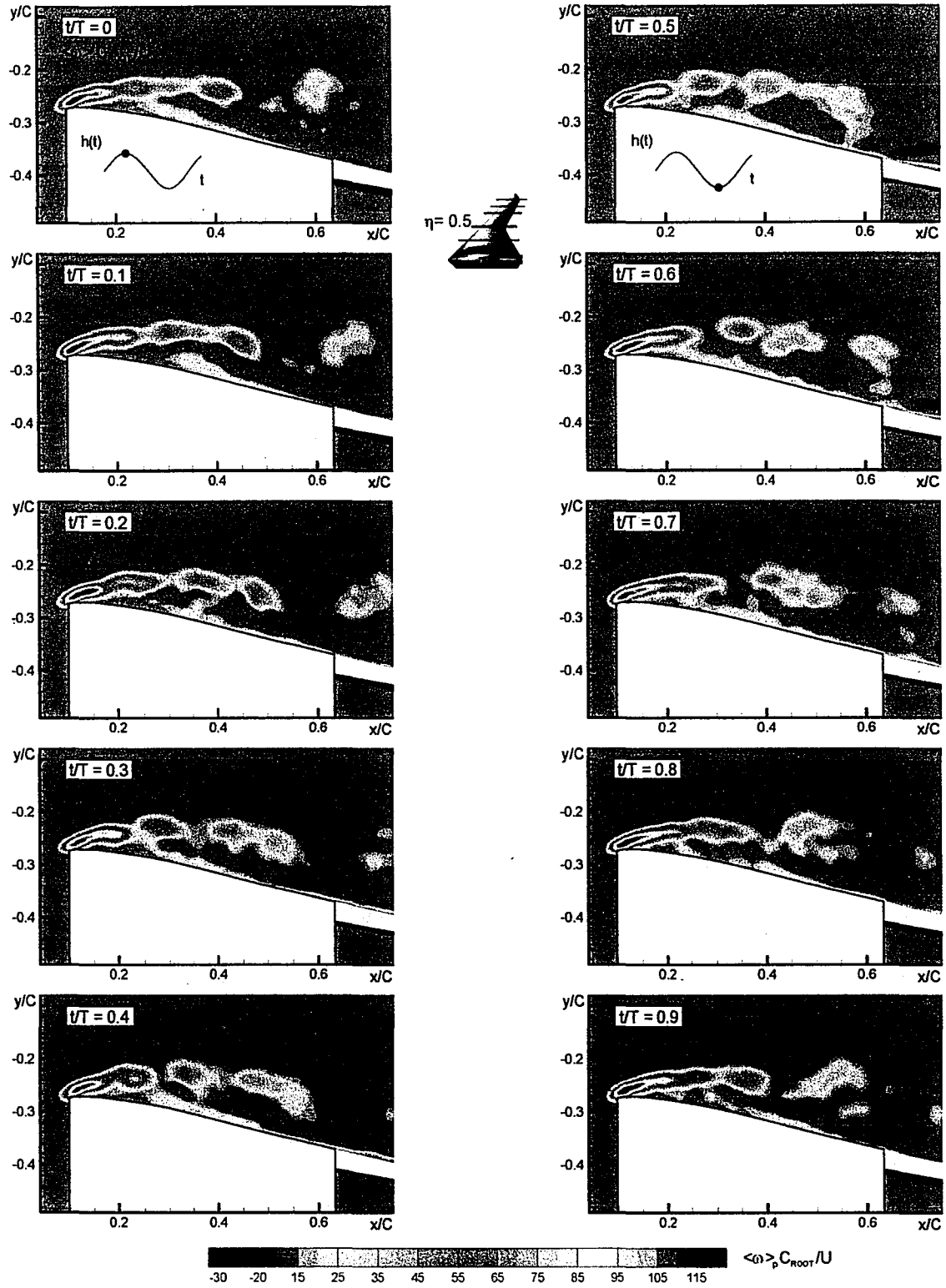


**Figure AA.21**: Phase-averaged vorticity contours for case of wing subjected to perturbations of angle-of-attack according to $\alpha = \bar{\alpha} + \alpha_e \sin 2\pi f_e t$ ; $\bar{\alpha} = 12°$, $\alpha_e = 0.45°$ and $f_e = f_o/4$ , where $f_o$ is the inherent instability frequency of separating shear layer. Reynolds number based on mean aerodynamic chord is $Re_c = 17927$

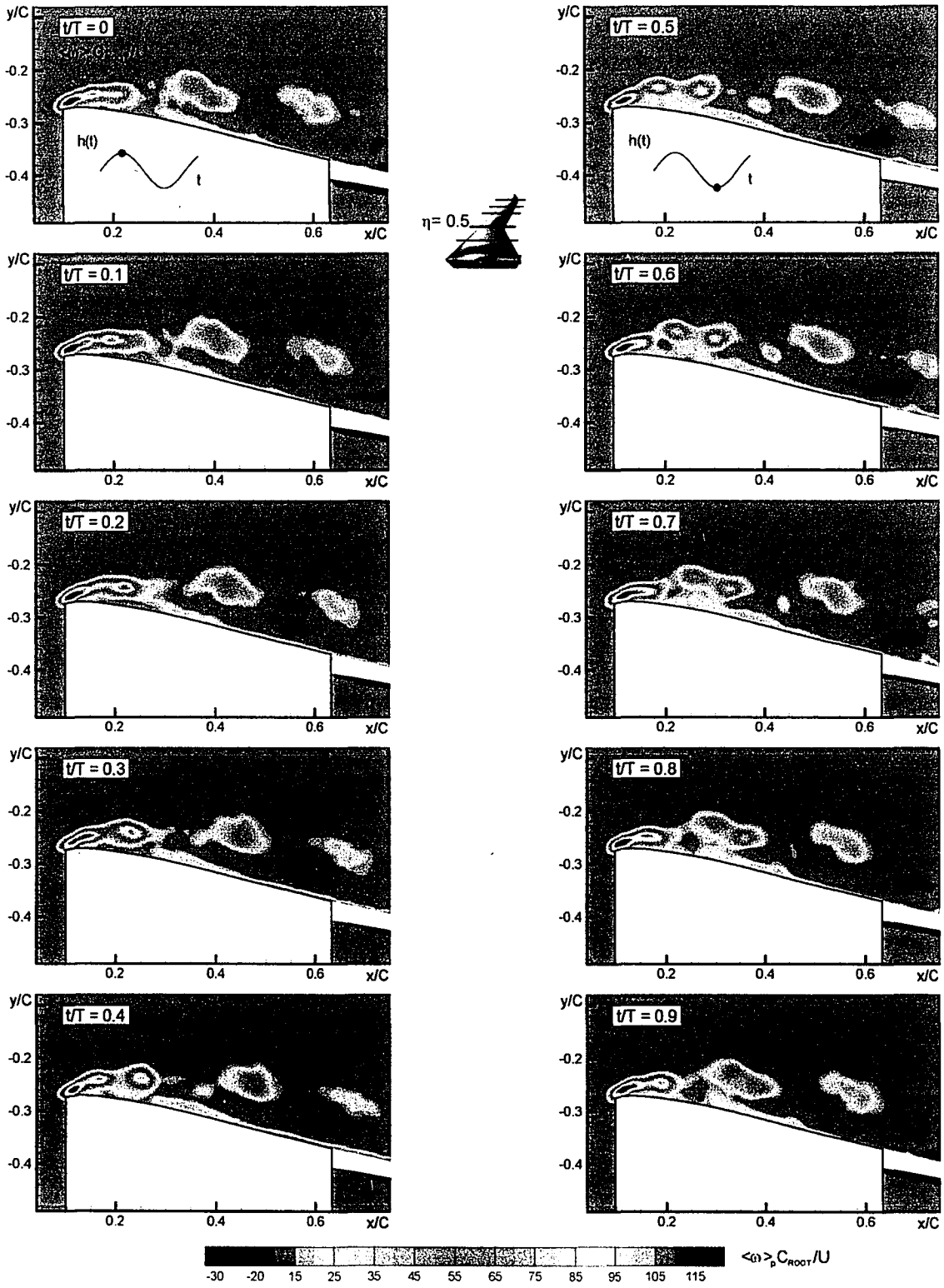


**Figure AA.22**: Phase-averaged vorticity contours for case of wing subjected to perturbations of angle-of-attack according to $\alpha = \bar{\alpha} + \alpha_e \sin 2\pi f_e t$ ; $\bar{\alpha} = 12°$, $\alpha_e = 0.45°$ and $f_e = f_o/2$ , where $f_o$ is the inherent instability frequency of separating shear layer. Reynolds number based on mean aerodynamic chord is $Re_c = 17927$

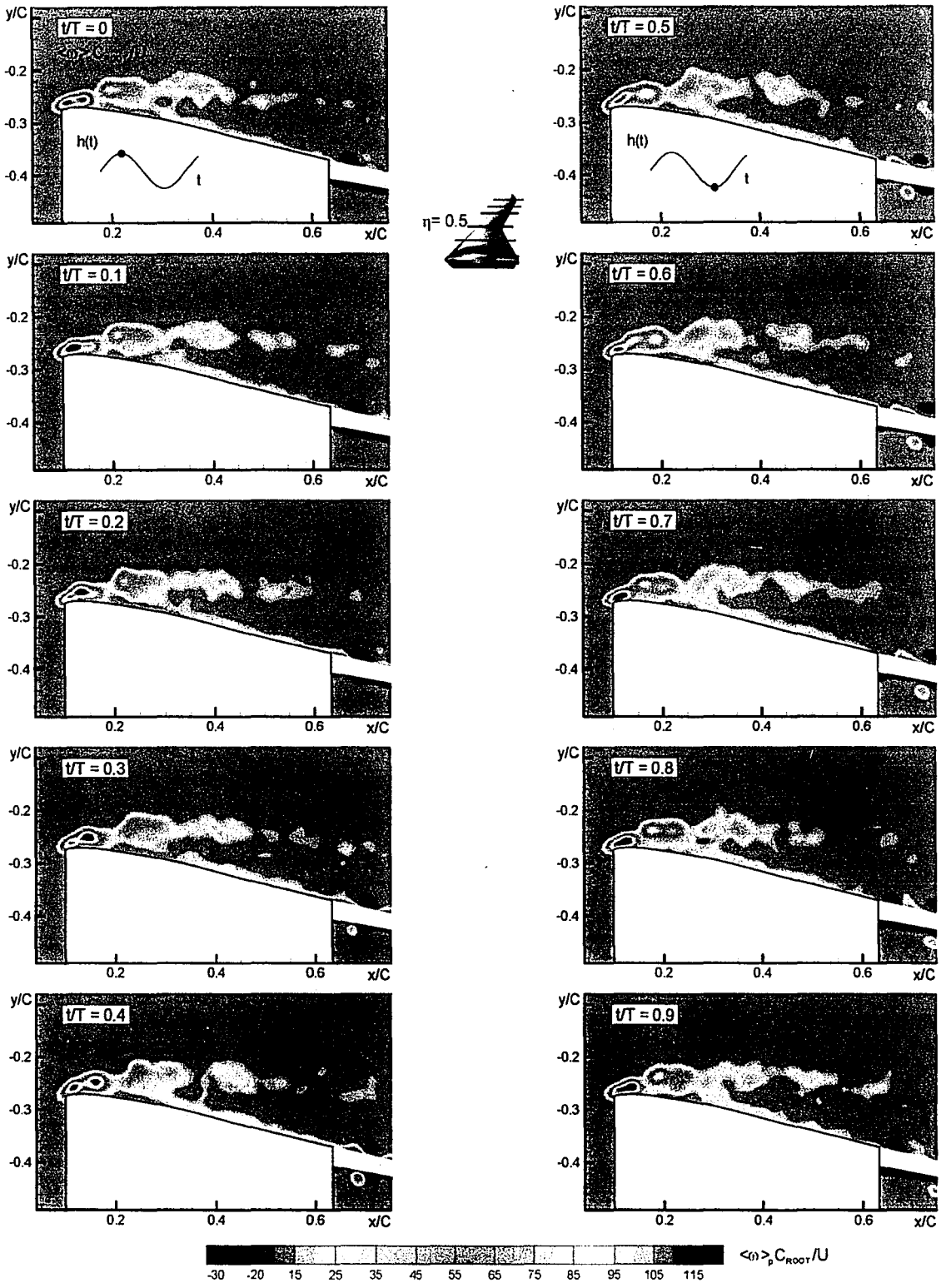


**Figure AA.23**: Phase-averaged vorticity contours for case of wing subjected to perturbations of angle-of-attack according to $\alpha = \bar{\alpha} + \alpha_e \sin 2\pi f_e t$ ; $\bar{\alpha} = 12°$, $\alpha_e = 0.45°$ and $f_e = f_o$, where $f_o$ is the inherent instability frequency of separating shear layer. Reynolds number based on mean aerodynamic chord is $Re_c = 17927$

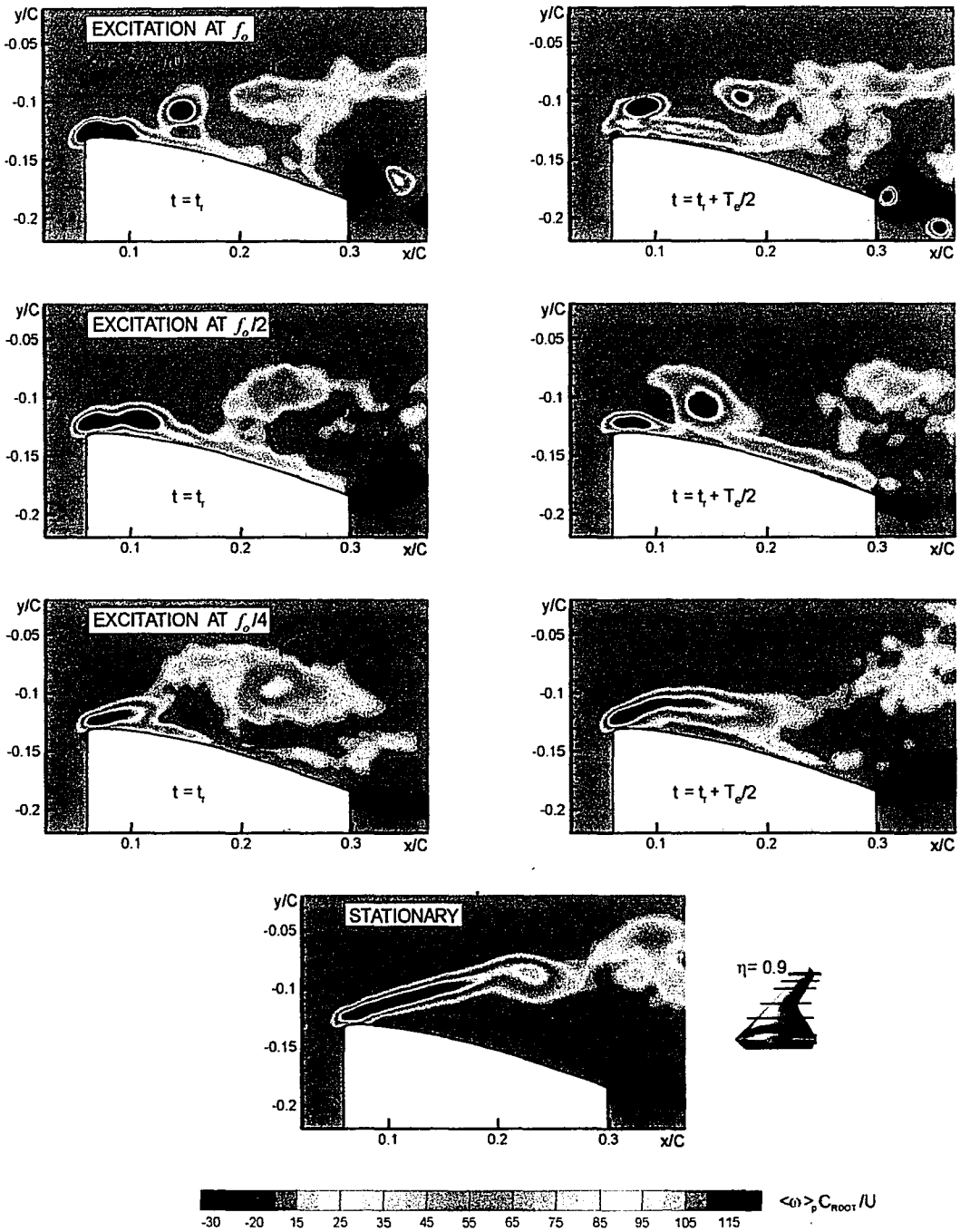


**Figure AA.24**: Phase-averaged vorticity contours for case of wing subjected to perturbations of angle-of-attack according to $\alpha = \bar{\alpha} + \alpha_e \sin 2\pi f_e t$ ; $\bar{\alpha} = 12°$, $\alpha_e = 0.45°$ and $f_e = f_o/4, f_o/2$, and $f_o$ where $f_o$ is the inherent instability frequency of separating shear layer. Case of stationary wing shown for comparison. Reynolds number based on mean aerodynamic chord is $Re_c = 17927$

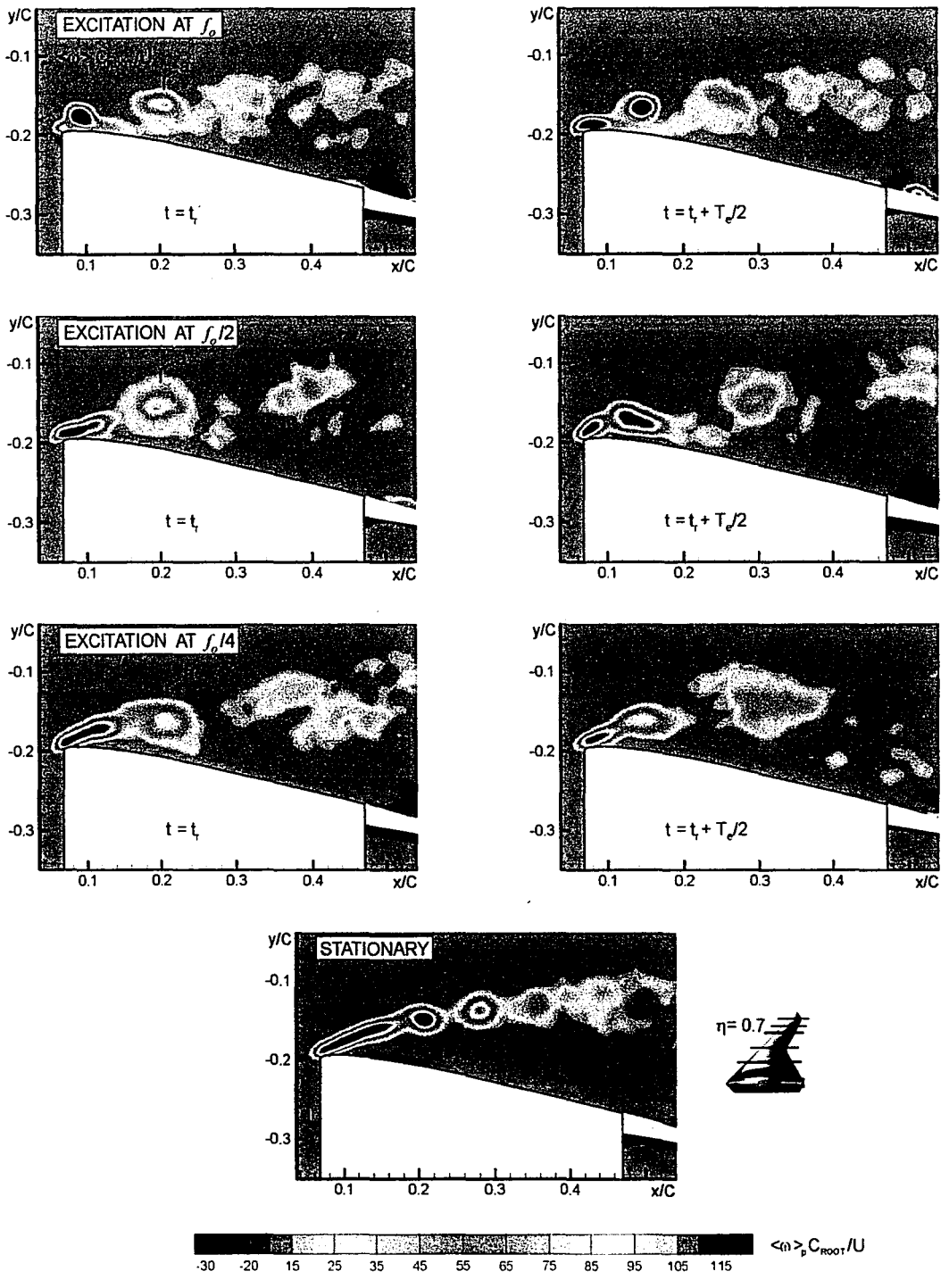


**Figure AA.25**: Phase-averaged vorticity contours for case of wing subjected to perturbations of angle-of-attack according to $\alpha = \bar{\alpha} + \alpha_e \sin 2\pi f_e t$ ; $\bar{\alpha} = 12°$, $\alpha_e = 0.45°$ and $f_e = f_o/4$, $f_o/2$, and $f_o$ where $f_o$ is the inherent instability frequency of separating shear layer. Case of stationary wing shown for comparison. Reynolds number based on mean aerodynamic chord is $Re_c = 17927$

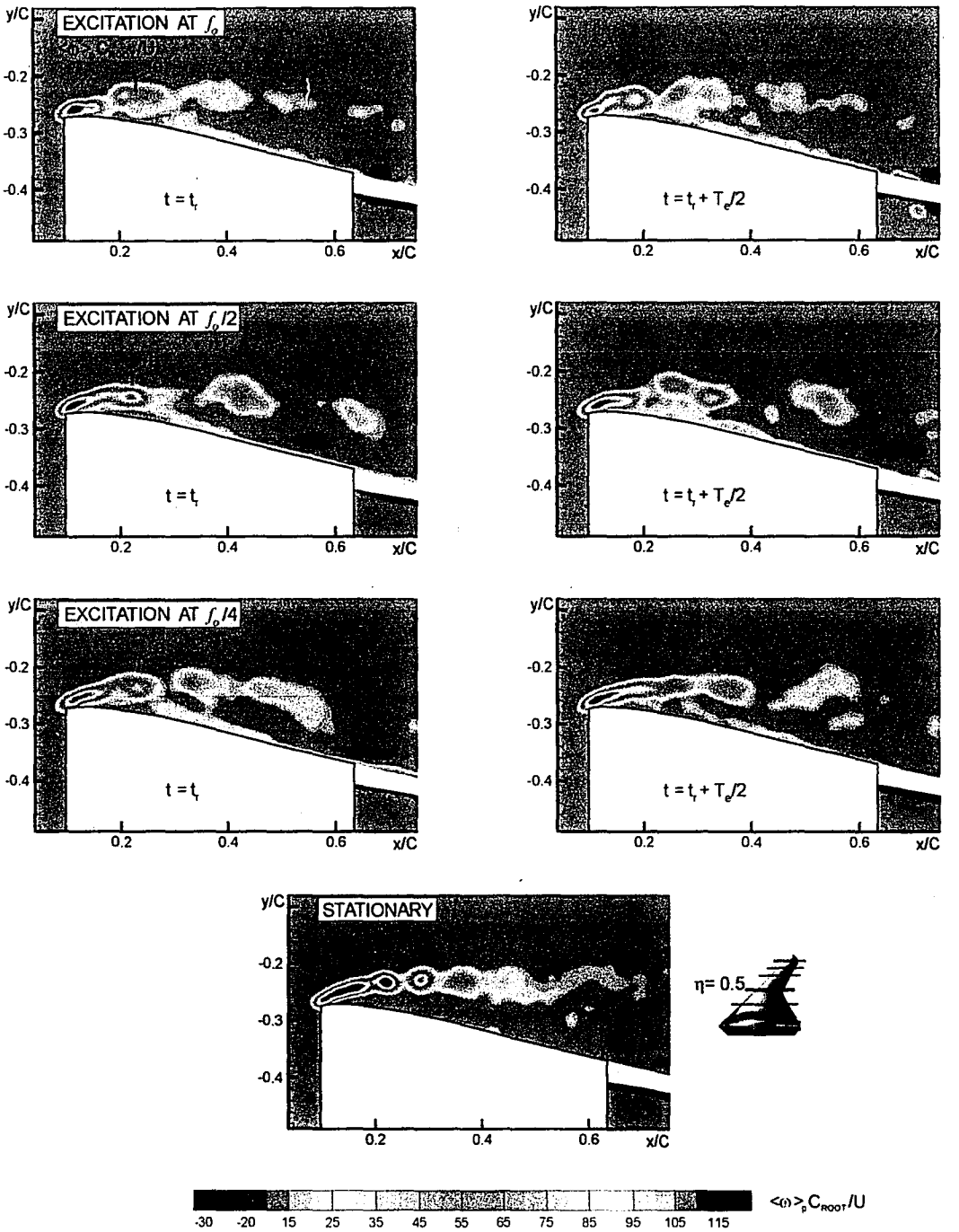


**Figure AA.26**: Phase-averaged vorticity contours for case of wing subjected to perturbations of angle-of-attack according to $\alpha = \bar{\alpha} + \alpha_e \sin 2\pi f_e t$ ; $\bar{\alpha} = 12°$, $\alpha_e = 0.45°$ and $f_e = f_o/4, f_o/2$, and $f_o$ where $f_o$ is the inherent instability frequency of separating shear layer. Case of stationary wing shown for comparison. Reynolds number based on mean aerodynamic chord is $Re_c = 17927$

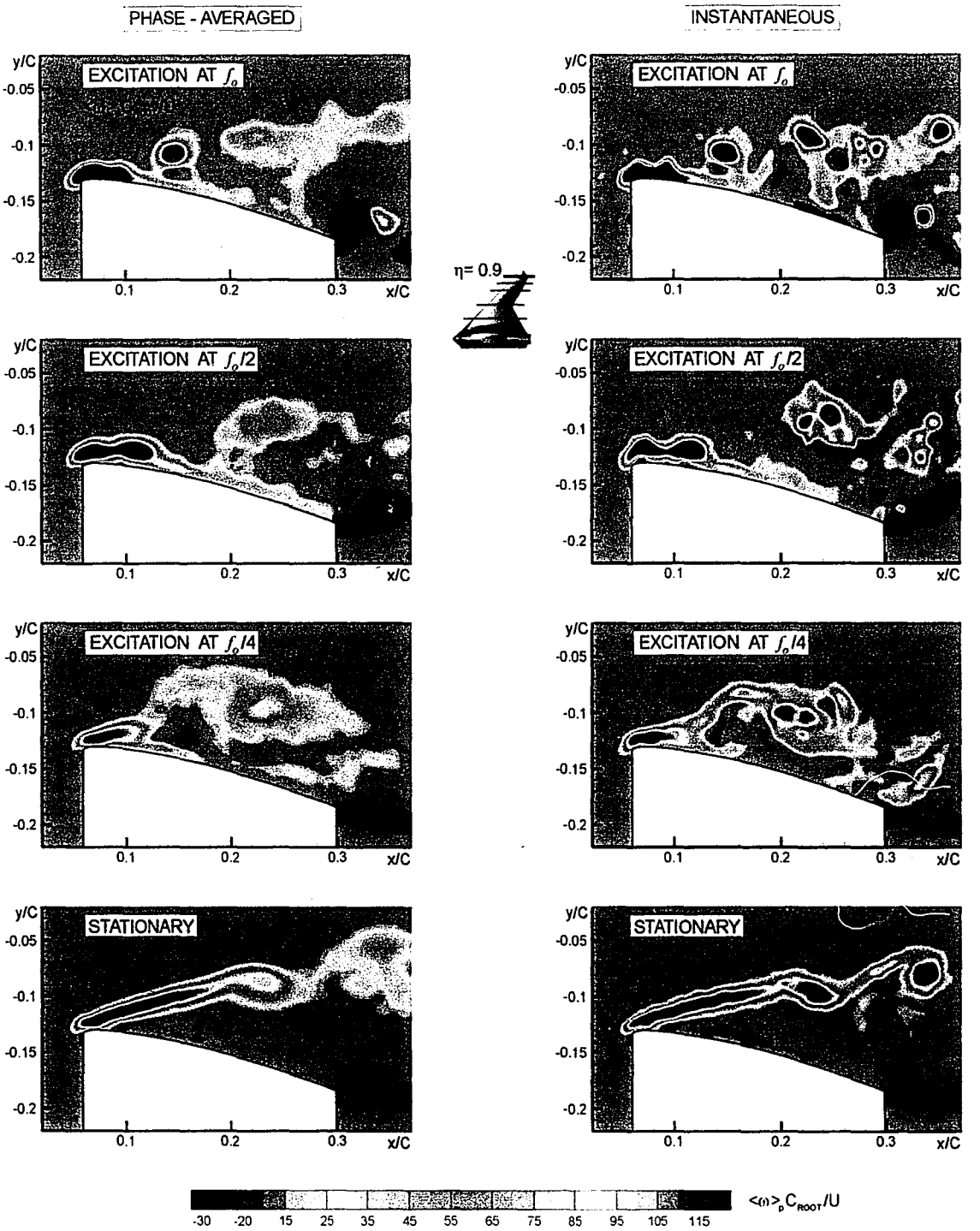


**Figure AA.27**: Phase-averaged and instantaneous vorticity contours for case of wing subjected to perturbations of angle-of-attack according to $\alpha = \bar{\alpha} + \alpha_e \sin 2\pi f_e t$ ; $\bar{\alpha} = 12°$, $\alpha_e = 0.45°$ and $f_e = f_o/4, f_o/2$ and $f_o$ . where $f_o$ is the inherent instability frequency of separating shear layer. Reynolds number based on mean aerodynamic chord is $Re_c = 17927$

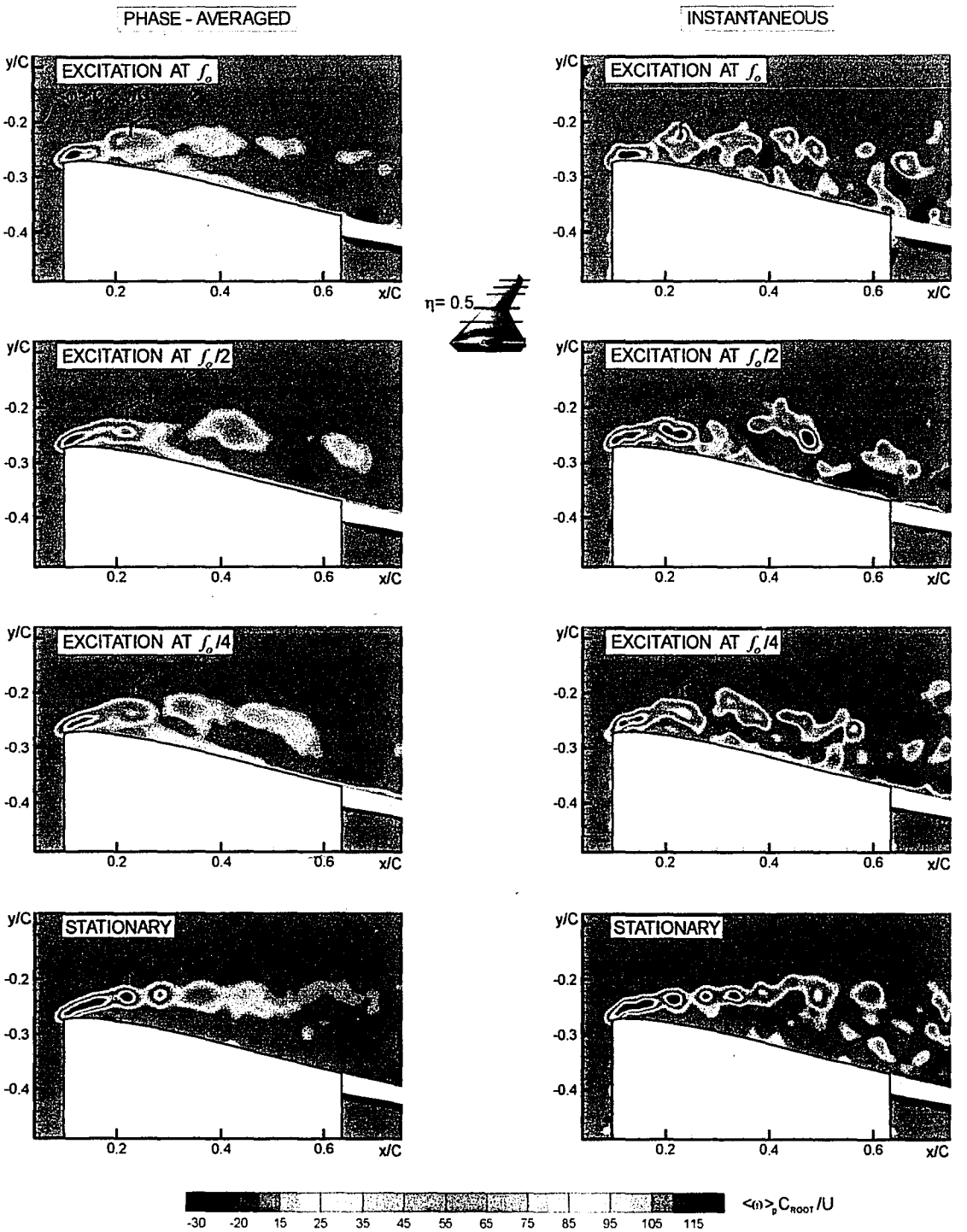


**Figure AA.28**: Phase-averaged and instantaneous vorticity contours for case of wing subjected to perturbations of angle-of-attack according to $\alpha = \bar{\alpha} + \alpha_e \sin 2\pi f_e t$ ; $\bar{\alpha} = 12°$, $\alpha_e = 0.45°$ and $f_e = f_o/4$, $f_o/2$ and $f_o$, where $f_o$ is the inherent instability frequency of separating shear layer. Reynolds number based on mean aerodynamic chord is $Re_c = 17927$

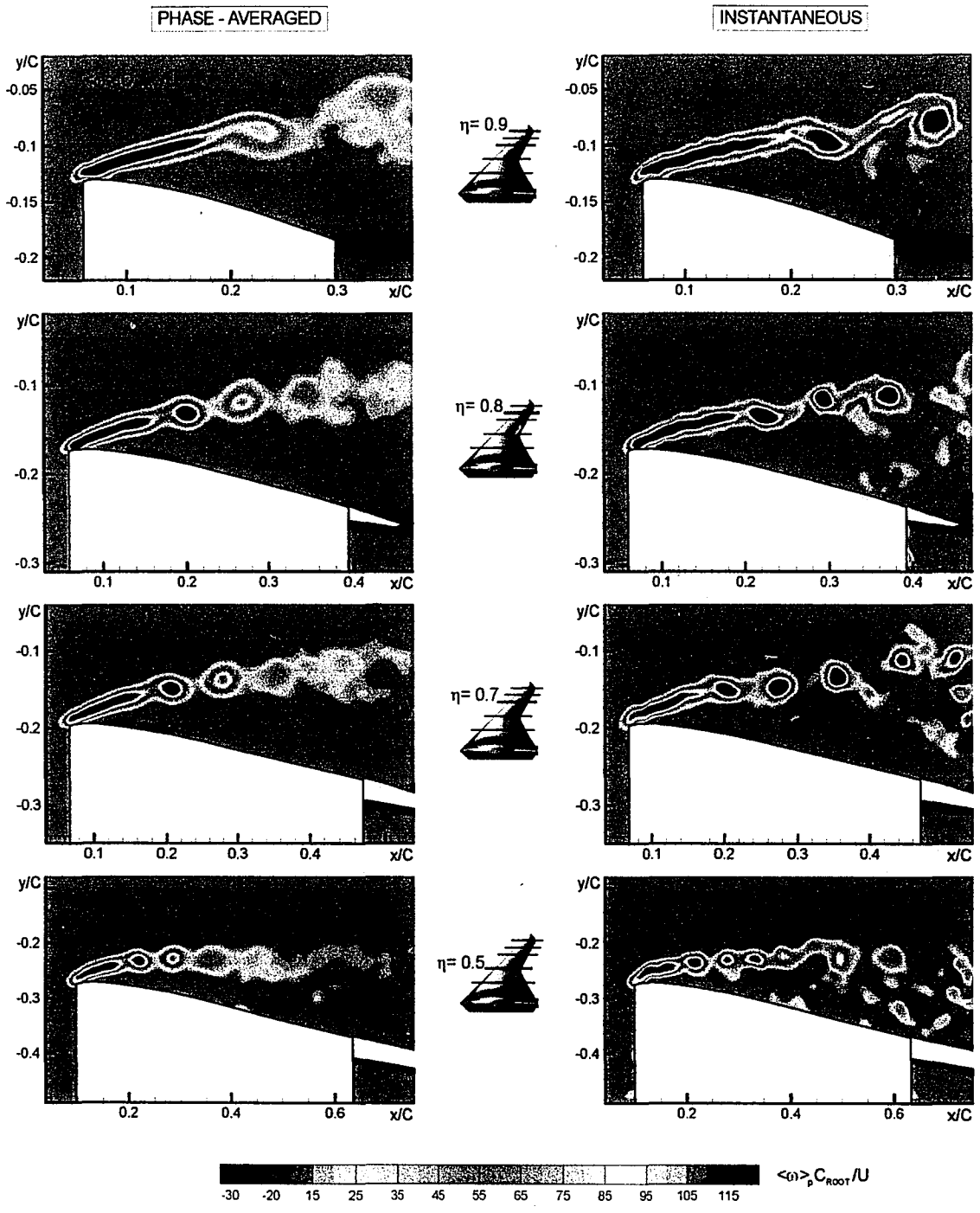


**Figure AA.29**: Paterns of phase-averaged and instantaneous vorticity on stationary wing. Reynolds number based on mean aerodynamic chord is $Re_c = 17927$

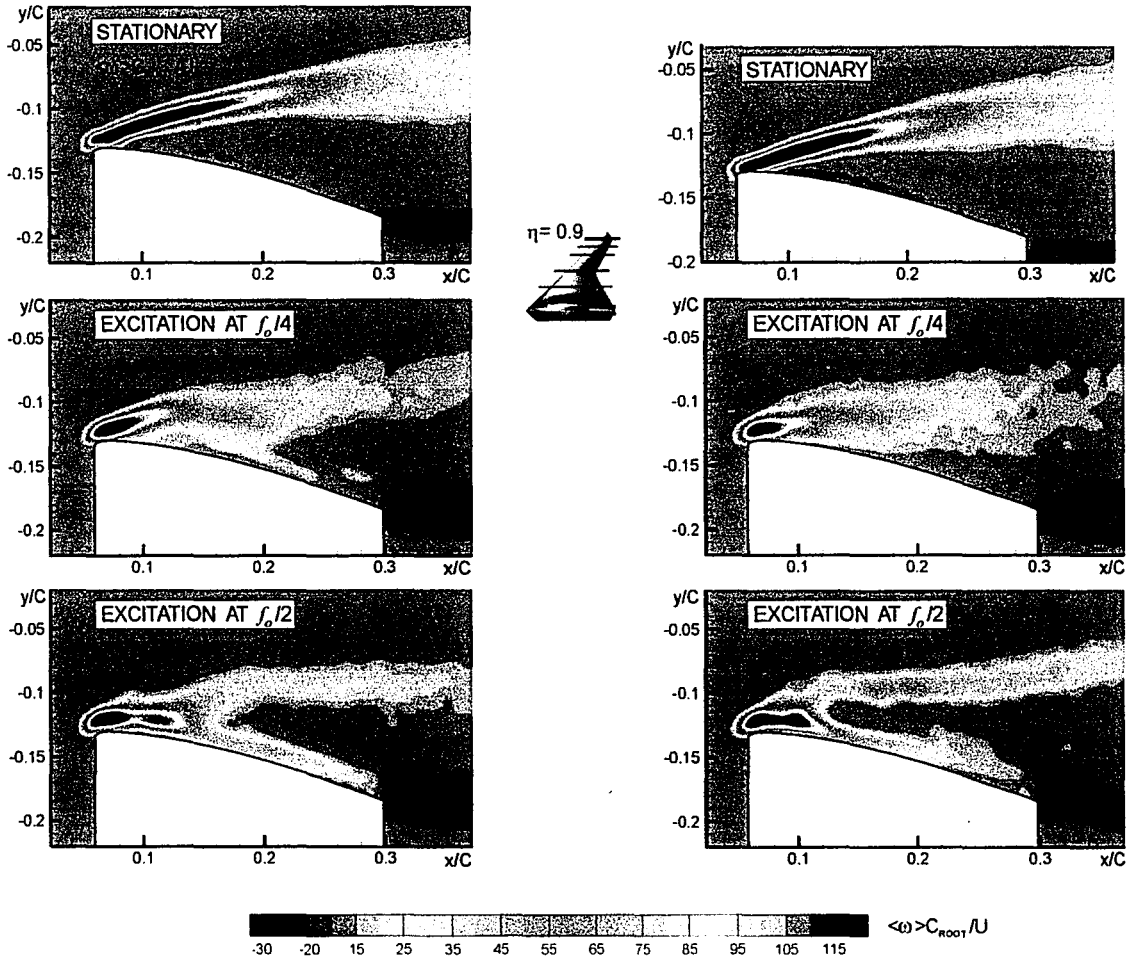


**Figure AA.30**: Comparison of time-averaged patterns of vorticity at two values of Reynolds number based on mean aerodynamic chord, $Re_c$ = 17927 (left column) and $Re_c$ = 32000 (right column). Wing is subjected to perturbations of angle-of-attack according to $\alpha = \bar{\alpha} + \alpha_e \sin 2\pi f_e t$ ; $\bar{\alpha} = 12°$, $\alpha_e = 0.45°$ and $f_e = f_o/4$ and $f_o/2$ where $f_o$ is the inherent instability frequency of separating shear layer.

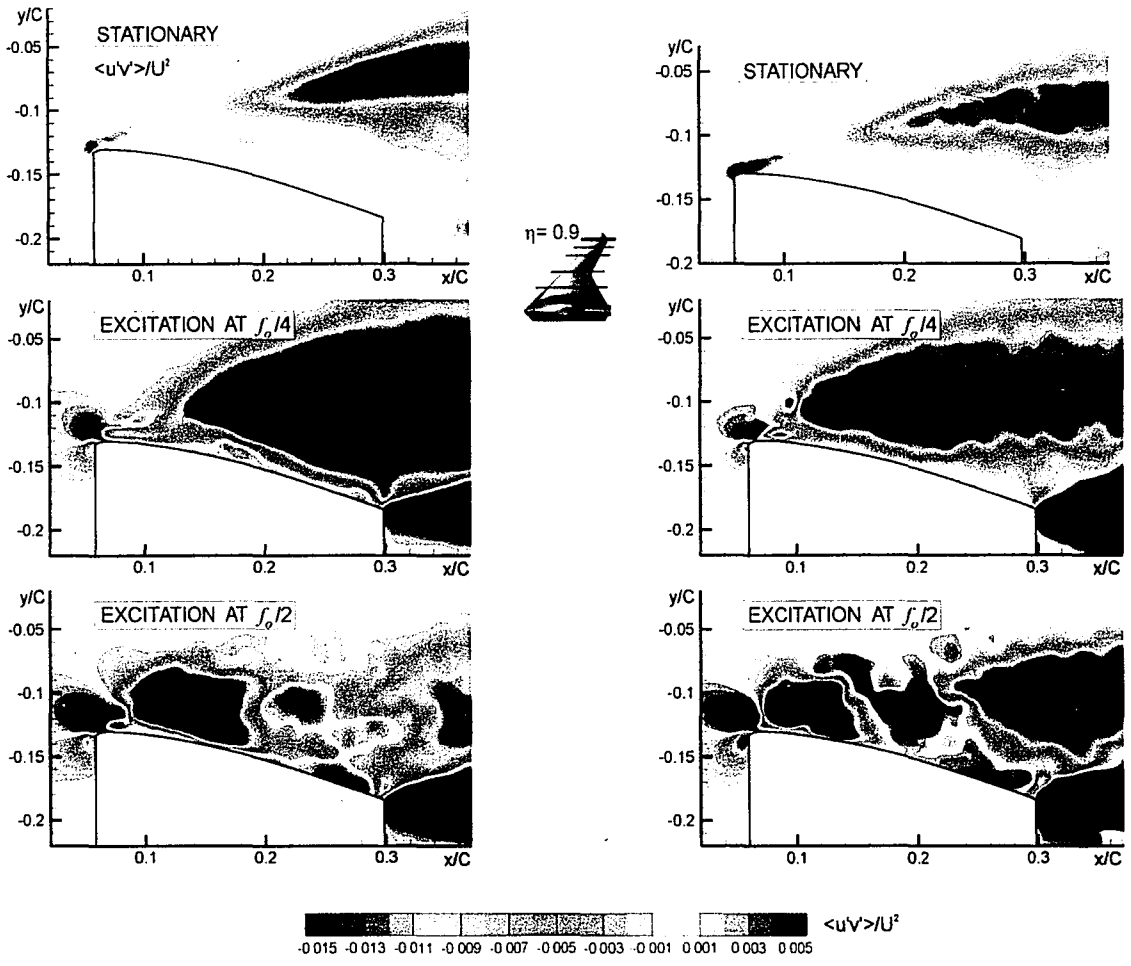


**Figure AA.31**: Comparison of time-averaged patterns of Reynolds stress at two values of Reynolds number based on mean aerodynamic chord. $Re_c$ = 17927 (left column) and $Re_c$ = 32000 (right column). Wing is subjected to perturbations of angle-of-attack according to $\alpha = \bar{\alpha} + \alpha_e \sin 2\pi f_e t$ ; $\bar{\alpha}$ = 12°, $\alpha_e$ = 0.45° and $f_e = f_o/4$ and $f_o/2$ where $f_o$ is the inherent instability frequency of separating shear layer.

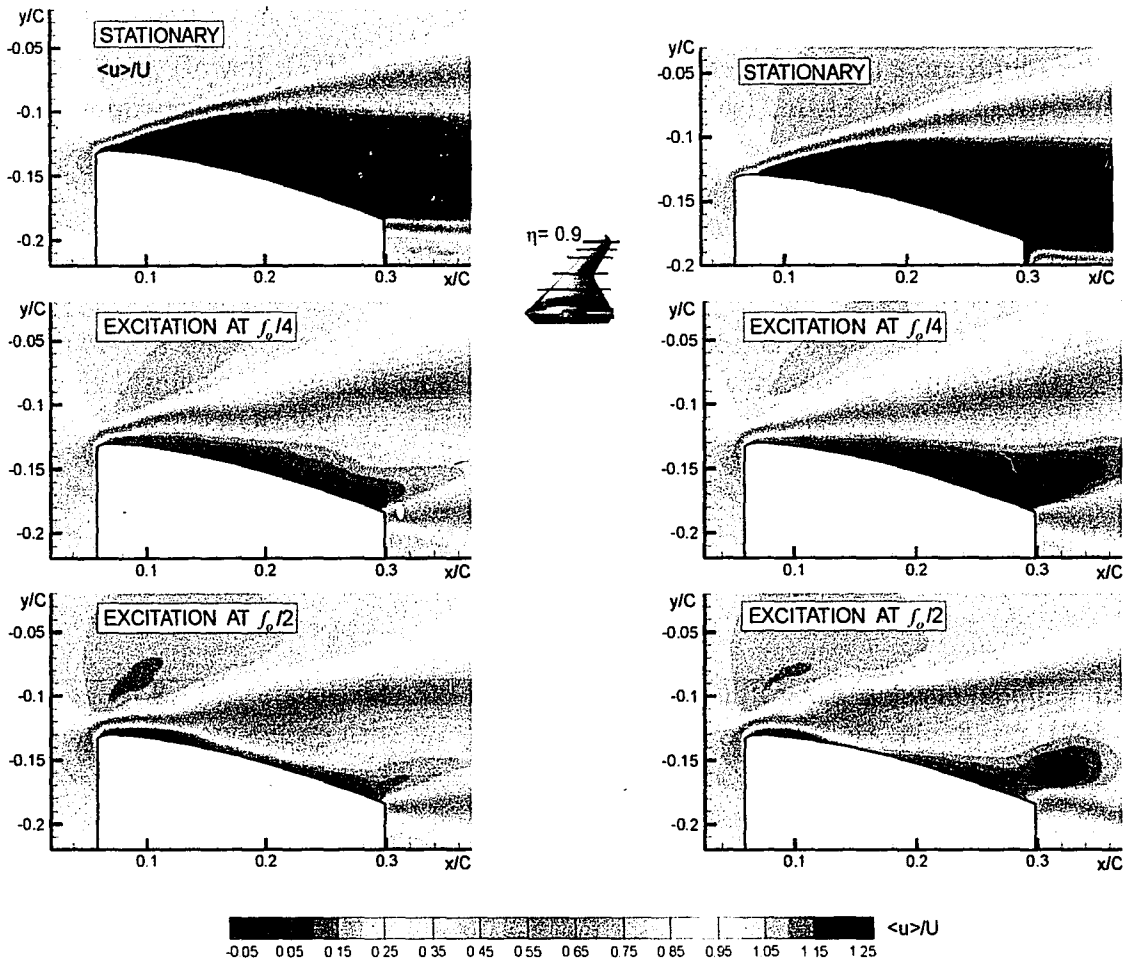


**Figure AA.32**: Comparison of time-averaged patterns of streamwise velocity at two values of Reynolds number based on mean aerodynamic chord, $Re_c$ = 17927 (left column) and $Re_c$ = 32000 (right column). Wing is subjected to perturbations of angle-of-attack according to $\alpha = \bar{\alpha} + \alpha_e \sin 2\pi f_e t$ : $\bar{\alpha} = 12°$. $\alpha_e = 0.45°$ and $f_e = f_o/4$ and $f_o/2$ where $f_o$ is the inherent instability frequency of separating shear layer.

## LIST OF REFERENCES


Atkinson, M. and Ferguson, F., 2006. "A Computational Fluid Dynamics Investigation of the 1303 UCAV Configuration with Deployable Rao Vortex Flaps", AIAA Paper 2006-1262, 44th AIAA Aerospace Sciences Meeting and Exhibit, Reno, Nevada, January, 2006.

Attar, P. J., Dowell, E. H. and Tang, D., 2008. "Delta wing with store limit-cycle-oscillation modeling using a high-fidelity structural model", *AIAA Journal of Aircraft*, Vol. 45, No. 3, pp. 1054-1061.

Bruce, R. J., 2003. "Low speed wind tunnel tests on the 1303 UCAV concept", Technical Report TR025502, QinetiQ Ltd., March, 2003.

Elkhoury, M. and Rockwell, D. 2004 "Visualized Vortices on Unmanned Combat Air Vehicle Planform: Effect of Reynolds Number", *AIAA Journal of Aircraft*, Vol. 41, No. 5, September/October, pp. 1244-1247.

Gordnier, D. V., Visbal, M. R., 1998. "Higher-order schemes for Navier-Stokes equations: Algorithms and implementation into FDl3DI", Technical Report AFRL-VA-WP-TR-1998-3060, Air Vehicles Directorate, Air Force Research Laboratory, August, 1998.

Gordnier, R. E., Visbal, M. R., 2005. "Compact difference scheme applied to simulation of low-sweep delta wing flow", *AIAA Journal*, Vol. 43, No. 8, pp. 1744-1752.

Gordnier, R. E., Visbal, M. R., 2006. "High-order simulation of low sweep delta wing flows using ILES and hybrid RANS/ILES models", AIAA Paper 2006-0504.

Gordnier, R. E., Visbal, M. R., Gursul, I., Wang, Z., 2007. "Computational and experimental investigation of a nonslender delta wing", AIAA Paper 2097-0894.

Gursul, I., 2004a. "Recent developments in delta wing aerodynamics", Invited Review Article, *Aeronautical Journal*, September, 2004, pp. 437-452.

Gursul, I., 2004b. "Vortex flows on UAVs: issues and challenges", *Aeronautical Journal*, Vol. 108, pp. 597-610.

Gursul, I., Gordnier, R., Visbal, M., 2005. "Unsteady aerodynamics of nonslender delta wings", Progress in Aerospace Sciences, Vol. 41, pp. 515-557.

Gursul, I., Vardaki, E., Wang, Z., 2006. "Active and passive control of reattachment on various low-sweep wings", AIAA Paper 2006-506.

Gursul, I., Vardaki, E., Margaris, P., Wang, Z. 2007. "Control of Wing Vortices", Notes on Numerical Fluid Mechanics and Multidisciplinary Design: Conference on Active Flow Control 2006, Springer Verlag, New York, 2007.

Ho,C. M. and Huerre, P., 1984. "Perturbed Free Shear Layers", *Annual Review of Fluid Mechanics*, Vol. 16, pp. 365-422.

Kosoglu, M. A., 2007. Flow structure along a 1303 unmanned combat air vehicle. Ph.D. Dissertation, Lehigh Univ., Bethlehem, PA

McParlin, S. C., Bruce, R. J., Hepworth, A. G., Rae, A. J., 2003. "Low speed wind tunnel tests on the 1303 UCAV concept", QinetiQ/fST/tR025502/1.0, QinetiQ, Ltd., Farnborough, UK, March, 2003.

Michalke, A., 1964. "On the inviscid instability of the hyperbolic tangent velocity profile", *Journal of Fluid Mechanics*, Vol. 19, pp. 543-556.

Nelson, R. C., Corke, T. C., He, C., Othman, H., Matsuno, T., 2007. "Modification of the flow structure over a UAV wing for roll control", AIAA Paper 2007-884.

Ol, M. V., 2006. "Water tunnel velocimetry results for the 1303 UCAV configuration", AIAA Paper 2006-2990.

Ol, M. V., Gharib, M., 2003. "Leading-Edge vortex structure of nonslender delta wings at low Reynolds number", *AIAA Journal*, Vol. 41, No. 1, 2003, pp. 16-26.

Petterson, K., 2006. "CFD analysis of the low-speed aerodynamic characteristics of a UCAV", AIAA Paper 2006-1259.

Sherer, S. E., Gordnier, R. E., Visbal, M. R., 2008. "Computational study of a UCAV configuration using a high-order overset-grid algorithm", AIAA Paper 2008-626.

Taylor, G., Wang, Z., Vardaki, E., Gursul, I., 2007. "Lift enhancement over flexible non-slender delta wings", *AIAA Journal*, Vol. 45, No. 12, pp. 2979-2993.

Vardaki, E., Wang, Z., Gursul, I., 2008. "Flow reattachment and vortex reformation on oscillating low-aspect-ratio wings", *AIAA Journal*, Vol. 46, No. 6, pp. 1453-1462.

Wong, M. D., Flores, J., 2006. "Application of OVERFLOW-MLP to the analysis of the 1303 UCAV", AIAA Paper 2006-2987.

Wong, M. D., McKenzie, G. J., Ol, M. V., Petterson, K., Zhang, S., 2006. "Joint TTCP CFD studies into the 1303 UCAV performance: first year results", AIAA Paper 2006-2984.

Yaniktepe, B., Rockwell, D., 2004. "Flow structure on a delta wing of low sweep angle", *AIAA Journal*, Vol. 42, No. 3, pp. 513-523.

Yaniktepe, B., Rockwell, D., 2005. "Flow structure on diamond and lambda planforms: trailing-edge region", *AIAA Journal*, Vol. 43, No. 7, pp. 1490-1512.

Yavuz, M. M., Elkhoury, M., Rockwell, D., 2004. "Near-surface topology and flow structure on a delta wing", AIAA Journal, Vol. 42, No. 2, pp. 332-340.

Zhang, F., Khalid, M., Ball, N., 2005. "A CFD based study of UCAV 1303 model", AIAA Paper 2006-4615.

## VITA

The author was born to Turan and Emine Yilmaz in Izmit, Turkey on March 02, 1980. He received his Bachelor of Science degree in both Mechanical Engineering and Physics from Koc University in May 2006. Then, he joined the Mechanical Engineering and Mechanics Department at Lehigh University. During his graduate study at Lehigh University, he worked under the supervision of Professor Donald Rockwell. He is currently enrolled in the Master of Science in Mechanical Engineering program in the P. C. Rossin College of Engineering at Lehigh University and will continue towards his Ph.D. at the same university.

# END OF TITLE